Accepted Manuscript

Journal of the Geological Society

Magnetostratigraphy of the Mercia Mudstone Group (Devon, UK): implications for regional relationships and chronostratigraphy in the Middle to Late Triassic of western Europe

Mark W. Hounslow & Ramues Gallois

DOI: https://doi.org/10.1144/jgs2022-173

To access the most recent version of this article, please click the DOI URL in the line above. When citing this article please include the above DOI.

Received 9 December 2022
Revised 16 April 2023
Accepted 20 April 2023

Supplementary material at https://doi.org/10.6084/m9.figshare.c.6613788

Magnetostratigraphy of the Mercia Mudstone Group (Devon, UK): implications for regional relationships and chronostratigraphy in the Middle to Late Triassic of western Europe.

***Mark W. Hounslow[1,2] and Ramues Gallois[3]**

1. Lancaster Environment Centre, Lancaster University, Lancaster, UK. LA1 4YW
2. Earth, Ocean and Ecological Sciences, Univ. of Liverpool, Jane Herdman Building, Liverpool, L69 3GP; mark.w.hounslow@gmail.com; orcid. ID: 0000-0003-1784-6291
3. 92 Stoke Valley Rd., Exeter EX4 5ER, UK gallois@geologist.co.uk orcid ID:0000-0001-5925-576X

Abstract: Global synchronisation of environmental change in terrestrial successions in deep-time is challenging due to the paucity of dating methods, a case also applicable to the Middle to Upper Triassic Mercia Mudstone Group in Britain. Using coastal cliff sections, magnetostratigraphy was evaluated at 263 horizons, defining 53 magnetozones. Magnetozones from the lower 140 m of the group demonstrate correspondence to those from the mid Ladinian to early Carnian polarity timescale, dating which is compatible with magnetostratigraphy from the underlying Sherwood Sandstone Group. Magnetostratigraphy of the Dunscombe Mudstone Formation, and associated palynological data, suggest a late Carnian to earliest Norian age, and a dramatically lower accumulation rate than adjacent formations. The polarity record demonstrates coeval flooding events, evaporite deposits and intervals of sand supply between the Wessex Basin and the Central European Basin in the Carnian. This is the result of linked climatic and eustatic changes between these separate basins, related to aeolian dust supply and the shrinkage of hyper-arid source regions for the fines. Magnetostratigraphy from the Branscombe Mudstone and Blue Anchor formations demonstrates their Norian and early Rhaetian age. These and other data suggest an alternative synchronization of marine and non-marine polarity records for the Norian polarity timescale.
198 words

Supplementary material: Section details and detailed logs of the sampled sections and inferred sequence boundaries, magnetic mineralogy data, demagnetisation behaviour and mean directions, summary of virtual geomagnetic pole data and a comparison to other European poles, construction of other composite reference sections and revised polarity scales. Excel sheet of magnetic data statistically evaluated correlation models, and age models.

Accurate and precise dating of sediment successions is the cornerstone of global understanding of many past environmental changes in deep time. It is particularly challenging merging datasets from terrestrial successions into such understanding, because of the common lack of detailed, accurate and precise biostratigraphies. In Europe the Middle and Late Triassic contains rather contrasting intervals of environmental change. The Middle Triassic saw the marine flooding of the Central European Basin (CEB) from the Palaeotethys Sea, through gateways on its southern borders (McKie 2017). Faunal and floral turnovers were low during the Middle Triassic (Brayard et al. 2009; Song et al. 2018). During the Carnian, the start of the Late Triassic, major environmental changes are linked to a northern-hemisphere-focused humid episode (Ruffell et al. 2016), which is associated with the diversification of the dinosaurs (Bernardi et al. 2018). The transition into the Norian witnessed major turnovers in marine biota (Dal Corso et al. 2020), linked to significant fluctuations in sea-water temperature, which later in the Norian witnessed rising temperatures and a climax in reef-building in the Palaeotethys (Sun et al. 2020).

In Britain the Mercia Mudstone Group (MMG) occupies part of the Middle (Ladinian Stage) and most of the Upper Triassic (Carnian to Rhaetian stages), which is ~36 Myr in duration, representing 72% of the Triassic (Ogg et al. 2020). However, the chronostratigraphy of the MMG is poorly understood, so synchronisation of environmental signals encoded in these red-bed sediments has remained elusive. The type section of the MMG is on the Devon coast and lies within the Dorset and East Devon Coast World Heritage Site (Gallois 2019). The MMG sections on the Devon coast are among the best exposed and accessible Middle and Upper Triassic sedimentary rocks in Europe. The MMG contains palynological assemblages recorded from two intervals, which allow a loose biostratigraphic age assignment to parts of the Carnian and Rhaetian (Warrington 1997; Hounslow et al. 2004; Baranyi et al. 2019). Other intervals are barren, hence the detailed chronostratigraphy of the remainder of the MMG is unknown. On the Devon coast the MMG rests on the Middle Triassic Otter Sandstone Formation (Fm), with the age of its upper part based on magnetostratigraphy and vertebrate fossils, thought to be Anisian in age (Benton et al. 1994; Benton 1997; Hounslow and McIntosh 2003). The current work addresses the age of the MMG using magnetostratigraphy, which allows the importation of chronostratigraphy by correlation with conodont and ammonoid dated successions elsewhere, that contain a linked magnetostratigraphy. This provides better insight into synchronisation of environmental changes with elsewhere in Europe.

The MMG was also important in the early development of palaeomagnetism, with geomagnetic reversals first detected in this unit in the pioneering study of Clegg et al. (1954). Expanding on preliminary work of Creer et al. (1954), the details of the first magnetostratigraphy from Triassic age sediments was by Creer (1959) from a 52 m section across the Otter Sandstone Fm - MMG boundary east of Sidmouth, in which three magnetozones were identified. Also pioneering was the use of alternating field tumbling demagnetisation on sediments which was later followed by a pioneering study using low-temperature methods to characterise the magnetic mineralogy of red beds (Creer 1961).

Currently, the Middle and Late Triassic geomagnetic polarity timescale (GPTS) is reasonably well understood allowing international chronostratigraphic correlations to be established (Gallet et al. 2007; Hounslow and Muttoni, 2010; Maron et al. 2019; Zhang et al. 2020; Ogg et al. 2020). However, the magnetic polarity pattern in some parts of the Carnian is less certain (Zhang et al. 2020; Hounslow et al. 2022a). In the Upper Triassic uncertainty remains about an internationally agreed position for the base of the Rhaetian (Galbrun et al. 2020), although that for the base of the Norian is closer to formal acceptance (Hounslow et al. 2021b).

We determined a magnetostratigraphy from the Devon coastal outcrops, providing the first detailed chronostratigraphy of the MMG. This provides a better understanding of the synchronisation of the British Middle and Upper Triassic with respect to the much better studied German Triassic. These data also allow re-assessment of the composite polarity timescale through the Norian by using additional data from the Upper Chinle Formation (of New Mexico and Arizona) and elsewhere. This suggests a revised GPTS that shows better convergence of the astronomically scaled magnetostratigraphy from the Newark Supergroup and biostratigraphically better-dated marine sections through the Norian-Rhaetian.

The Mercia Mudstone Group in the Wessex Basin

The sections exposed in the east Devon cliffs between the outfall of the River Sid [SY 129 873] at Sidmouth, and east of the outfall [SY 273 893] of the River Axe at Seaton provide the type section of the Mercia Mudstone Group (Howard et al. 2008; Gallois, 2019 Fig. 1). A total of about 470 m of Mercia Mudstone Group sediments, predominantly red mudstone (and some green) with a few thin beds of sandstone, are exposed in these sections. There are minor gaps in the succession due to faulting with potentially larger gaps in the Axe Valley Fault Zone (Fig. 1). Micro- and macro-fossils are largely absent in these mudstones. The MMG was previously inferred to range in age from the early Ladinian to late Rhaetian

based on: a) Anisian-age vertebrates (Benton et al. 2002) and a magnetostratigraphy from the underlying Otter Sandstone Fm (Hounslow and McIntosh 2003), b) Carnian miospores from the predominantly green and grey mudstones in the Dunscombe Mudstone Fm (DMF) and immediately adjacent units (Baranyi et al. 2019) and c) Rhaetian miospores from the Lyme Regis Borehole (Warrington 1997) and miospores and magnetostratigraphy from the top-most Branscombe Mudstone and Blue Anchor formations in the Bristol Channel Basin (Hounslow et al. 2004).

The MMG comprises four formations and eight members (Gallois 2001) that crop out in almost continuous coastal cliffs between Sidmouth and Seaton (Fig. 1; Table 1). Detailed lithological logs and magnetostratigraphic sampling points for the sections between Sidmouth and Haven Cliff are shown in the Supplementary Information (SI Figs. S1.1 to S1.7).

The red mudstones that make up most of the MMG are thought to have formed largely in arid playa environments, with mud input likely via mud-pellets (Talbot et al. 1994; McKie 2017), and/or loess accumulation (Jefferson et al. 2000; Mao et al. 2021). In more marginal situations in the north-eastern part of the Bristol Channel Basin some horizons have pedogenic features such as slickensides (Milroy et al. 2019). However, palaeosols are not present in most of the MMG on the Devon coast but do occur within the Dunscombe Mudstone Fm (DMF) and its immediately underlying unit. Sedimentological evaluation of the DMF indicates it formed in a freshwater lacustrine environment with shallow channels (Porter and Gallois 2008), with associated beds of halite/sulphate collapse breccias (Gallois 2003). Within this general pattern of sedimentation there are regional lithological variations that are poorly understood in the absence of age-diagnostic indicators. However, overall facies are like those of other Germanic-type facies in western Europe (Aigner and Bachman 1989; Reinhardt and Ricken 2000; Vollmer et al. 2008; McKie 2017). The Wessex Basin in which these strata accumulated is a sag basin without bounding faults (Butler, 1998). Coeval Upper Triassic basin-margin strata (carbonates and some coarse clastics) onlap basement, with limited areal occurrence, in marginal units to the NW (Milroy & Wright, 2000; Milroy et al. 2019). This basin therefore is tectonically quiescent in contrast to some other well studied Upper Triassic basins, such as the Newark Rift Basin, where tectonism played a more active role in sedimentation (Withjack et al. 2013).

Sampling and Methods

Samples were collected from 262 horizons, including four from the Pennington Point Member (which overlap the sampling of Hounslow and Mcintosh (2003) from the Otter

Sandstone Fm). From these samples, 447 specimens were measured (Table 2), placed onto sub-sections that represent natural continuously exposed segments of the MMG outcrop (see SI section 1). Red mudstone horizons were preferred for sampling, if available, but non-red lithologies were sampled in the DMF and Blue Anchor Formation (BAF). Sampling used exclusively oriented hand-samples, prepared from suitable exposures, using hammers and digging tools to expose a fresh block. Flat surfaces on these were oriented with a magnetic compass and a specially designed 'foot-print' orientation staff (Hounslow et al. 2022b). Samples were wrapped in the field for protection during transportation. Sampling was segmented into subsections detailed in Table 2 and SI section S1.

In the laboratory, specimens were re-oriented and set in dental plaster, from which cubic palaeomagnetic specimens were cut dry with a diamond saw (the mudstones tend to fracture and crumble when exposed to saw coolant water).

Low field magnetic susceptibility (K) was measured using either an AGICO Kappabridge or Bartington MS2 meter. Measurements of Natural Remanent Magnetisation (NRM) were made using a 3-axis CCL GM400 cryogenic magnetometer (noise floor ~ 0.002 mA/m with holder correction). Red mudstone specimens were subjected to stepwise thermal demagnetisation, using a Magnetic Measurements Ltd, MMTD1 thermal demagnetiser, in 100-50°C steps up to 720°C, with most steps above 400^{o}C. Magnetic susceptibility measurements were performed after each heating step, to monitor mineralogical changes caused by the heating, which were mostly minor (see SI). Some non-red samples from the DMF and BAF (41 specimens in total) were measured by a combination of thermal demagnetisation up to around 300-400 ^{o}C followed by reverse-tumbling AF demagnetisation (on a Molspin demagnetiser). This procedure was used to limit thermal alteration which obscured the characteristic remanent magnetisation (ChRM) in these lithologies. The specimen demagnetisation results were analysed using principal component analysis in the LINEFIND software (Kent et al. 1983), to extract the Triassic ChRM from the specimen data (See Hounslow and McIntosh 2003; Hounslow et al. 2008a; 2021a for analysis details). Great circle type behaviour was also shown by many specimens during demagnetisation, and behavioural classes S (for linear -fits) and T (great circle behaviour) were assigned to specimens (see demagnetisation behaviour panel in Figs 2 to 7). These were further sub-divided into three qualitative classes (S1, S2, S3 and T1, T2, T3; with class 1 the top quality) based on the directional scatter and number of points in the fitted principal component data (see Hounslow et al. 2008a; 2021a for classification details). Directional data for some of the weakest intensity specimens was too erratic and these specimens were rejected (X-class).

Based on the approach to expected Triassic directions and the behaviour classes, the specimen is assigned a polarity quality (R, R?, R??, ?, N??, N? or N), to indicate its reversed or normal polarity status, with R? or N? indicating a polarity assignment of lower quality, compared to R or N of top quality. '?' indicates the specimen could not be confidently assigned a polarity (Figs. 2 to 8).

The specimen virtual geomagnetic pole (VGP_R) latitudes (Hounslow et al. 2022b), were determined with respect to the reference mean VGP direction for either the Sidmouth Mudstone (MS, MD samples), Dunscombe Mudstone (MW samples), Branscombe Mudstone (ML, SH, MB, SE samples) or Haven Cliff (HC samples) data. Values of VGP_R latitude near $+90^o$ indicate a normal polarity specimen and values near -90^o indicate reverse polarity (Figs. 2 to 8). Directional statistics (see SI Table S3.1) were determined with PMagtool v.5 (Hounslow 2006).

The magnetic mineralogy of the red mudstones of the Sidmouth Mudstone Fm was described by Creer (1957, 1961), and additional data are given in SI section 2, confirming haematite dominates the natural remanent magnetisations (NRM) in most of the MMG.

Statistical t of the magnetic polarity correlations was determined by firstly characterising the polarity pattern in terms of five metrics for each magnetozone, t_0, $\log_e(t_{-1}/t_0)$, polarity bias, Shermans ω_2 statistic and geometric mean. Where t_0 is the thickness (or duration) of the magnetozone, and t_{+1}, t_{-1} are the corresponding values for the underlying and overlying magnetozones. The later three metrics use t_{+1}, t_0 and t_{-1}. $\text{Log}_e(t_{-1}/t_0)$ is used in quantitative polarity correlation since it is less dependent on sedimentation rate changes (Man, 2008; Lallier et al. 2013). The polarity bias, ω_2 and mean thickness metrics characterise more about the local polarity structure than using t_0 or $\log_e(t_{-1}/t_0)$ individually (Olsen et al. 2014) and have been used in quantitative multivariate polarity correlation (Hounslow et al. 2022b). Using these metrics for each magnetozone the polarity correlation models were evaluated for statistical similarity using the similarity of matrices index (SMI) and Procrustes similarity index (PSI) using methods in Indahl et al. (2018), The probability of association of the corresponding polarity patterns uses the RV-based statistic P_{RV} (Josse et al. 2007). Lastly the divergent characteristics of each magnetozone in the correlation models was characterised by the Euclidean distance (d_i) using the above five metrics above, in which more problematic intervals of correlation are highlighted with larger d_i. Care was taken to approximately normalise the five metrics to similar means and standard deviations. This involved using $\log_e(t_{-1}/t_0)*0.5$ and $2*\omega_2$ and most-often scaling magnetozones to duration (in

Myr). This allows comparison of the median of d_i (d_{median}), as an additional approximate measure of overall polarity pattern divergence. Statistical comparisons used R.

We also provide a preliminary assessment of the sequence stratigraphy of the MMG, which is used with an assessment of the wider regional implications of this study. Details of sequence boundaries selected are indicated in SI Table S1.2. These use the playa-lacustrine environmental models proposed by Aigner and Bachman (1989), Reinhardt and Ricken (2000) and Vollmer et al. (2008).

Results

NRM intensity is broadly related to colour, with red-mudstones having intensity 1-7 mA/m, and others 0.03- 1.5 mA/m (left panels in Figs. 2 to 8). The multi-coloured lithologies from the DMF have a less simple relationship to NRM intensity (Figs. 4a; see SI section 2). Demagnetisation behaviour shows two components: a low laboratory unblocking temperature (LT) component and a dual polarity ChRM at the highest unblocking temperature. The LT component typically ranges from NRM or 100 ^{o}C to around 350^{o}C, but in some specimens can extend to 500^{o}C or more rarely to 600^{o}C (See SI section 3). The LT component typically dominates the magnetisation, which rapidly demagnetises in intensity towards 400 ^{o}C (SI section 2). The Fisher mean of the LT component (in geographic coordinates) is 349°, +53° (α_{95}=5.9°, k=3.3, n=245) and may be partly a Brunhes-age component, but with many specimens displaying partial overlap with the Triassic components (see SI section 3 for details and demagnetisation plots). However, the mean inclination is shallower than expected for the Brunhes (~67°), indicating the LT component could be partly acquired during the Early Cretaceous, when the MMG were eroded and onlapped (Fig. 1).

The ChRM in red mudstones is shown predominantly by linear fits to the high temperature steps (on average from 480 ^{o}C to 680-700 ^{o}C or the origin; see SI section 3), but with some more unusual specimens having ChRM that unblocks from 150-400 ^{o}C. In the non-red lithologies from the DMF, ChRM ranges are 300-400^{o}C to 40 - 80mT or the origin. Linear fits comprise data from 62% of specimens (S-class data points in Figs. 2 to 8, 255 specimens). The ChRM identified by great circle trends toward the expected direction (T-type behaviour; Figs. 2 to 8), comprised 32% of specimen data (133 specimens). The remaining 6% of specimens failed to yield useful directional data either due to complete LT and ChRM component overlap or absence of a ChRM (indicated as X-class). A total of 88%

of specimens were assigned polarity using the two better categories of polarity quality (i.e. N, R, N?, R?).

Mean directions were determined for each section using either the S-class directions (Fig. 9) or additionally using the great circle data from the T-class specimens (SI Table S3.1). Directions mostly pass the reversal test with class Rb or Rc, and the derived palaeopoles are like other Triassic poles from stable Europe (see SI section 4).

Magnetostratigraphy

Magnetozones are assigned to 12 major magnetozone couplets labelled SS1 to SS12 (Sidmouth to Seaton composite section), with SS12 in the Seaton Cliff section. The basal reverse magnetozone in the MMG is labelled BS8r, continuing the labelling used by Hounslow and McIntosh (2003) for the Budleigh Salterton to Sidmouth sections in the Sherwood Sandstone Group (Fig. 2). The Haven Cliff section uses a separate magnetozone code (HC1n to HC3r; Fig. 8) because its relationship with the SS-magnetozones is less secure.

The lower ~140 m of the MMG between the River Sid outfall to Hook Ebb (Figs. 2,3) is composed of 11 magnetozones, with the thickest magnetozone (SS1n) in the whole of the group at 36 m, in the Salcombe Hill Mudstone Mb (Fig. 2). The polarity in the top of the Otter Sandstone Formation (Pennington Point Mb) east of Sidmouth is consistent with that previously measured in the same interval west of Sidmouth by Hounslow and McIntosh (2003), and their correlated data are also shown on Fig. 2. Some larger sampling gaps are present in the Hook Ebb Mudstone Mb (Fig. 3), and three of the magnetozones are defined by single samples (2 specimens each; SS2r.1n; SS3n.1r) in the Salcombe Mouth to Hook Ebb section (Fig. 3). Polarity data of Creer (1959) from the lower part of this section identifies the base of a normal polarity magnetozone some 17 m above a green sandstone level, which is presumably near the top of the Otter Sandstone, and normal polarity below the sandstone level, with an intervening reverse magnetozone some 17-22 m thick. These polarity changes are like our data, but reverse magnetozone (BS8r) is some double the thickness of Creer's. Lithological logs were not given by Creer (1959), so either; a) these differences relate to a thickness error, or b) the upper part of BS8r in Creer's data was too strongly overprinted by the LT overprint, that AF demagnetisation at 120 mT (and 3 years storage in zero field) failed to remove it.

The SS1n-SS3r polarity boundary coincides with the basal sandstone bed in the base of the Salcombe Mouth Mb, indicating there could be a hiatus at this level. Similarly, the

SS2r-SS3n polarity boundary coincides with a halite breccia bed so it could be there is a hiatus between samples MD1 and MD4 across this ~1 m breccia interval.

The 45 m of section at Strangman's Cove preserves 18 magnetozones, with three additional tentative reverse magnetozones in the upper part of the Little Weston Mudstone Mb (SS3n.2r, SS3n.3r, SS3n.4r; Fig. 4). This part of the Little Weston Mudstone Mb was one of the least well exposed parts of the MMG (at the time of sampling), and the sparser sampling probably inadequately represents the polarity changes. The high sampling density in the lower and mid parts of the DMF indicates frequent reversals, or a relatively condensed interval in the MMG. The Lincombe Sandstone Mb (a lenticular siltstone/sandstone body if evaluated using adjacent outcrops) is exclusively reverse polarity (SS4r; Fig. 4). The change in polarity across the base of the Lincombe Sandstone Mb could indicate a hiatus at its base. Likewise, the halite breccias in the section likely indicate a hiatus in the section at these levels (Fig. 4). An interval at -2.5 m with slickensides (Fig. 4) is a probable palaeosol. This occurs in an interval of strata that is infrequently exposed in the upper part of the Little Weston Mudstone Mb (172 -183 m in composite height; SI Fig. S1.3).

The stratigraphically higher but partially overlapping 45 m section at Littlecombe Shoot west displays dominantly reverse polarity with a single-sample normal magnetozone in the lowest Littlecombe Mudstone Mb (SS8r.1n; Fig. 4). Samples from the upper sandstone are of reverse polarity (magnetozone SS9n.1r; Fig. 5) embedded in a thicker normal polarity magnetozone SS9n, which extends into the base of the section at Littlecombe Shoot east (Fig. 5a). The magnetostratigraphy in the Littlecombe Shoot Mb may be more complex than the sampling indicates, because seven of the submagnetozones in this member are based on only single samples (but 2 specimens from each, e.g., basal part of SS9r; Fig. 5).

The section between Red Rock and Branscombe Mouth starts in reverse magnetozone SS9r (Fig. 6), like the upper-most sampled part at Littlecombe Shoot east, but passes up into normal polarity (SS10n, SS11n), which is dominant in the mid and upper parts of this section (Fig. 6). Two submagnetozones are defined by a single sample, one at the base of the Seaton Mudstone Mb (SS9r.3n), and one at ~48 m above the base of the Seaton Mudstone Mb (SS11n.1r; Fig. 6).

The Seaton Cliff section is dominated by normal magnetozone SS12n, but with three submagnetozones defined by single samples (SS12n.1r, SS12r.1r, SS12r.1n; Fig. 7).

The Haven Cliff section has well defined magnetozones, particularly those in the uppermost Seaton Mudstone Mb and throughout the Haven Cliff Mudstone Mb where sampling density is higher (i.e., HC2n; Fig. 8). The specimens from the BAF were

challenging to measure and analyse due to the weak NRM intensity (many <0.1 mA/m), larger directional scatter, and dominance of great-circle type behaviour (Fig. 8). Four magnetozones are defined by a single sample, with multiple specimens (HC1n.1r, HC1n.2n, HC2n.1r and HC3r.1n), and three tentative submagnetozones (HC2n.2r, HC3n.1r, HC3r.2n; half width bars in polarity column; Fig. 8) are defined by a single specimen. One sample has specimens of opposite polarity and is assigned unknown polarity (grey bar at -11 m; Fig. 8).

Overall, the MMG magnetostratigraphy has a moderate number of magnetozones defined by single samples (21 out of the total), which is a non-ideal situation, and could be rectified with detailed sampling of sparse intervals.

Discussion and synthesis

Timing issues in red-bed magnetisations

The fine-grained haematite (the pigment) which colours many red-bed successions generally has been generated over-long time intervals by oxic diagenesis. This pigment component often largely carries the overprint magnetisations or it is sufficiently fine-grained to acquire no persistent remanence. The specularite (haematite generally > 1μm in size) in red beds is responsible for the stable magnetisations either produced during deposition, during very early burial, or in some cases during longer-term diagenesis, like the pigment (see reviews by Butler, 1992 and Swanson-Hysell et al. 2019). Some of the issues connected with the 'red-bed controversy', which was most active in the late 1970-1980's, were also related to the incomplete demagnetisation methods (i.e. blanket demagnetisation) often employed at the time, which were unlikely to separate primary from secondary components and later diagenetic-related magnetisations. These have now been superseded by more complete demagnetisation approaches. It is clear from the work of Creer (1959, 1961) that the MMG contains both pigment and specularite. Likely, the LT component in the MMG is largely carried by the pigment, as evidenced by the often-rapid intensity decay during thermal demagnetisation and unblocking of this component (see SI). Isolation of magnetisations in randomly tilted intraformational intraclasts is the classic way to test for specularite components acquired prior to deposition (Swanson-Hysell et al. 2019). Intraclasts are rare in the MMG (and only of small size), so this method cannot be easily applied.

We infer that the ChRM in the MMG red-sediments is largely carried by detrital haematite deposited during deposition (or close to that time). This is based on: 1) The ChRM is carried by both haematite and magnetite in the DMF, which contains both normal and

reverse polarity intervals. The DMF red mudstones appear little different magnetically to other parts of the MMG. 2) The ChRM directions are of dual polarity with palaeopoles much like many other European Triassic sediments; 3) Magnetisations are simple in directional behaviour, unlike those inferred to be acquired over long-term intervals which tend to be more complex (Butler, 1992). 4) Magnetozones are straightforward to define, without many single-sample polarity intervals, which could be a characteristic of patchy diagenetic production of specularite.

However, it cannot be excluded that some of the specularite has been produced over longer time intervals. This could be responsible for the great-circle type behaviour seen in some specimens, so longer-term diagenetic-related magnetisations are not fully separated from near-depositional components when demagnetised. The wide dispersion in the declination of the poles to the great circles for the specimens with t-class ChRM's (SI Fig. S3.2) is consistent with contamination from rather dispersed secondary components, perhaps acquired over longer and variable time-intervals into the Brunhes (e.g., SI Fig. S3.1). Possibly some of the 6% of specimens that retain no ChRM are dominated by magnetisations from pigment or diagenetic specularite.

Age of the Sidmouth Mudstone Formation and international comparisons

Independent constraints on the age of the Sidmouth Mudstone Fm (SMF) are provided firstly by vertebrates, largely from the Chiselbury and Pennington Point members (and some older occurrences from the Otterton Ledge Member) of the underlying Otter Sandstone Fm (Benton et al. 1994; Spencer and Storrs 2002; Gallois 2005; Coram et al., 2017). The key taxon *Eocyclotosaurus* is largely known from the upper parts of the Otter Sandstone (Coram et al., 2017). The age of these vertebrate assemblages has been inferred by comparison to similar assemblages in better dated strata of the Röt Formation (in Germany) and the Holbrook Member (Moenkopi Formation, USA) described by Lucas and Schoch (2002). The Röt Formation in the CEB is early Anisian in age (Nawrocki and Szulc 2000; Szurlies 2007). From the Moenkopi Formation (in Arizona), magnetostratigraphy from the Holbrook Member suggests it has a late Anisian age range from magnetochrons MT4 to MT7, a correlation also constrained by (CA-TIMS) U-Pb detrital zircon dates (Haque et al. 2021; Fig. 10).

In addition, vertebrate assemblages like those of the Otter Sandstone Fm occur in the Bromsgrove Sandstone of the Midlands, which is inferred to be Anisian (Seyfullah et al. 2013), because the overlying MMG has Anisian age palynomorphs (Benton et al. 1994). In

contrast, fish remains from the Otter Sandstone Fm suggest a Ladinian age (Milner et al. 1990). The level of uncertainty in the widely inferred Anisian age for the Otter Sandstone Fm, based on the vertebrates alone is unclear. Indeed, some have emphasized the inherent uncertainties and flaws in the concept of land vertebrate faunachrons and their means of age control (Rayfield et al. 2009; Irmis et al. 2010; Martz and Parker, 2017)

Secondly, age is inferred from miospores in the uppermost SMF, DMF and basal Branscombe Mudstone (Baranyi et al. 2019). Two palynologically-productive samples some 38 m below the base of the DMF in the Wiscombe Park-1 borehole, were assigned to the early Julian Substage (earliest Carnian) by Baranyi et al. (2019), a position some 6 m above the base of the Little Weston Mudstone Mb (Gallois 2007).

The Little Weston Mudstone Mb palynology accords with the normal polarity dominance of this member, which characterises the early part of the Julian (Fig. 10). The underlying magnetostratigraphy from the remainder of the SMF seems a good match to the GPTS in the mid and late Ladinian (Fig. 10). However, there are differences in the presence of brief normal subchrons in MT11r, which are only seen from the Seceda core dataset (Maron et al. 2019; Hounslow and Muttoni 2010). Other marine sections containing MT11r such as Mayerling and Gammsstein-1 only have reverse polarity (Maron et al. 2019), like our data from magnetozone BS8r (Fig. 10). These correlations suggest the base of the SMF closely corresponds with the start of MT11r in the mid Ladinian.

The reverse polarity dominated mid and late Anisian (MT4r to MT8r) is a distinctive polarity feature of the Middle Triassic (Fig. 10). This MT4r-MT8r interval is primarily evidenced by well-dated magnetostratigraphies from the Mushcelkalk (Nawrocki and Szulc 2000), the upper Guandao section (Lehrmann et al. 2015; Li et al. 2018), and the Milne Edwards Fjellet section on Svalbard (Hounslow et al. 2008b). The coeval upper part of this interval (MT7 to MT8r) is also found in other sections from Italy, Greece, Austria, and Svalbard (Hounslow et al. 2008b; Maron et al. 2019). The MT4r to MT8r chron interval is most likely equivalent to the BS3r to BS6r magnetozones in the Otterton Ledge Mb of the Otter Sandstone Fm (correlation option-1 in Fig. 10). This correlation option gives a fair correspondence between the number and relative thickness of magnetozones in the BS6 to BS8n interval and the two possible GPTS interpretations for this interval. Option-1 (our preferred solution) places the base of the Ladinian close to the base of the Chiselbury Mb of the Otter Sandstone (Fig. 10).

The differences between the GPTS of Hounslow and Muttoni (2010) and Maron et al. (2019) in the MT4r-MT8r interval are due to use of the Guandao section data as the reference

section for the lower and mid parts of this interval by Maron et al. (2019). Whereas Hounslow and Muttoni (2010) used more datasets for this interval. Because of the uncertainty in this part of the GPTS, a second possibility is that the MT4r-MT8r interval represents BS3r-BS5r, shown as correlation option-2 in Fig. 10. Option-2 results in more changes in accumulation rate (if magnetochron thickness in the GPTS is a proxy for time) in the Otter Sandstone Fm than option-1. Also, option-2 gives two additional reverse magnetozones in BS7n.1n, BS7r which are not represented in MT11n. However, magnetochron MT11n is only partially represented in the Belvedere and Aghia Triada sections, with both displaying a tentative reverse submagnetozone near the base (Maron et al. 2019), so MT11n may contain more reverse subchrons than shown in these reference sections. The loss of time at potential hiatuses in the Otter Sandstone at the base of the Chiselbury and Pennington members appears to be small, although perhaps all three correlation options suggest part of MT8r (SC2r in GPTS-A) may be missing, based on the thinner reverse polarity of BS6r.

The statistical evaluation of these correlations shows that correlations to GPT-A (Option-1) gives the better and larger SMI (0.53), but the correlations to GPTS-B give the larger PSI value (Table 3). As a comparison the GPTS-A to GPTS-B statistics show a higher level of similarity, as would be expected, because both are constructed from mostly similar datasets. The median Euclidean distance is smaller (0.48) for the correlation to GPTS-B, suggesting this has some advantage over the correlations with GTS-A. All three correlation options pass the RV-test of similarity at >99% probability (P_{RV} <0.01; Table 3). The more problematic magnetozones (i.e., with larger d_i) for comparison are Anisian magnetochrons MT4r and MT5n using GPTS-B, and BS3r.2r, BS5r, BS6n.1n for GPTS-A (flagged in Fig. 10). All correlation options indicate magnetochrons MT12n and MT11 have larger d_i indicating these are more problematic comparisons.

Comparison to the Triassic of the Central European Basin (CEB)

In the CEB the Longobardian to early Carnian interval are assigned to the Grabfeld Fm (Bachmann and Kozur 2004; Nitsch et al. 2005; Hagdorn and Nitsch 2009), largely based on miospore correlations (Kürschner and Herngreen 2010). Regionally the Grabfeld Fm is divided into three units (lower, middle, and upper) with boundaries locally expressed as disconformities (Nitsch, et al. 2005), but in the Morsleben 52a core as correlative conformities. Sulphate bearing units largely occur in the Lower and Middle Grabfeld Fm, like those seen in the Hook Ebb Mudstone and Little Weston Mudstone members (Fig. 11). A magnetostratigraphy through the Grabfeld Fm in core Morsleben 52a and associated northern

CEB cores (Fig. 11), allowed construction of a composite for this formation (Zhang et al. 2020), which has a connected cycle-stratigraphy (Barnasch 2010). The magnetostratigraphy from the Lower and Middle Grabfeld Fm and upper part of the underlying Urfurt Fm shows a fair correspondence to the upper part of the SMF (Fig. 11). This suggests the maximum regressive surface in the Salcombe Mouth Mb may relate to the upper-most regressive interval in the Erfurt Fm, below the flooding surface expressed by the transgressive, marine Grenzdolomit horizon. This correlation is emphasised by the sulphate bearing interval between SS2r to basal SS3n and the dominance of coeval evaporites, typical (Nitsch et al. 2005) of the Middle Grabfeld Fm (Fig. 11). Possible hiatuses may be at the base of the Salcombe Mouth Mb and the base of magnetozone SS2n where there is coincidence of polarity boundaries and beds with distinctly differing lithology to underlying units. In the CEB the Urfurt Fm, unlike the overlying Grabfeld Fm contains sandstone beds, a simple comparison which also applies to the Salcombe Mouth Mb and the overlying Hook Ebb Mudstone pair of units. Therefore, as an approximation the interval from the base of the Pennington Point Mb to the base of magnetozone SS2n is coeval with the mid and upper parts of the Urfurt Fm (Figs. 10, 11), which has a strongly diachronous boundary with the underlying Muschelkalk (Franz. et al 2013)

Correlation of the MMG polarity data to the GPTS is ambiguous around the base of the Carnian. Firstly, miospores place the base of the Carnian below the productive samples in the Little Weston Mudstone Mb (Baranyi et al. 2019), and near the base of the Upper Grabfeld Fm in the CEB (Bachmann and Kozur 2004; Kürschner and Herngreen 2010). Secondly, uncertainty about the GPTS construction in the early Carnian (Julian-1 interval) also leads to duplicate options for correlations of magnetozones SS3n and MK2n (Fig. 11). The most likely correlation for the bases of SS3n and MK2n is with the base of UT1n in both GPTS-A and GPTS-B (Fig. 11). If the single specimen of conodont *Paragondolella polygnathiformis* (conodont proxy for the base of the Carnian; Rigo et al. 2018) found in the Carnian GSSP at Stuores is representative of its first appearance, then UT1n and UT2n may be duplicates in GPTS-B, and instead magnetochron MA5 (in GPTS-A) may be representative of this interval (Fig. 11). This would suggest SS2r and MK1r are the likely equivalents of MT13r (and MA4r), a magnetochron which so far only has a thickness/duration estimate from the Mayerling section (Gallet et al. 1998).

The upper part of magnetozone SS3n in the Little Weston Mudstone Mb has insufficiently detailed sampling to properly define a polarity stratigraphy. However, by comparison to the upper part of the Grabfeld Fm, it is clear this interval is either condensed,

or contains a hiatus. The most likely candidates for either of these scenarios are the palaeosol at 179 m or its underlying halite collapse breccia (Fig. 11). If a hiatus, this may be coeval with a disconformity often inferred at the base of the Upper Grabfeld Fm (Bachmann and Kozur 2004; Hagdorn and Nitsch 2009; Kozur and Weems 2010).

Age of the Dunscombe Mudstone Formation (DMF) and international comparisons

Independent evidence of the age of the DMF are firstly provided using miospores from the Strangman's Cove section, in which Baranyi et al. (2019) placed the Julian-Tuvalian boundary around the upper boundary of the DMF. Their miospore data from the body of the DMF suggest that most of this formation is late Julian (or Julian) in age. Warrington (1971) similar concluded that palynomorph assemblages from the DMF were Carnian in age, and Fisher (in Jeans, 1978) recognised older and younger Carnian palynomorph assemblages with the boundary between them placed within the Lincombe Sandstone Mb. Warrington (1997) also inferred a Carnian-age in two samples from the Lyme Regis Borehole, which probably come from the DMF (Gallois 2006). However, the precision with which the Julian and Tuvalian substages can be identified with miospores in the MMG is uncertain, because as noted by Baranyi et al. (2019), miospore occurrences are often diachronous between the Triassic Germanic and Tethyan realms, and independent age control is poor for miospores from the inferred Tuvalian and Norian of the Germanic realm (Kürschner and Herngreen 2010). Characterising the Carnian-Norian transition using miospore assemblages more generally is also problematic (Cirilli 2010; Lucas et al. 2012; Hounslow et al. 2021b).

Secondly, a single specimen of the spinicaudatan, *Laxitextella multireticulata* (Reible) was found in the Lincombe Sandstone Mb from fallen blocks at Weston Mouth (Kozur in Gallois 2019). This species also occurs in the Middle and Upper Grabfeld Fm of the CEB (Geyer & Kelber, 2018), and from the Upper Meride Limestone of the southern Alps (Kozur & Weems, 2010). The Upper Meride limestone is early Longobardian in age (Stocker et al. 2012), currently providing the best age calibration of *L. multireticulata* . However, the range of *L. multireticulata* is unknown in detail, and more 'advanced forms' have been described, similar to the younger *L. laxitexta*, which is known to range into the Norian (Geyer & Kelber, 2018). Until more is known about the age range of *L. multireticulata* a single specimen from the DMF cannot be confidently used to infer precise ages.

Thirdly, age can be inferred using negative carbon-isotope excursions (CIE) found in the DMF both in the Strangman's Cove section and the Wiscombe Park boreholes (Miller et al. 2017; Baranyi et al. 2019; marked on Hook Ebb-Strangman's Cove section in Fig. 12 as

DIE#). These provide additional means of correlation to marine sections with better age control. The Carnian possesses several CIE in the Julian which are in part well calibrated to biostratigraphy (Mueller et al. 2016; Dal Corso et al. 2018; Lu et al. 2021; Mazaheri-Johari et al. 2021; Li et al. 2022). These are marked on the Ogg et al. (2020), GPTS-A in Fig. 12 (as J1 to J4); although these are less well-calibrated to magnetostratigraphy. CIE also occur in the Tuvalian and basal Lacian interval (Jin et al. 2019; Hounslow et al. 2022a; marked on the GPTS-B column (T1 to L1) in Fig. 12) and are better calibrated to magnetostratigraphy.

The magnetostratigraphy from the late Tuvalian and Julian is generally well characterised by section-based studies from Turkey, Italy, Austria, Slovakia and China (Hounslow and Muttoni 2010; Maron et al. 2019; Figs 11, 12). However, the magnetostratigraphy of the early Tuvalian (Tuvalian-1; Fig. 12) is less certain, and one option is to project the poorly-dated Stockton Formation dataset (Newark Supergroup, E-numbered magnetozones) into the mid Carnian (Figs. 12, 14). This option is used in GPTS-A (Fig. 12) and by Zhang et al. (2020), based on magnetostratigraphy from the northern CEB cores. However, Hounslow et al. (2022a) have proposed a rather different polarity scale for the Tuvalian (GPTS-B; Fig. 12), based partly on polarity datasets from Svalbard and constrained by CIE correlations in the Tuvalian.

In terms of geomagnetic polarity, the most distinctive feature of the Lacian Substage is the dominance of reverse polarity (Newark magnetozones E8r-E12r; chrons UT13r-UT16r; Fig. 14). This clearly associates the dominant reverse polarity in the top of the DMF and lower Littlecombe Shoot Mb (SS7 to SS8r) to the Lacian (Figs. 12, 15). This correlation places the base of the Norian within SS6r.1n or SS7n in the upper part of the DMF (Fig. 12). This part likely has missing intervals at the halite collapse breccias in the section (breccias in SS6-SS7 magnetozones). The preferred correlations shown in Fig. 12 (magnetozones SS5r and SS6n to GPTS-B) are based on the correlation of the DMF isotope excursions DIE4, DIE5 to CIE (T5+T6) and T4 respectively (Fig. 12). Magnetozones SS5n and SS6n may additionally correspond with magnetozones MK5n.1n and MK5n.2n in the Weser Fm from the northern CEB cores (upper red correlation lines in Fig.12).

The Little Weston Mudstone Mb and basal DMF are normal-polarity dominated and hence the Julian-1 magnetochron interval UT1n- UT2n in GPTS-A, may correlate with the pattern of polarity changes inadequately represented by the sampling in this part of the MMG (Fig. 12). Overlying chron UT2n (blue labels on GPTS-A) is a reverse polarity dominated interval (MK3r-MK4r at Morsleben; SS3r-SS4r in the DMF), which is probably equivalent to the UT6r - UT9r interval in the GPTS-B (based on data from Svalbard and the Pignola-2

section; Maron et al. 2017; Hounslow et al. 2022a). In the DMF the isotope excursion DIE-3 likely correlates to the J3+J4 excursions (Mazaheri-Johari et al. 2021) of Julian-2 age (black correlation line in Fig. 12). Based on the association of normal polarity around DIE-1, and the dominantly reverse polarity in UT3r-UT4r, it seems less likely that DIE-2 is the equivalent of excursion J2 known from the earliest Julian-2 (Fig. 12). A better alternative is that a missing interval may be present at the halite collapse breccia in SS3r, and DIE-2 and DIE-1 are probably older CIEs within Julian-1 (e.g., as in Mueller et al. 2016). This suggests the reverse polarity of the Lincombe Sandstone Mb is coeval with that of the Stuttgart Fm in the Morsleben cores, and both are early Tuvalian in age. Since the polarity changes across the base of the Lincombe Sandstone Mb, this level could be a minor hiatus/missing interval (Fig. 13) because this sandstone has a channel-like (but not clearly down-cutting) geometry (Porter and Gallois 2008).

A magnetostratigraphy from the Polish 'Schilfsandstein' (Nawrocki et al. 2015, Wójcik et al. 2017) has indicated three normal polarity submagnetozones, in a dominantly reverse polarity interval like the style of polarity changes in the Stuttgart Fm of the Morsleben cores; although in Poland fragmentary recovery of polarity from over and underlying strata precludes any detailed correlation. Refinement of the association of carbon isotope excursions with respect to the magnetostratigraphy in the late Julian would assist with international correlation at a finer scale.

The statistical assessment of these correlations shows that SMI is largest for the DMF to Morsleben correlations, with the largest PSI for the DMF to GPTS-B correlations (Table 3). This later correlation also has the smallest median d_i (at 0.77), and the larger probability of association (more than 99% chance of association). This suggests statistically the correlation to GTPS-B is the better, with the most problematic intervals for comparison being SS4r, SS6n and SS6r.1r (Fig. 12). For comparison, the GPTS-A to GPTS-B correlations have smaller SMI and PSI indices, indicating poorer relationships. This is probably because these are constructed from entirely different polarity datasets through the Tuvalian.

Comparison to the Stuttgart and Weser formations of the CEB

At a simple-level, the sandstone and calcareous 'group' divisions of Jeans (1978) for the DMF (Fig. 13) are like the halite-sandstone-halite bearing 'sandwich' of the Stuttgart Fm and its adjacent formations in the CEB (Bachmann et al. 2010; Hagdorn and Nitsch 2009). The presence of dolostone beds in both successions also enhances the degree of similarity to the DMF, with flooding surfaces in the CEB usually represented by dolostone beds. Using the

magnetostratigraphic correlations and the events and cycles of Barnsach (2010) from the Morsleben 52a core, and Franz et al. (2014) from more widely in the CEB, some of these flooding surfaces may have coeval expression in the Devon successions; particularly those of the Neubrandenburg, Beaumont and Lehrberg beds (Figs. 12, 13). However, the small cycles of Barnsach (2010) do not have a clear synchronous expression in the DMF.

The set of halite-dissolution breccias in the Upper Weser Fm from the Moresleben 52a core, and those near beds K and J in the DMF may be indicative of coeval flooding events around the base of the contemporary SS7r and MK5r.1r magnetozones (Fig. 13). Indeed, three widely distributed halite units are known in the CEB in the Weser Fm (Bachmann et al. 2010), which may be coeval with the three collapse breccias seen in the upper part of the DMF between 26- 30 m (Fig. 13). If these relationships are correct, the boundary between the Weser and Arnstadt formations (the D4 or early Kimmerian-I unconformity; Feist-Burkhardt et al. 2008) may be coeval with the sequence boundary at bed N in the base of the Littlecombe Shoot Mudstone Mb (Fig. 13).

Despite episodic eustatic marine influence on the Middle Keuper in the CEB (sourced through a southern gateway; Bachmann et al. 2010; Franz et al. 2014), and the correlations proposed in Fig. 13, there is no direct evidence for marine intervals in the Wessex Basin in this interval. If there was, this would likely be a route from the SW through the SW Approaches basins (McKie 2017). More detailed investigation of the dolostone intervals in the DMF may shed light on this possibility.

Rhaetian and upper Norian: Blue Anchor Formation (BAF), Seaton and Haven Cliff Mudstone members

In addition to the miospore data discussed above in the base of the Branscombe Mudstone Fm, palynomorphs from the upper parts of the BAF suggest a Rhaetian age (Warrington 1997, 2005). These Rhaetian assemblages are comparable to those from the St Audrie's Bay section in North Somerset, where similar assemblages continue into the Penarth Group (Hounslow et al. 2004; Bonis et al. 2010).

Alternative GPTS's have been proposed for the mid Norian to early Rhaetian. Firstly, that of Kent et al. (2017) and Maron et al. (2019) utilise a reference scale largely from the Newark Supergroup magnetostratigraphy (Fig. 15), with the chronostratigraphy imported using a correlation to selected marine sections with magnetostratigraphy. Secondly, is the GPTS-B (Fig. 14) a marine-section based composite of Hounslow and Muttoni (2010), which is updated here with new data for the Sevatian to early Rhaetian (see SI Fig. S5.1).

Correlations between GPTS-B and some key non-marine sections for this interval are shown in Fig. 14, with the addition of a composite for the upper Chinle Formation (its construction is outlined in SI section 5.1). GTPS-B provides the better base to understand the likely chronostratigraphy of the upper parts of the MMG (Fig. 15).

The magnetostratigraphy from the Haven Cliff section is closely comparable to that from the St Audrie's Bay section (Fig. 15), even down to the reverse submagnetozones in the coeval mid parts of HC2n and SA4n and the probably coeval reverse submagnetozones SA3n.1r and HC1n.1r (Fig. 15). The relative thicknesses of coeval magnetozones varies somewhat between these sections, but both are closely comparable to the magnetostratigraphy from the upper Passaic Fm (E16n to E19 magnetozones) of the Newark Supergroup (Fig. 15). These relationships are also consistent with an unanchored astrochronology from the MMG at St Audrie's Bay and its synchronisation with the Newark Supergroup cyclostratigraphy (Kemp & Coe, 2007). Newark magnetozones E15 to E19 are widely associated with late Norian (Sevatian age strata) and their transition into the earliest parts of the Rhaetian (Fig. 14; SI Figs. S5.1, S5.2; Maron et al. 2019). Based on these magnetostratigraphic correlations, the two proposed choices for the base of the Rhaetian (NRB1 and NRB2 in Figs. 14, 15), place the Rhaetian boundary either in the upper part of the Haven Cliff Mudstone, or within the lowest part of the BAF (Fig. 15). This indicates that magnetozone HC1n (in the Haven Cliff section) should equate to Newark magnetozone E16n, St Audrie's Bay magnetozone SA3n and magnetochron UT22n.

The age of NRB1 based on the anchored astrochronology from Austrian sections places it at ~208 Ma (Galbrun et al. 2020), consistent with both the placement of NRB1 (from magnetostratigraphic correlations in Fig. 14) and the anchored astrochronological age (207.6 Ma; Kent et al. 2017) for the base of E18r in the Newark Supergroup (Fig. 14). Based on the biostratigraphy from the Chinle Fm; the Redonda Mb (magnetozone CC8n-CC10n interval; Fig. 14) is usually assigned a Rhaetian age (Zeigler and Geissmann 2011; Heckert and Lucas 2015). In addition, the similarity in Chinle Fm detrital zircon ages to the Newark-Hartford APTS ages between CC5r-CC9n (E14r- E18n in Newark-Hartford APTS) indicates a close correspondence between the polarity patterns in the Chinle Fm and Newark Supergroup (top left Fig. 15), and the corresponding interval in GPTS-B. This locates NRB1 near the base of magnetozone CC9r in the Chinle Fm composite, and consequently robustly demonstrates the international consistency in the polarity patterns in this Sevatian to early Rhaetian interval, from magnetochrons UT20r to UT24r (Fig. 14).

In the Wessex Basin the interval encompassing the Seaton Mudstone Mb to the base of the BAF is regionally rather consistent in thickness (Gallois 2001; 2003), with the nearest borehole to the coastal outcrops (at Marshwood) showing ~ 145 m (Gallois 2003) for this interval. This is used as a thickness estimate for the Seaton Mudstone Mb in the coastal outcrops. We consider that magnetozone SS12n is not the equivalent of either HC1n, SS11n or SS10n, also in the Seaton Mudstone Mb, for the following reasons. Firstly, projecting the top of the Seaton section (above the sampled interval), based on a test of the equivalence of SS12n and HC1n, would indicate that the Haven Cliff Mudstone Mb should be close to the top of the Seaton section; yet there is no evidence of the Haven Cliff Mudstone Mb in the Seaton fault blocks. Secondly, the mudstones from the Seaton Mudstone Mb in the Branscombe section, have cm-scale sandy laminae which are absent from the Seaton Cliff section, suggesting these sections are not lithologically equivalent. Thirdly, SS11n is some 23 m thick compared to 14 m for SS12n and also have no consistent lithological matches using the detailed logs (see the SI). Fourthly, SS10n (11 m thick) is a similar thickness to SS12n, yet any lithological match, using the assumption of magnetozone equivalence is poor. Also, this match would require the Red Rock Gypsum Mb to be shortly below the Seaton section, a situation for which there is no evidence in the ~40 m of poorly exposed outcrop to the west in the Axe valley fault blocks. The later three arguments suggest that magnetozone SS12n is not equivalent to magnetozones SS11n or SS10n seen in the Branscombe Mouth section. Using the above thickness estimate of the Seaton Mudstone Mb and the cumulative sampled thicknesses of this member, indicates that ~26 m of this member remains unsampled from this study.

Therefore, magnetozone SS12n is inferred to be magnetochron UT21n, as also seen in the basal part of the St Audrie's Bay section (SA2n; Fig. 15 and E15n in the Newark APTS). Additional support for this is that the pattern of polarity changes in the Seaton Cliff section is like that in magnetozone CC6n in the Chinle Fm. Also, both the Pizzo Mondello and Kavur Tepe sections have reverse sub-magnetozones in UT21n, like those detected within CC6n and SS12n, similarities strengthening this proposed correlation.

The Branscombe Mudstone Formation and the middle Norian (Alaunian)

The interval from magnetozones SS9n to SS11n contains three major normal polarity intervals (SS9n, SS10n, SS11n), like both the marine-based GPTS-B, and the interval CC4n to CC5n in the upper Chinle Fm composite (Fig. 15). For this reason, and the constraints from overlying and underlying polarity patterns, we correlate the interval SS9n - SS11n with

UT18n - UT20n (Fig. 16). However, this interval is unlike the Newark Supergroup APTS, which has only two thick normal magnetozones over this interval. This suggests that the Newark Supergroup magnetozone interval E14n-E14r may be incomplete (marked in Fig. 15). Other than the marine-based sections over this interval, there are also coeval non-marine sections from the Fleming Fjord Group and the Los Colorados Fm (Fig. 14). The middle Norian interval has also been evaluated in cores and sections from the Holy Cross Mountains in Poland (Wojcik et al. 2017) through the Arnstadt Formation, which displays a pattern of polarity reversals similar in overall style to the UT18n to UT21n, although the fragmentary recovery of polarity precludes a detailed comparison.

The magnetostratigraphy from the Fleming Fjord Group does not extend to older strata to confirm the polarity pattern UT18n-UT20n, but matches well with GTPS-B (Fig. 14), using the preferred correlation of Kent and Clemmenson (2021) and the coeval parts of the Newark APTS. Some 60 m below the base of the Colorados Fm is a precise ID-TIMS zircon date (i.e., 221.8 ±0.3 Ma), which when compared to the Chinle Fm composite (with its detrital zircon dates), suggests the magnetostratigraphic match shown as Option-2 in Fig. 14. The correlation shown as Option-1 was that preferred by Kent et al. (2014) based on the less precise Ar/Ar date (225.9 ±3.7 Ma), which also gives a satisfactory polarity match between the upper part of the Colorados Fm and magnetochrons UT18n to UT20n (Fig. 14), but unsatisfactory match using the more precise ID-TIMS date.

The proposed missing interval in the Newark APTS (marked in Figs. 14, 15) corresponds with an abrupt upwards decrease in accumulation rate near the boundary of magnetozones E14n-E14r (from ~24 to 14 cm/ka), based on the astrochronology using depth rank and colour (Meyers 2019; Wang et al. 2022). This suggests an abrupt and major shift in sedimentary regimes at the proposed position of the missing interval.

These strands of evidence, along with the new data from the MMG, although not conclusive by themselves, collectively support the Newark APTS to GPTS-B correlation shown in Figs. 14, 15. Significantly this solution may solve the long-running debate (Gallet et al. 2003; Muttoni et al. 2004; Hounslow and Muttoni 2010; Galbrun et al. 2020; Ogg et al. 2020) about how the Newark APTS in the mid Norian relates to the marine-based GPTS. This conundrum is fundamentally linked to ambiguity in how to relate the biostratigraphy of the Newark Supergroup to international stages (Tanner and Lucas 2015; Galbrun et al. 2020). With the solution proposed here, the chronostratigraphic and biostratigraphic divisions of the Norian are now satisfactorily aligned with the astrochronology from the Newark Supergroup

(Fig. 14). This interpretation indicates the Branscombe Mudstone Fm contains the full complement of magnetochrons known from the early Norian to the early Rhaetian (Fig. 15).

The statistical evaluation of these correlations shows that the GPTS-B to Chinle composite show the strongest association with the largest SMI, PSI and smallest median d_i (Table 3). The Newark Supergroup APTS to Chinle composite shows a similar level of association as between the GPTS-B and the MMG, with all three of these having a probability of association > 99% (P_{RV} <0.01; Table 3). Magnetozones SS9n.2n, SS9r.3r, HC2n.2n and HC2r, have the larger d_i indicating more divergence of these zones. These statistics support the overall correlation relationships proposed above. They also suggest that in spite of the very different tectonic and sedimentologic settings of these three terrestrial successions, they all share a common record of polarity changes which is not impacted to a major extent by hiatus. This does not mean that these successions are complete, as inferred at the hiatuses in the MMG, it may just indicate that at the time-scale of polarity changes, the sediment record is sufficiently complete to approximate the relative length-scales of most major magnetochrons.

Controls on accumulation rates in the Mid-Late Triassic in Britain

With the proposed correlation to the polarity scales, we estimate accumulation rates in the Otter Sandstone Fm and Mercia Mudstone Group. Attachment of polarity boundaries to chronometric time used the Bayesian age model of Hounslow et al. (2018) for the Middle Triassic to early Carnian (polarity chrons up to UT5n). The late Carnian to Rhaetian interval used the Newark Supergroup astrochronology of Kent et al. (2017) and Wang et al. (2022), which give only slightly different ages for the magnetochrons. That using the Bayesian age model and Kent et al. (2017) ages is referred to as age model-1 and that using the Bayesian age model and Wang et al. (2022) ages is model-2 (Fig. 16). As an alternative to the late Ladinian-Carnian part of these models we also use the chronometric scale proposed by Zhang et al. (2020). Alternatively, Miller et al. (2017) proposed a 1.09 Myr duration (based on an astrochronology from the Wiscombe Park borehole) for the interval from the base of the DMF to near the correlated base of magnetozone SS6r. This same interval gives a duration of 7.0 Myr and 8.1 Myr using age model-1 and the Zhang et al. (2020) age model respectively. Likely the ca 8 m cycles identified by Miller et al. (2017) are closer to 2.4 Myr eccentricity cycles.

Using these three age models, instantaneous accumulation rates between polarity boundary ages were estimated (data points in Fig. 16). The accumulation rates are not

significantly impacted by the inferred missing interval in the Newark Supergroup APTS, because rates are based on chron durations. Since the age estimates of polarity boundaries in the MMG are likely biased by sampling resolution and fidelity of polarity recovery, and by uncertainties in the chronometric estimation of magnetochrons in the age models, we have averaged the accumulation rates (using a 3-point geometric mean) for the model-1 and Carnian age models (Fig. 16). The alternate Carnian age model does not significantly modify the accumulation rates. These accumulation rates also include the potential missing time at the likely hiatus levels identified.

These data indicate thye Devon coastal succession overall has a baseline accumulation rate of 30-50 m/Myr throughout this interval, which presumably relates to typical subsidence and accommodation space availability in this part of the Wessex Basin. There are several deviations from the baseline rates (Fig. 16).

In the upper part of the Otterton Ledge Mb there is a reduction of accumulation rate to ~10-20 m/Myr, which corresponds with the upper part of the 2nd fluvial cycle of Newell (2018a) in this member. This reduction in accumulation rate corresponds with the Anisian-Ladinian boundary interval. In the northern part of the CEB the Illyrian-Fassanian boundary also corresponds with the initial regression of the Lower Keuper (Erfurt Fm) over the marine limestones of the Upper Muschelkalk. In the southern CEB, with a stronger marine influence, this diachronous regression was completed in the late Fassanian (Franz et al. 2013). The facies shift expressed by Muschelkalk-Keuper transition is the major environmental change of the Middle and Upper Triassic Germanic facies in Europe. Our dating shows that the Otter Sandstone-MMG transition (Chiselbury to Sid Mudstone members) is coeval with this diachronous environmental shift. However, the Wessex Basin was not hydrologically connected to the CEB (McKie 2014) in this interval. More importantly in the Wessex Basin this transition shows a transgressive relationship. The transgressive character is shown most clearly above the sequence boundary (Gallois 2005; Newell 2018a) at the base of the Pennington Point Mb, which is an erosive transgressive surface with an overlying transgressive system tract (TST) extending into the Salcombe Hill Mudstone Mb (Fig. 16). The nature and boundaries of the Pennington Point Mb indicate it genetically belongs to the MMG successions (Gallois 2003). Although the CEB and the Wessex Basin have opposite sequence stratigraphic tracts in this age interval, they both show a flood of silt-and clay-grade siliclastics overwhelming carbonate and fluvial sand-prone systems respectively. In the CEB the source of sand was predominantly from Scandinavia in the Keuper (Paul et al. 2008), but from Cadomian basement rocks of the Armorican Massif throughout the Otter Sandstone Fm

(Morton et al. 2013). The likely common factor linking the incoming Erfurt Fm and MMG successions was an increasing aridification and greater supply of loessic silt and clay during the transition into the Ladinian. Loessic silt may have had a bigger impact on the dry-playas (McKie 2017), of the Sidmouth Mudstone Fm, than in the CEB, where wet-playa facies tend to dominate in coeval mudstones (Aigner and Bachmann, 1989; McKie 2017).

The DMF shows the largest reduction in accumulation rates, which began in the upper part of the Little Weston Mudstone Mb and shows recovery through the lower part of the Littlecombe Shoot Mudstone Mb (Fig. 16). This dramatic reduction in accumulation rates is likely associated with Carnian environmental changes that are best understood in the mid-Carnian (Dal Corso et al. 2020). Probable causes of this large reduction in accumulation rate are:

A. **Fine-sediment bypass**: the sink for detrital fines was largely directed to basin depocenters with sand- grade material remaining at basin margins and within channel systems that are directed to basin depocenters (Porter & Gallois 2008). Certainly, during the Carnian much greater thicknesses of halite accumulated in depocenters in the Wessex Basin (Gallois 2003), probably coeval with the halite-breccia intervals above and below the sand-bearing interval in the DMF. The basin-flank halite deposits were likely re-worked during ephemeral periods of high groundwater and re-charged to depocenters (McKie 2017), as inferred in the CEB by Franz et al. (2014). A similar style of Carnian-age, by-pass basin-filling is seen in the CEB, giving distinctive depocenter sags from filling of accommodation space, particularly during the interval of the Grabfeld Fm (Bachmann et al. 2010). Alternatively, this geometry is commonly inferred as a pulse of renewed extensional tectonics (Bachman et al. 2010; McKie 2017), rather than flank condensation with sediment by-pass and accommodation spacing filling. Rejuvenated extensional subsidence does not concur with the observed reduction in basin flank accumulation rates.
B. **Shut down in fine sediment supply** from hinterlands and desert margins: This comes about by lack of supply, perhaps caused by enhanced vegetation trapping in hinterland soils or lakes, so that loessic sources areas ceased to supply the same volume of fines, yet the limited supply of fluvial-derived sand+fines continued. At the present-day, desert dusts in low latitudes are principally supplied from desert margins, with the largest single sources being from deflation of lake basins (Bristow et al. 2009), providing seasonally phased supplies of dust (Middleton 2017; Li et al. 2020).

The conundrum of the mid Carnian in western European Germanic-style basins is the sedimentological indication of sandy, wetter lacustrine and fluvial systems in the mid Carnian (Porter and Gallois 2008; Kozur and Bachmann 2010; Franz et al. 2019; Ruffell et al. 2015), yet palynological data suggest similar dry-land vegetation (xerophytes) throughout the Carnian crisis (Baranyi et al. 2019; Franz et al. 2019). One way to balance this apparent dichotomy is a flashier riverine input, so that ephemeral/seasonal storms deliver the sand-grade material, yet ground water and soil moisture is not maintained throughout the growing season, so hygrophytic flora was not able to fully develop, a situation which has been proposed for the Carnian of the Wessex Basin (Baryani et al. 2019). A greater contribution from xerophytic regionally-derived pollen rain, may also have limited the ability to detect local hygrophytic vegetation that developed during these brief wetter intervals. This imbalance may have been enhanced by spread of hinterland xerophytes, into previously hyper-arid areas, due to seasonally more humid, but annually essentially dry desert margins. This may be linked to point B above. Franz et al. (2014) have proposed an alternative scenario for the Stuttgart Fm in the CEB invoking marine transgressions as the forcing factor for local development of hygrophytes, which is not applicable in the Wessex Basin due to a lack of evidence for marine influence.

The dry playa facies of the Branscombe Mudstone Fm do not reach maximum accumulation rates until the mid Norian, at around the position of the Red Rock Gypsum Mb, which likely represents an interval of wet-playa facies (i.e., facies divisions of McKie 2017), probably marking a maximum flooding surface. A second maximum flooding surface in the late Alaunian corresponds with a distinctive high gamma pick seen consistently on log profiles in the Wessex Basin (Gallois 2003; Newell 2018b). This likely relates to an interval with cm-thick black mudstones which are exposed on the low tide beach below the Seaton section (so likely in magnetozone UT20r; Fig. 15). This ‘high gamma event’ heralds a decline into lower accumulation rates in the upper Seaton Mudstone Mb, and the development of wet-playa facies in the Haven Cliff Mudstone Mb and BAF. Since the units above the Red Rock Gypsum Mb are consistent in thickness across the Wessex Basin (Gallois 2003), the likely reason for the accumulation rate decrease may be increasing humidity into the Sevatian and early Rhaetian, impacting sediment supply, like outlined in B) above.

Conclusions

1. A magnetostratigraphy is recovered from most of the 474 m of the Mercia Mudstone Group from coastal outcrops in the type-section of the group. Some outcropping intervals

need refining, because the sampling density is inadequate to robustly define some thin magnetozones.

2. Characteristic magnetisations are largely carried by haematite, but with some rare levels in the Dunscombe Mudstone Fm where magnetisations are carried by magnetite.
3. The magnetostratigraphy can be correlated with better dated marine and non-marine sections elsewhere, and thus establishes the first accurate chronostratigraphy for the MMG. The interval studied ranges from the early Ladinian (mid Fassanian Substage) to the early part of the Rhaetian. Other geochronological tools applied to the MMG, such as cyclostratigraphy, may assist in improving and adapting the proposed age assignments.
4. Using our data and a collective assessment of magnetostratigraphies from other Norian sections, allows us to proposal a solution to the long-standing debate about the polarity pattern through the mid Norian.
5. The interval of the Hook Ebb Mudstone to Little Weston Mudstone members is closely comparable in facies and age to the Grabfeld Fm in the CEB.
6. A comparison of our magnetostratigraphy to that from the Middle Keuper Group of the CEB indicates a close similarity to the Dunscombe Mudstone Fm, including the equivalence of sandstone-bearing intervals of the Lincombe Sandstone Mb and the Stuttgart Fm of the CEB. The coeval nature of some flooding surfaces and the timing of evaporites between the Dunscombe Mudstone Fm and the Weser Fm of the CEB indicates synchroneity of some climatic events between these two basins. Additional work on the more sparsely-sampled upper part of the Little Weston Mudstone Mb would improve the chronology of this apparent Julian age interval.
7. Using the derived age models of the Devon succession, accumulation rates are dramatically lower from the mid Carnian, but show recovery in the early Norian. These changes reflect sediment by-pass on the flanks of the Wessex Basin and a major slowdown in fine sediment delivery. This was likely due to limited aeolian supply of dust from shrinkage of the hyper-arid source areas, caused by seasonal climatic humidification from the mid Carnian to earliest Norian.
8. The data detailed here enables environments and habitats in the Middle-Late Triassic in Britain to be better related to other widely geographically spaced localities and it should improve details of palaeogeological maps, bringing the British Triassic succession into much better time-alignment with the Germanic Triassic.

Acknowledgements Magnetic measurements were also performed by Guy Jenkins, Paulette Posen and Vassil Karloukovski. Guy Jenkins, Paulette Posen and Julian Andrews assisted with early fieldwork. Neil Jones kindly supplied MWH with logs of some of these sections during initial field work. We thank Geoff Warrington and Richard Edwards who aided preliminary investigations, and Rob Coram for stratigraphical advice. The reviewers Spencer Lucas, John Geissman and the Editor provided constructive comments on drafts that led to improvements in the present account.

Funding BGS grant GA/98E/31/A1 initiated this work. Part of the fieldwork and measurements on the Seaton section was funded by a NERC grant to Gordon Walkden with some additional fieldwork support from Wolfram Kürschner. Part of the work at Haven Cliff was funded by Leverhulme Trust grant F/204/W.

References

Aigner, T. and Bachmann, G.H. 1989. Dynamic stratigraphy of an evaporite-to-red bed sequence, Gipskeuper (Triassic), southwest German Basin. *Sedimentary Geology*, 62, 5-25.

Bachmann, G.H. and Kozur, H.W. 2004. The Germanic Triassic: correlations with the international chronostratigraphic scale, numerical ages and Milankovitch cyclicity. *Hallesches Jahrbuch für Geowissenschaften*, 26, 17-62.

Bachmann, G.H., Geluk, M.C., Warrington, G., Becker-Roman, A., Beutler, G., Hagdorn, H., Hounslow, M.W., Nitsch, E., Rohling, H.G., Simon, T. and Szulc, A. 2010. Triassic. *In:* Doornenbal, H. and Stevenson, A. (eds) *Petroleum geological atlas of the Southern Permian Basin area*. EAGE, 149-173.

Baranyi, V., Miller, C.S., Ruffell, A., Hounslow, M.W. and Kürschner, W.M. 2019. A continental record of the Carnian Pluvial Episode (CPE) from the Mercia Mudstone Group (UK): palynology and climatic implications. *Journal of the Geological Society*, 176, 149-166.

Barnasch, J., 2010. *Der Keuper im Westteil des Zentraleuropäischen Beckens (Deutschland, Niederlande, England, Dänemark): diskontinuierliche Sedimentation, Litho-, Zyklo- und Sequenzstratigraphie.* Schriftenreihe der Deutschen Gesellschaft für Geowissenschaften, 7-169.

Benton, M.J. 1997. The Triassic reptiles from Devon, *Proceedings of the Ussher Society*., 9**,** 141-152.

Benton, M.J., Warrington, G.., Newell, A.J. and Spencer, P.S. 1994. A review of the British Middle Triassic tetrapod assemblages. *In*: Fraser, N.C and Sues, H-D. (eds), *In the Shadow of the Dinosaurs*, 131-160. Cambridge University Press, Cambridge.

Benton, M.J., Cook, E. and Turner, P. 2002. *Permian and Triassic Red Beds and the Penarth Group of Great Britain*. Geological Conservation Review Series, No. 24. Joint Nature Conservation Committee, Peterborough.

Bernardi, M., Gianolla, P., Petti, F.M., Mietto, P. and Benton, M.J. 2018. Dinosaur diversification linked with the Carnian Pluvial Episode. *Nature Communications*, 9, 1-10.

Bonis, N.R., Ruhl, M. and Kürschner, W.M. 2010. Milankovitch-scale palynological turnover across the Triassic–Jurassic transition at St. Audrie's Bay, SW UK. *Journal of the Geological Society*, 167, 877-888.

Brayard, A., Escarguel, G., Bucher, H., Monnet, C., Brühwiler, T., Goudemand, N., Galfetti, T. and Guex, J. 2009. Good genes and good luck: ammonoid diversity and the end-Permian mass extinction. *Science*, 325, 1118-1121.

Bristow, C.S., Drake, N. and Armitage, S. 2009. Deflation in the dustiest place on Earth: the Bodélé Depression, Chad. *Geomorphology*, 105, 50-58.

Broglio Loriga, C., Cirilli ,S., De Zanche, V., di Bari, D., Gianolla, P., Laghi, M.F., Lowrie, W., Manfrin, S., Mastandrea, A., Mietto, P., Muttoni, C., Neri, C., Posenato, C., Rechichi, M.C., Rettori, R., and Roghi, G. 1999, The Prati di Stuores/Stuores Wiesen Section (Dolomites, Italy): a candidate Global Stratotype Section and Point for the base of the Carnian stage. *Rivista Italiana di Paleontologia Stratigraphia*, 105, 37-78.

Butler, M. 1998. The geological history and the southern Wessex Basin- a review of new information from oil exploration. In: Underhill, J. R. (ed), *Development, evolution and petroleum geology of the Wessex Basin.* Geological Society London Special Publication 133, 67-86.

Cirilli, S., 2010. Upper Triassic–lowermost Jurassic palynology and palynostratigraphy: a review. *In:* Lucas, S.G. (ed) *The Triassic timescale, Geological Society, London, Special Publications*, 334, 285-314.

Clegg, J.A., Almond, M. and Stubbs, P.H.S. 1954. LXVI. The remanent magnetism of some sedimentary rocks in Britain. *The London, Edinburgh, and Dublin Philosophical Magazine and Journal of Science*, 45, 583-598.

Coram, R.A., Radley, J.D. and Benton, M.J. (Anisian) Otter Sandstone biota (Devon, UK): review, recent discoveries and ways ahead. *Proceedings of the Geologists' Association*, 130, 294-306.

Creer, K.M. 1959. AC demagnetization of unstable Triassic Keuper Marls from SW England. *Geophysical Journal of the Royal Astronomical Society*, 2, 261-275.

Creer, K.M. 1961. Superparamagnetism in red sandstones. *Geophysical Journal of the Royal Astronomical Society*, 5, 16-28.

Creer, K.M., Irving, E. and Runcorn, S.K. 1954. The direction of the geomagnetic field in remote epochs in Great Britain. *Journal of geomagnetism and geoelectricity*, 6, 163-168.

Dal Corso, J., Gianolla, P., Rigo, M., Franceschi, M., Roghi, G., Mietto, P., Manfrin, S., Raucsik, B., Budai, T., Jenkyns, H.C. and Reymond, C.E. 2018. Multiple negative carbon-isotope excursions during the Carnian Pluvial Episode (Late Triassic). *Earth-Science Reviews*, 185, 732-750.

Dal Corso, J., Bernardi, M., Sun, Y., Song, H., Seyfullah, L.J., Preto, N., Gianolla, P., Ruffell, A., Kustatscher, E., Roghi, G. and Merico, A. 2020. Extinction and dawn of the modern world in the Carnian (Late Triassic). *Science Advances*, 6, page numbers? DOI: 10.1126/sciadv.aba009

Feist-Burkhardt, S., Götz, A.E., Szulc, J., Borkhataria, R., Geluk, M., Haas, J., Hornung, J., Jordan, P., Kempf, O., Michalík, J. and Nawrocki, J. 2008. Triassic. *In:* McCann, T. (ed). *The Geology of Central Europe Volume 2: Mesozoic and Cenozoic*, Geological Society of London, 749-822. https://doi.org/10.1144/CEV2P.1

Franz, M., Henniger, M. and Barnasch, J. 2013. The strong diachronous Muschelkalk/Keuper facies shift in the Central European Basin: implications from the type-section of the Erfurt Formation (Lower Keuper, Triassic) and basin-wide correlations. International *Journal of Earth Sciences*, 102, 761-780.

Franz, M., Nowak, K., Berner, U., Heunisch, C., Bandel, K., Röhling, H.G. and Wolfgramm, M., 2014. Eustatic control on epicontinental basins: the example of the Stuttgart Formation in the Central European Basin (Middle Keuper, Late Triassic). *Global and Planetary Change*, 122, 305-329.

Franz, M., Kustatscher, E., Heunisch, C., Niegel, S. and Röhling, H.G. 2019. The Schilfsandstein and its flora; arguments for a humid mid-Carnian episode?. *Journal of the Geological Society*, 176, 133-148.

Furin, S., Preto, N., Rigo, M., Roghi, G., Gianolla, P., Crowley, J.L. and Bowring, S.A., 2006. High-precision U-Pb zircon age from the Triassic of Italy: Implications for the Triassic time scale and the Carnian origin of calcareous nannoplankton and dinosaurs. *Geology*, 34, 1009-1012.

Galbrun, B., Boulila, S., Krystyn, L., Richoz, S., Gardin, S., Bartolini, A. and Maslo, M., 2020. " Short" or "long" Rhaetian? Astronomical calibration of Austrian key sections. *Global and Planetary Change*, 192, doi.org/10.1016/j.gloplacha.2020.103253

Gallet, Y., Krystyn, L. and Besse, J. 1998. Upper Anisian and lower Carnian magnetostratigraphy from the northern Calcareous Alps (Austria), *Journal of Geophysical Research*, 103, 605-622.

Gallet, Y., Krystyn, L., Besse, J. and Marcoux, J. 2003. Improving the Upper Triassic numerical time scale from cross-correlation between Tethyan marine sections and the continental Newark basin sequence. *Earth and Planetary Science Letters*, 212, 255-261.

Gallet, Y., Krystyn, L., Marcoux, J. and Besse, J. 2007. New constraints on the end-Triassic (Upper Norian–Rhaetian) magnetostratigraphy. *Earth and Planetary Science Letters*, 255, 458-470.

Gallois, R.W. 2001. The lithostratigraphy of the Mercia Mudstone Group (mid and late Triassic) of the south Devon coast. *Geoscience in south-west England* , 10, 195-204.

Gallois, R.W. 2003. The distribution of halite (rock salt) in the Mercia Mudstone Group (mid to late Triassic) in south-west England. *Geoscience in south-west England*, 10, 383-389.

Gallois, R.W. 2005. The type section of the junction of the Otter Sandstone Formation and the Mercia Mudstone Group (mid Triassic) at Pennington Point, Sidmouth. *Geoscience in south-west England*, 11, 51-58.

Gallois, R.W. 2006. Correlation of the Triassic and Jurassic successions proved in the Lyme Regis (1901) borehole with those exposed on the nearby Devon and Dorset coasts. *Geoscience in south-west England*, 11, 99-105.

Gallois, R.W. 2007. The stratigraphy of the Mercia Mudstone Group succession (mid to late Triassic) proved in the Wiscombe Park boreholes, Devon. *Geoscience in south-west England*, 11, 280-286.

Gallois, R.W. 2019. The stratigraphy of the Permo-Triassic rocks of the Dorset and East Devon Coast World Heritage Site, UK. *Proceedings of the Geologists' Association*, 130, 274-293.

Gallois, R.W. and Porter, R.J. 2006. The stratigraphy and sedimentology of the Dunscombe Mudstone Formation (late Triassic) of south-west England. *Geoscience in south-west England*, 11, 174-182.

Geyer, G. and Kelber, K.P. 2018. Spinicaudata ("Conchostraca," Crustacea) from the Middle Keuper (Upper Triassic) of the southern Germanic Basin, with a review of Carnian–Norian taxa and suggested biozones. *PalZ*, 92, 1-34.

Hagdorn, H. and Nitsch, E. 2009. *Field guide to the 6th International Triassic Field Workshop (Pan-European Correlation of the Triassic): Triassic of Southwest Germany*, Institut für Geowissenschaften der Universität Tübingen,72p. http://www.stratigraphie.de/perm-trias/Triassic_workshop_2009_guide.pdf.

Haque, Z., Geissman, J.W., Irmis, R.B., Olsen, P.E., Lepre, C., Buhedma, H., Mundil, R., Parker, W.G., Rasmussen, C. and Gehrels, G.E. 2021. Magnetostratigraphy of the Triassic Moenkopi Formation from the continuous cores recovered in Colorado Plateau Coring Project Phase 1 (CPCP-1), Petrified Forest National Park, Arizona, USA: correlation of the Early to Middle Triassic strata and biota in Colorado Plateau and its environs. *Journal of Geophysical Research*, 126, doi.org/10.1029/2021JB021899.

Heckert, A.B. and Lucas, S.G. 2015. Triassic vertebrate paleontology in New Mexico. *In*: Lucas, S.G. and Sullivan, R.M. (eds*). Fossil vertebrates in New Mexico*. *New Mexico Museum of Natural History and Science Bulletin*, 68, 77-96.

Hounslow, M.W., 2006. PMagTools version 4.2- a tool for analysis of 2-D and 3-D directional data. http://dx.doi.org/10.13140/RG.2.2.19872.58880.

Hounslow, M.W. and McIntosh, G. 2003. Magnetostratigraphy of the Sherwood Sandstone Group (Lower and Middle Triassic), south Devon, UK: detailed correlation of the marine and non-marine Anisian. *Palaeogeography, Palaeoclimatology, Palaeoecology*, 193, 325-348.

Hounslow, M.W. and Muttoni, G., 2010. The geomagnetic polarity timescale for the Triassic: linkage to stage boundary definitions. *In*: Lucas, S.G. (ed) *The Triassic timescale*, Geological Society, London, Special Publications, 334, 61-102.

Hounslow, M.W., Posen, P.E. and Warrington, G., 2004. Magnetostratigraphy and biostratigraphy of the Upper Triassic and lowermost Jurassic succession, St. Audrie's Bay, UK. *Palaeogeography, Palaeoclimatology, Palaeoecology*, 213, 331-358.

Hounslow, M.W., Peters, C., Mørk, A., Weitschat, W. and Vigran, J.O. 2008a. Biomagnetostratigraphy of the Vikinghøgda Formation, Svalbard (Arctic Norway),

and the geomagnetic polarity timescale for the Lower Triassic. *Geological Society of America Bulletin*, 120, 1305-1325.

Hounslow, M.W., Hu, M., Mørk, A., Weitschat, W., Vigran, J.O., Karloukovski, V. and Orchard, M.J. 2008b. Intercalibration of Boreal and Tethyan time scales: the magnetobiostratigraphy of the Middle Triassic and the latest Early Triassic from Spitsbergen, Arctic Norway. *Polar Research*, 27, 469-490.

Hounslow, M.W., Domeier, M. and Biggin, A.J. 2018. Subduction flux modulates the geomagnetic polarity reversal rate. *Tectonophysics*, 742, 34-49.

Hounslow, M.W., Harris, S.E., Wójcik, K., Nawrocki, J., Woodcock, N.H., Ratcliffe, K.T. and Montgomery, P. 2021a. Geomagnetic polarity during the early Silurian: The first magnetostratigraphy of the Llandovery. *Palaeogeography, Palaeoclimatology, Palaeoecology*, 567, doi.org/10.1016/j.palaeo.2021.110245.

Hounslow, M.W. and Carnian-Norian boundary working group, 2021b. Albertiana Working Group Report: The case for the Global Stratotype Section and Point (GSSP) for the base of the Norian stage. *Albertiana*, 46, 25-57.

Hounslow, M.W., Harris, S., Karloukovski, V. and Mørk, A. 2022a. Geomagnetic polarity and carbon isotopic stratigraphic assessment of the late Carnian-earliest Norian in Svalbard: evidence for a major hiatus and improved Boreal to Tethyan correlation. *Norwegian Journal of Geology*, 102, https://njg.geologi.no/vol-101-200/details/30/2339-2339.html

Hounslow, M.W., Xuan, C. and Nilsson. A. 2022b. Chapter 5: Using the geomagnetic field for correlation and dating. *In:* Coe A.L. (ed). *Deciphering Earth's history: the practice of stratigraphy.* Geological Society of London, 81-99.

Howard, A., Warrington, G., Ambrose, K. and Rees, J. 2008. *A formational framework for the Mercia Mudstone Group (Triassic) of England and Wales*. British Geological Survey Research Report, RR/08/04.

Indahl, U.G., Næs, T. and Liland, K.H., 2018. A similarity index for comparing coupled matrices. *Journal of Chemometrics*, 32, doi.org/10.1002/cem.3049.

Irmis, R.B., Martz, J.W., Parker, W.G. and Nesbitt, S.J. 2010. Re-evaluating the correlation between Late Triassic terrestrial vertebrate biostratigraphy and the GSSP-defined marine stages. *Albertiana*, 38, pp.40-52.

Irmis, R.B., Mundil, R., Mancuso, A.C., Carrillo-Briceño, J.D., Ottone, E.G. and Marsicano, C.A. 2022. South American Triassic geochronology: Constraints and uncertainties for

the tempo of Gondwanan non-marine vertebrate evolution. *Journal of South American Earth Sciences*, 116, doi.org/10.1016/j.jsames.2022.103770.

Irving, E. and Runcorn, S.K. 1957. II. Analysis of the paleomagnetism of the Torridonian sandstone series of North-West Scotland. I. *Philosophical Transactions of the Royal Society of London. Series A, Mathematical and Physical Sciences*, 250, 83-99.

Jeans, C.V. 1978. The origin of the Triassic clay assemblages of Europe with special reference to the Keuper Marl and Rhaetic of parts of England. *Philosophical Transactions of the Royal Society of London*, Series A, 289, 549-639.

Jefferson, I., Rosenbaum, M., and Smalley, I. 2000. Mercia Mudstone as a Triassic aeolian desert sediment. *Mercian Geologist*, 15, 157–162.

Jin, X., McRoberts, C.A., Shi, Z., Mietto, P., Rigo, M., Roghi, G., Manfrin, S., Franceschi, M. and Preto, N. 2019. The aftermath of the CPE and the Carnian–Norian transition in northwestern Sichuan Basin, South China. *Journal of the Geological Society*, 176, 179-196.

Josse, J., Pagès, J. and Husson, F. 2008. Testing the significance of the RV coefficient. *Computational Statistics & Data Analysis*, 53, 82-91.

Kent, D.V. and Clemmensen, L.B. 2021. Northward dispersal of dinosaurs from Gondwana to Greenland at the mid-Norian (215–212 Ma, Late Triassic) dip in atmospheric pCO_2. *Proceedings of the National Academy of Sciences*, 118, doi.org/10.1073/pnas.2020778118.

Kent, D.V., Santi Malnis, P., Colombi, C.E., Alcober, O.A. and Martínez, R.N. 2014. Age constraints on the dispersal of dinosaurs in the Late Triassic from magnetochronology of the Los Colorados Formation (Argentina). *Proceedings of the National Academy of Sciences*, 111, 7958-7963.

Kent, D.V., Olsen, P.E. and Muttoni, G. 2017. Astrochronostratigraphic polarity time scale (APTS) for the Late Triassic and Early Jurassic from continental sediments and correlation with standard marine stages. *Earth-Science Reviews*, 166, 153-180.

Kent, J.T., Briden, J.C. and Mardia, K.V. 1983. Linear and planar structure in ordered mulivariate data as applied to progressive demagnetisation of palaeomagnetic remanance. *Geophysical Journal of the Royal Astronomical Society*, 81: 75-87.

Kemp, D.B. and Coe, A.L., 2007. A nonmarine record of eccentricity forcing through the Upper Triassic of southwest England and its correlation with the Newark Basin astronomically calibrated geomagnetic polarity time scale from North America. *Geology*, 35, 991-994.

Kozur, H.W. and Weems, R.E. 2010. The biostratigraphic importance of conchostracans in the continental Triassic of the northern hemisphere. *In*: Lucas, S.G. (ed) *The Triassic timescale, Geological Society, London, Special Publications*, 334, 315-417.

Krystyn, L., Richoz, S., Gallet, Y., Bouquerel, H., Kürschner, W.M. and Spötl, C. 2007. Updated bio-and magnetostratigraphy from Steinbergkogel (Austria), candidate GSSP for the base of the Rhaetian stage. *Albertiana*, 36, 164–173.

Krystyn, L., Mandl, G.W. and Schauer, M. 2009. Growth and termination of the upper Triassic platform margin of the Dachstein area (northers calcareous alps, Austria). *Austrian Journal of Earth Sciences*, 102, 23-33.

Kürschner, W.M. and Herngreen, G.W. 2010. Triassic palynology of central and northwestern Europe: a review of palynofloral diversity patterns and biostratigraphic subdivisions. *In*: Lucas, S.G. (ed) *The Triassic timescale, Geological Society, London, Special Publications*, 334, 263-283.

Lallier, F., Antoine, C., Charreau, J., Caumon, G. and Ruiu, J. 2013. Management of ambiguities in magnetostratigraphic correlation. *Earth and Planetary Science Letters*, 371, 26-36.

Lehrmann, D.J., Stepchinski, L., Altiner, D., Orchard, M.J., Montgomery, P., Enos, Ellwood, B.B., Bowring, S.A., Ramezani, J., Wang, H., Wei, J., Yu, M., Griffiths, J.D., Minzoni, M., Schaal, E.K., Li, X., Meyer, K.M. and Payne, J.L. 2015. An integrated biostratigraphy (conodonts and foraminifers) and chronostratigraphy (paleomagnetic reversals, magnetic susceptibility, elemental chemistry, carbon isotopes and geochronology) for the Permian–Upper Triassic strata of Guandao section, Nanpanjiang Basin, south China. *Journal of Asian Earth Sciences,* 108, 117–135.

Li, M., Huang, C., Hinnov, L., Chen, W., Ogg, J. and Tian, W. 2018. Astrochronology of the Anisian stage (Middle Triassic) at the Guandao reference section, South China. *Earth and Planetary Science Letters,* 482, 591-606.

Li, Q., Ruhl, M., Wang, Y.D., Xie, X.P., An, P.C. and Xu, Y.Y. 2022. Response of Carnian Pluvial Episode evidenced by organic carbon isotopic excursions from western Hubei, South China. *Palaeoworld*, 31, 324-333.

Li, Y., Shi, W., Aydin, A., Beroya-Eitner, M.A. and Gao, G. 2020. Loess genesis and worldwide distribution. *Earth-Science Reviews,* 201, doi.org/10.1016/j.earscirev.2019.102947

Lu, J., Zhang, P., Dal Corso, J., Yang, M., Wignall, P.B., Greene, S.E., Shao, L., Lyu, D. and Hilton, J. 2021. Volcanically driven lacustrine ecosystem changes during the Carnian Pluvial Episode (Late Triassic). *Proceedings of the National Academy of Sciences,* 118, doi.org/10.1073/pnas.2109895118.

Lucas, S.G., Tanner, L.H., Kozur, H.W., Weems, R.E. and Heckert, A.B. 2012. The Late Triassic timescale: age and correlation of the Carnian–Norian boundary. *Earth-Science Reviews,* 114, 1-18.

Lucas, S.G. and Schoch, R.R., 2002. Triassic temnospondyl biostratigraphy, biochronology and correlation of the German Buntsandstein and North American Moenkopi Formation. Lethaia, 35, 97-106.

Man, O., 2008. On the identification of magnetostratigraphic polarity zones. Studia *Geophysica et Geodaetica*, 52, 173-186.

Mao, X., Liu, X. and Zhou, X. 2021. Permo-Triassic aeolian red clay of southwestern England and its palaeoenvironmental implications. *Aeolian Research*, 52, doi.org/10.1016/j.aeolia.2021.100726

Maron, M., Muttoni, G., Rigo, M., Gianolla, P. and Kent, D.V. 2019. New magnetobiostratigraphic results from the Ladinian of the Dolomites and implications for the Triassic geomagnetic polarity timescale. *Palaeogeography, Palaeoclimatology, Palaeoecology*, 517, 52-73.

Martz, J.W. and Parker, W.G., 2017. Revised formulation of the Late Triassic Land Vertebrate "Faunachrons" of western North America: recommendations for codifying nascent systems of vertebrate biochronology. In: Ziegler, K.E and Parker, W.G. (eds). *Terrestrial depositional systems*, 39-125, Elsevier. doi.org/10.1016/B978-0-12-803243-5.00006-6). Elsevier.

Mazaheri-Johari, M., Gianolla, P., Mather, T.A., Frieling, J., Chu, D. and Dal Corso, J. 2021. Mercury deposition in Western Tethys during the Carnian Pluvial Episode (Late Triassic). *Scientific reports*, 11, 1-10.

McKie, T. 2014. Climatic and tectonic controls on Triassic dryland terminal fluvial system architecture, central North Sea. *In:* Martinius, A.W., Ravnås, R., Howell, J.A., Steel, R.J. and Wonham, J.P. (eds*) From depositional systems to sedimentary successions on the Norwegian continental margin. International Association of Sedimentologists. Special Publication* 46, 19–58.

McKie, T., 2017. Paleogeographic evolution of latest Permian and Triassic salt basins in Northwest Europe. *In*: Cámara, P., Flinch, J.F., Soto, J.I., Flinch, J.I. and Tari, G.

(eds). *Permo-Triassic Salt Provinces of Europe, North Africa and the Atlantic Margins*, Elsevier, 159-173.

Meyers, S.R. 2019. Cyclostratigraphy and the problem of astrochronologic testing. *Earth-Science Reviews*, 190, 190-223.

Middleton, N.J. 2017. Desert dust hazards: A global review. *Aeolian research*, 24, 53-63.

Mietto, P., Manfrin, S., Preto, N., Rigo, M., Roghi, G., Furin, S., Gianolla, P., Posenato, R., Muttoni, G., Nicora, A. and Buratti, N. 2012. The global boundary stratotype section and point (GSSP) of the Carnian stage (Late Triassic) at Prati di Stuores/Stuores Wiesen section (Southern Alps, NE Italy). *Episodes*, 35, 414-430.

Miller, C.S., Peterse, F., Da Silva, A.C., Baranyi, V., Reichart, G.J. and Kürschner, W.M., 2017. Astronomical age constraints and extinction mechanisms of the Late Triassic Carnian crisis. *Scientific Reports*, 7, 1-7.

Milner, A.R., Gardiner, B.G., Fraser, N.C. and Taylor, M.A. 1990. Vertebrates from the Middle Triassic Otter Sandstone Formation of Devon. *Palaeontology*, 33, 873-892.

Milroy, P., Wright, V.P. and Simms, M.J. 2019. Dryland continental mudstones: Deciphering environmental changes in problematic mudstones from the Upper Triassic (Carnian to Norian) Mercia Mudstone Group, south-west Britain. *Sedimentology*, 66, 2557-2589.

Morton, A., Hounslow, M.W. and Frei, D. 2013. Heavy-mineral, mineral-chemical and zircon-age constraints on the provenance of Triassic sandstones from the Devon coast, southern Britain. *Geologos*, 19, 67–85. doi: 10.2478/logos-2013-0005.

Mueller, S., Hounslow, M.W. and Kürschner, W.M. 2016. Integrated stratigraphy and palaeoclimate history of the Carnian Pluvial Event in the Boreal realm; new data from the Upper Triassic Kapp Toscana Group in central Spitsbergen (Norway). *Journal of the Geological Society*, 173, 186-202.

Muttoni, G., Kent, D.V., Olsen, P.E., Stefano, P.D., Lowrie, W., Bernasconi, S.M. and Hernández, F.M. 2004. Tethyan magnetostratigraphy from Pizzo Mondello (Sicily) and correlation to the Late Triassic Newark astrochronological polarity time scale. *Geological Society of America Bulletin*, 116, 1043-1058.

Nawrocki, J. and Szulc, J. 2000. The Middle Triassic magnetostratigraphy from the Peri-Tethys basin in Poland. *Earth and Planetary Science Letters*, 182, 77-92.

Nawrocki, J., Jewuła, K., Stachowska, A. and Szulc, J. 2015. Magnetic polarity of Upper Triassic sediments of the Germanic Basin in Poland. *Annales Societatis Geologorum Poloniae*, 85, 663-674, doi: 10.14241/asgp.2015.026

Newell, A.J. 2018a. Evolving stratigraphy of a Middle Triassic fluvial-dominated sheet sandstone: The Otter Sandstone Formation of the Wessex Basin (UK). *Geological Journal*, 53, 1954-1972.

Newell, A.J. 2018b. Rifts, rivers and climate recovery: A new model for the Triassic of England. *Proceedings of the Geologists' Association*, 129, 352-371.

Nitsch, E., Beutler, G., Hauschke, N., Etzold, A. and Laass, M. 2005. Feinstratigraphische Korrelation der Grabfeld-Formation (Keuper, Trias) zwischen Hochrhein und Ostsee. *Hallesches Jahrbuch für Geowissenschaften, Reihe B: Geologie, Paläontologie, Mineralogie*, 19, 137-152.

Ogg, J.G., Chen, Z.Q., Orchard, M.J. and Jiang, H.S. 2020. The Triassic Period. *In:* Gradstein, F.M., Ogg, J.G., Schmitz, M.D. and Ogg, G.M. (eds), *Geologic Time Scale 2020*, Elsevier, 903-953. DOI: https://doi.org/10.1016/B978-0-12-824360-2.00025-5.

Olson, P., Hinnov, L.A. and Driscoll, P.E., 2014. Nonrandom geomagnetic reversal times and geodynamo evolution. *Earth and Planetary Science Letters*, 388, 9-17.

Paul, J., Wemmer, K. and Ahrendt, H. 2008. Provenance of siliciclastic sediments (Permian to Jurassic) in the Central European Basin. *Zeitschrift der Deutschen Gesellschaft fur Geowissenschaften*, **159**, 641-650

Porter, R.J. and Gallois, R.W. 2008. Identifying fluvio–lacustrine intervals in thick playa-lake successions: An integrated sedimentology and ichnology of arenaceous members in the mid–late Triassic Mercia Mudstone Group of south-west England, UK. *Palaeogeography, Palaeoclimatology, Palaeoecology*, 270, 381-398.

Rayfield, E.J., Barrett, P.M. and Milner, A.R., 2009. Utility and validity of Middle and Late Triassic 'land vertebrate faunachrons'. *Journal of Vertebrate Paleontology*, 29, 80-87.

Reinhardt, L. and Ricken, W. 2000. The stratigraphic and geochemical record of Playa Cycles: monitoring a Pangaean monsoon-like system (Triassic, Middle Keuper, S. Germany). *Palaeogeography, Palaeoclimatology, Palaeoecology*, 161, 205-227.

Rigo, M., Bertinelli, A., Concheri, G., Gattolin, G., Godfrey, L., Katz, M.E., Maron, M., Mietto, P., Muttoni, G., Sprovieri, M. and Stellin, F., 2016. The Pignola-Abriola section (southern Apennines, Italy): a new GSSP candidate for the base of the Rhaetian Stage. *Lethaia*, 49, 287-306.

Rigo, M., Mazza, M., Karádi, V. and Nicora, A., 2018. New Upper Triassic conodont biozonation of the Tethyan realm. *In*: Tanner, L. (eds) *The Late Triassic World*. Springer, Cham, 189-235. doi.org/10.1007/978-3-319-68009-5_6

Ruffell, A., Simms, M.J. and Wignall, P.B. 2016. The Carnian humid episode of the Late Triassic: a review. *Geological Magazine*, 153, 271-284.

Seyfullah, L.J., Kustatscher, E. and Taylor, W.A. 2013. The first discovery of in situ *Verrucosisporites applanatus* spores from the Middle Triassic flora from Bromsgrove (Worcestershire, UK). *Review of Palaeobotany and Palynology*, 197, 15-25.

Song, H., Wignall, P.B. and Dunhill, A.M. 2018. Decoupled taxonomic and ecological recoveries from the Permo-Triassic extinction. *Science advances*, 4, doi.org/ 10.1126/sciadv.aat509.

Spencer, P.S. and Storrs, G.W. 2002. A re-evaluation of small tetrapods from the Middle Triassic Otter Sandstone Formation of Devon, England. *Palaeontology*, 45, 447-467.

Stockar, R., Baumgartner, P.O. and Condon, D. 2012. Integrated Ladinian bio-chronostratigraphy and geochrononology of Monte San Giorgio (Southern Alps, Switzerland). *Swiss Journal of Geosciences,* 105, 85-108.

Sun, Y.D., Orchard, M.J., Kocsis, Á.T. and Joachimski, M.M. 2020. Carnian–Norian (Late Triassic) climate change: Evidence from conodont oxygen isotope thermometry with implications for reef development and Wrangellian tectonics. *Earth and Planetary Science Letters,* 534, doi.org/10.1016/j.epsl.2020.116082.

Swanson-Hysell, N.L., Fairchild, L.M. and Slotznick, S.P. 2019. Primary and secondary red bed magnetization constrained by fluvial intraclasts. *Journal of Geophysical Research, Solid Earth*, 124, 4276-4289.

Szurlies, M. 2007. Latest Permian to Middle Triassic cyclo-magnetostratigraphy from the Central European Basin, Germany: Implications for the geomagnetic polarity timescale. *Earth and Planetary Science Letters,* 261, 602-619.

Tanner, L.H. and Lucas, S.G. 2015. The Triassic-Jurassic strata of the Newark Basin, USA: a complete and accurate astronomically-tuned timescale. *Stratigraphy*, 12, 47-65.

Talbot, M., Holm, K. and Williams, M. 1994. Sedimentation in low-gradient desert margin systems: A comparison of the Late Triassic of northwest Somerset. In: Rosen, M.R. (ed). *Paleoclimate and basin evolution of playa systems, Geological Society of America special paper*, 289, 97-118.

Vollmer, T., Werner, R., Weber, M., Tougiannidis, N., Röhling, H.G. and Hambach, U. 2008. Orbital control on Upper Triassic Playa cycles of the Steinmergel-Keuper (Norian): A new concept for ancient playa cycles. *Palaeogeography, Palaeoclimatology, Palaeoecology,* 267, 1-16.

Wang, M., Li, M., Kemp, D.B., Boulila, S. and Ogg, J.G. 2022. Sedimentary noise modeling of lake-level change in the Late Triassic Newark Basin of North America. *Global and Planetary Change*, 208, page numbers. doi.org/10.1016/j.gloplacha.2021.103706.

Warrington, G. H., 1971. Palynology of the New Red Sandstone of the South Devon coast. *Proceedings of the Ussher Society* 2, 307-314.

Warrington, G. H. 1997. The Lyme Regis Borehole, Dorset-palynology of the Mercia Mudstone, Penarth and Lias groups (Upper Triassic-Lower Jurassic). *Proceedings of the Ussher Society*, 9, 153-157.

Warrington, G. 2005. The chronology of the Permian and Triassic of Devon and south-east Cornwall (U.K.): a review of methods and results. *Geoscience in south-west England*, 11, 117-122.

Withjack, M.O., Schlische, R.W., Malinconico, M.L. and Olsen, P.E. 2013. Rift-basin development: lessons from the Triassic–Jurassic Newark Basin of eastern North America. *In*: W. U. Mohriak, A. Danforth, P. J. Post, D. E. Brown, G. C. Tari, M. Nemčok, S. T. Sinha (eds.). *Conjugate Divergent Margins. Geological Society, London, Special Publications*, 369, 301-321.

Wójcik, K., Kołbuk, D., Sobień, K., Rosowiecka, O., Roszkowska-Remin, J., Nawrocki, J. and Szymkowiak, A. 2017. Keuper magnetostratigraphy in the southern Mesozoic margin of the Holy Cross Mts. (southeastern edge of the German Basin). *Geological Quarterly*, 61, 946-961.

Zeigler, K.E. and Geissman, J.W. 2011. Magnetostratigraphy of the Upper Triassic Chinle Group of New Mexico: Implications for regional and global correlations among Upper Triassic sequences. *Geosphere*, 7, 802-829.

Zhang, Y., Ogg, J.G., Franz, M., Bachmann, G.H., Szurlies, M., Röhling, H.G., Li, M., Rolf, C. and Obst, K. 2020. Carnian (Late Triassic) magnetostratigraphy from the Germanic Basin allowing global correlation of the Mid-Carnian Episode. *Earth and Planetary Science Letters*, 541, doi.org/10.1016/j.epsl.2020.116275.

Zhang, Z.T., Sun, Y.D., Lai, X.L., Joachimski, M.M. and Wignall, P.B., 2017. Early Carnian conodont fauna at Yongyue, Zhenfeng area and its implication for Ladinian-Carnian subdivision in Guizhou, South China. *Palaeogeography, Palaeoclimatology, Palaeoecology*, 486, 142-157.

Figure Captions

Fig. 1. Geological sketch sections of the Mercia Mudstone Group outcrop in the cliffs between Sidmouth in the west and Bindon Cliffs (east of Seaton). All sections projected onto a west-east line. Drift deposits and minor landslides omitted for clarity. Inset shows location in UK.

Fig. 2. Summary of the magnetostratigraphic data for the Sidmouth to Salcombe Mouth section. A) simplified sedimentary log (see SI Fig. S1.1 for detailed log) and magnetic susceptibility (MS) and initial natural remanent magnetisation (NRM) intensity (each point represents a demagnetised specimen). B) Demagnetisation behaviour classification of specimen data. C) Specimen polarity classification. D) Virtual geomagnetic pole latitude (VGP_R) with respect to the formation mean pole, with S-class data with filled symbol and T-class data with unfilled symbol; E) interpreted polarity and section lithostratigraphy. MZ=labels of magnetozone couplets (BS8r is a continuation of that used by Hounslow and McIntosh (2003) for the Budleigh Salterton to Sidmouth Section); SS=Sidmouth to Seaton sections.

Fig. 3. Summary magnetostratigraphic data for the Salcombe Mouth to Hook Ebb section. See Fig. 2 for column details. See SI Fig. S1.2 for detailed log.

Fig. 4. Summary magnetostratigraphic data for the Strangman's Cove section. See Fig. 2 for column details. The position of the organic matter carbon isotope excursions of Miller et al. (2017) and Baranyi et al. (2019) are shown as (C). See SI Fig. S1.3 for detailed log.

Fig. 5. Summary magnetostratigraphic data for the Littlecombe Shoot sections. Upper panels are the western section, and lower panels the eastern section. See Fig. 2 for column details. See SI Fig. S1.4 for detailed log. DMF=Dunscombe Mudstone Fm.

Fig. 6. Summary magnetostratigraphic data for the Red Rock to Branscombe Mouth section. See Fig. 2 for column details. See SI Figs S1.4 and S1.5 for detailed logs.

Fig. 7. Summary magnetostratigraphic data for the Seaton Cliff section. See Fig. 2 for column details. See SI Fig.S1.6 for detailed log.

Fig. 8. Summary magnetostratigraphic data for the Haven Cliff section. See Fig. 2 for column details. See SI Fig. S1.7 for detailed log.

Fig. 9. Specimen S-class ChRM directions for the sections. A) Sidmouth Mudstone Fm and Pennington Point Member from the Sid outfall to Hook Ebb sections. B) The Strangman's Cove section, largely in the Dunscombe Mudstone Formation; C) The

Littlecombe Shoot sections in the Littlecombe Shoot Mudstone Member. D) The Red Rock Gypsum and Seaton Mudstone Members in the Branscombe Mouth and Seaton Cliffs sections; E) Haven Cliff section. See SI Table S3.1 for mean directions and other directional tests.

Fig. 10. Magnetic polarity correlations for the interval from the middle part of the Otter Sandstone Fm and lower part of the Sidmouth Mudstone Fm. GPTS-A from Maron et al. (2019), Ogg et al. (2020) and GPTS-B from Hounslow and Muttoni (2010). Otter Sandstone data from Hounslow and McIntosh (2003), with lithostratigraphy of Newell (2018a) and Gallois (2001). PPM= Pennington Point Member. See text for description of option-1 and option-2 correlations. Details of the statistical comparisons are in the SI.

Fig. 11. Correlation of the upper part of the Sidmouth Mudstone Fm to the Erfurt to Grabfeld formations of the Central European Basin (Morsleben polarity from Zhang et al. 2020). Likely correlation to the GPTS composites of Hounslow and Muttoni (2010) and Maron et al. (2019) are indicated. The differences between the two GTPS are related to the differences in correlation between the marine Stoures and Mayerling sections. GPTS-B uses that proposed by Broglio Loriga et al. (1999), GPTS-A use the first occurrence of the conodont *Paragondolella polygnathiformis* (Mietto et al. 2012; a single specimen at Stuores). The base of Julian-2 (J2) in GPTS-A is based on conodonts in Zhang et al. (2017), and in GPTS-B conodonts of Gallet et al. (1998).

Fig. 12. Comparison of the magnetostratigraphy of the Carnian-age interval of the MMG with the GPTS-A of Ogg et al. (2020) and GPTS-B of Hounslow et al. (2022a). The correlation of the Morsleben core data to the GPTS-A is that of Zhang et al. (2020). Position of negative carbon isotope excursions (C) shown are based on Fig. 5 for the MMG excursions (labelled DIE# on MMG column), Hounslow et al. (2022a) for the Tuvalian-Lacian excursions (CIE, T1 to T6 & L1), and Dal Corso et al. (2018) and Mueller et al. (2016) for the Julian excursions (J1- J4 on GPTS-A).

Fig. 13. Comparison of the Dunscombe Mudstone Fm (DMF) to the cycles and magnetostratigraphy of the Morsleben cores. Bed labels on DMF from Gallois and Porter (2006). Cycles in Morsleben 52a from Barnasch (2010), and lithostratigraphy from Franz et al. (2014). Red arrows are possible sequence stratigraphic correlations. Seq.= sequence stratigraphy outlined in SI Table S1.2.

Fig. 14. Summary data for composite magnetostratigraphy through the Norian and early Rhaetian, modified from Hounslow and Muttoni (2010) (see SI section 5 for source

details). See SI Fig. S5.3, S5.4 and SI section 5.1 for details of the upper Chinle Formation composite and detrital zircon ages. Newark Supergroup magnetostratigraphy from Kent et al. (2017), with astronomically anchored ages from their table 3. Red arrowed bar is the estimated stratigraphic uncertainty range in placing the radiometric date of Furin et al. (2006) onto the magnetostratigraphy. *E. quadrata* (*E. abneptis* A) and *E. slovakensis* (*E. n. sp*. D) conodont biozones are from Krystyn et al. (2009), others from Rigo et al. (2018). Fleming Fjord and La Sal section data from Kent and Clemmenson (2021) and Kent et al. (2014) respectively. Radioisotopic dates below La Sal section described in Irmis et al. (2022).

Fig. 15. Correlation of the magnetostratigraphy of the Norian-Rhaetian part of the MMG to the GPTS-B from Fig. 14. The likely missing interval in the Newark Supergroup in the middle of the E14 magnetozone is explained in the text. NRB1 and NRB2 are the positions proposed for the base of the Rhaetian of Krystyn et al. (2007) and Rigo et al. (2016) respectively. Magnetostratigraphic composite for upper Chinle Fm from SI Fig. S5.4. St Audrie's Bay data from Hounslow et al. (2004).

Fig. 16. The accumulation rates for the Otter Sandstone Fm and the Mercia Mudstone Group, using three age models. Symbols represent 'instantaneous' accumulation rates using the magnetochron durations, and the lines are geometric means of three adjacent instantaneous accumulation rates. Abbreviations: -M= Member, -MM= Mudstone Member, PP= Pennington Point, SH=Salcombe Hill; SM=Salcombe Mouth; HE=Hook Ebb; LW=Little Weston, LS=Littlecombe Shoot; RRG=Red Rock Gypsum; S= Seaton, HC=Haven Cliff; BAF=Blue Anchor.

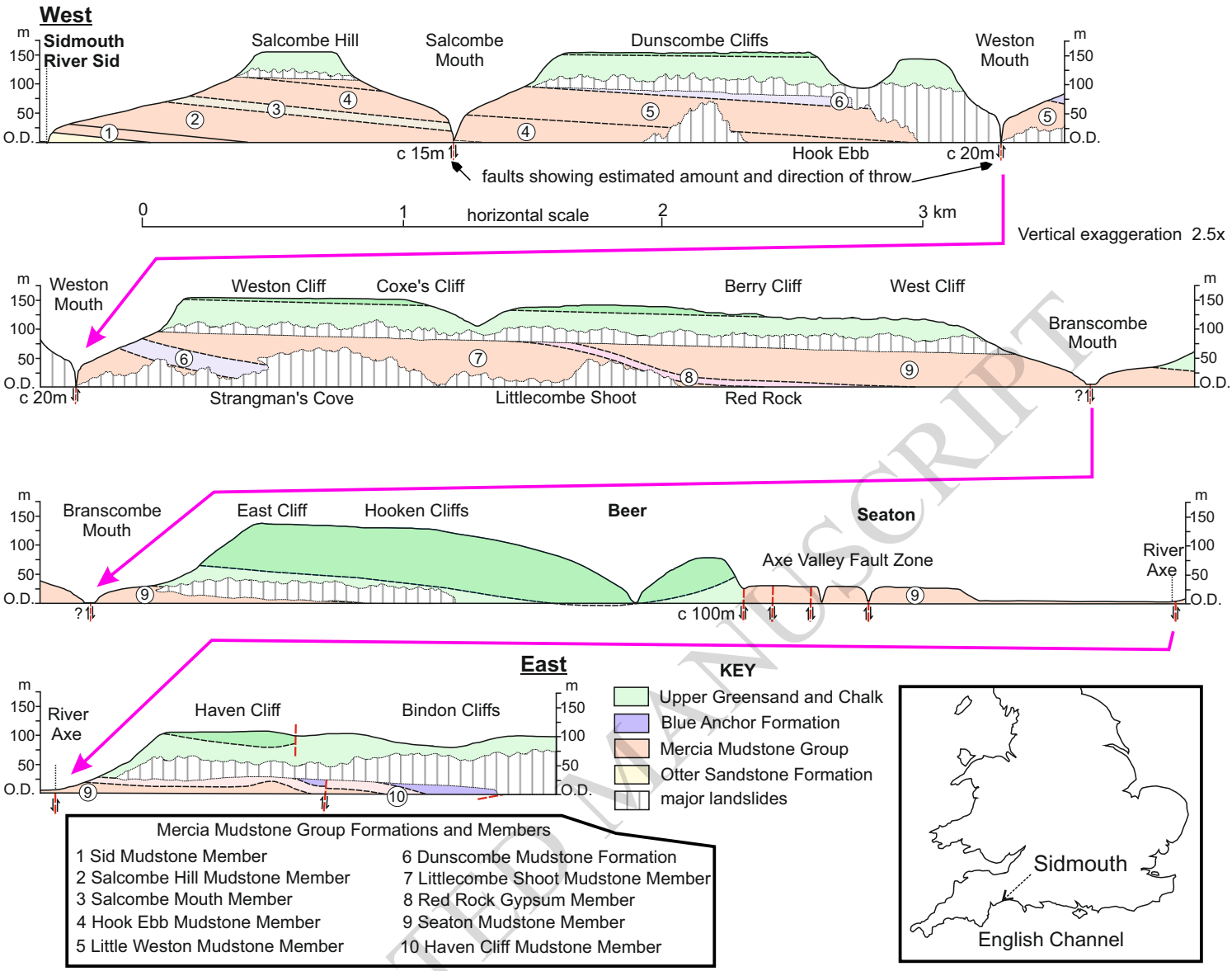

Fig. 1

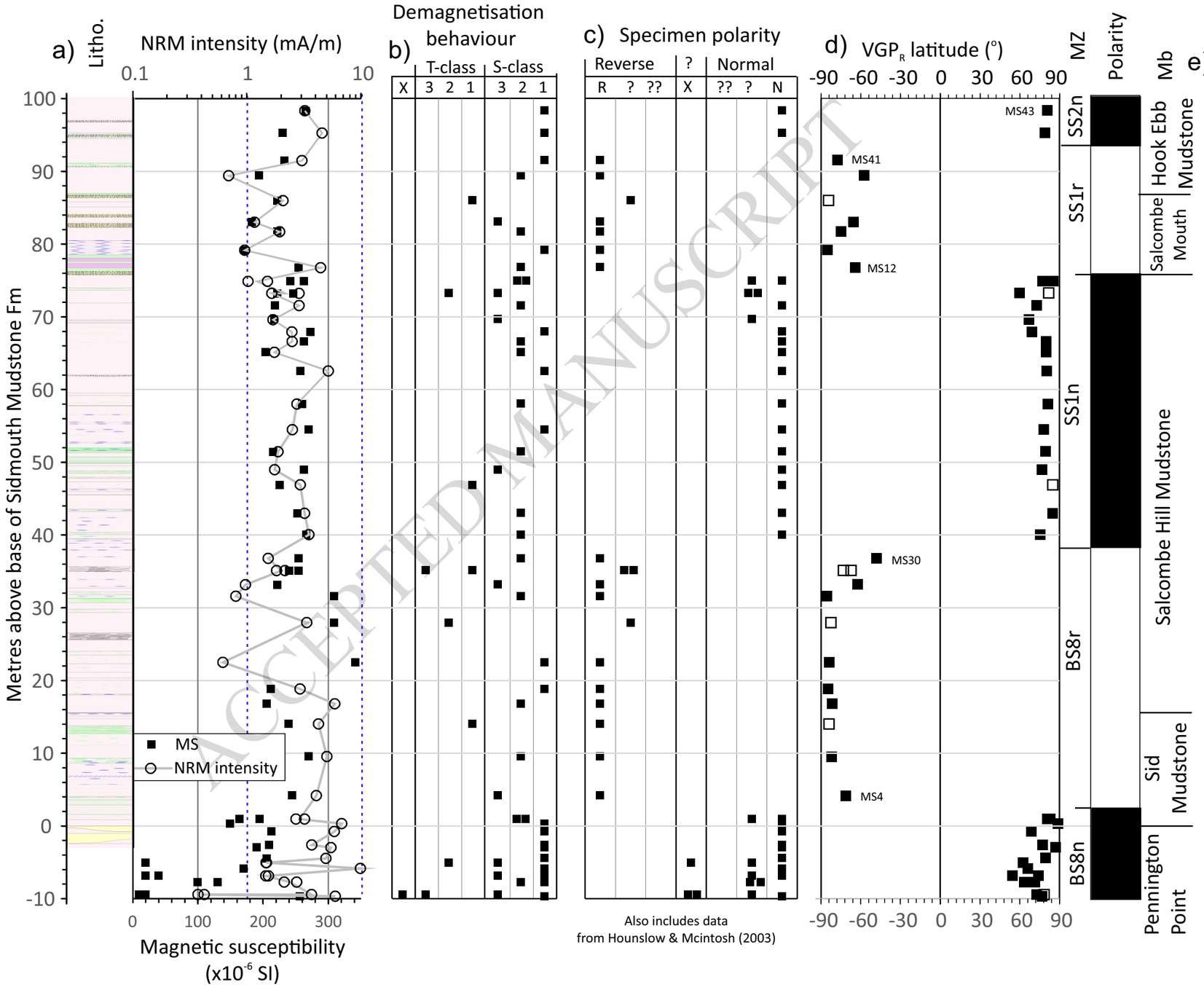

Fig. 2

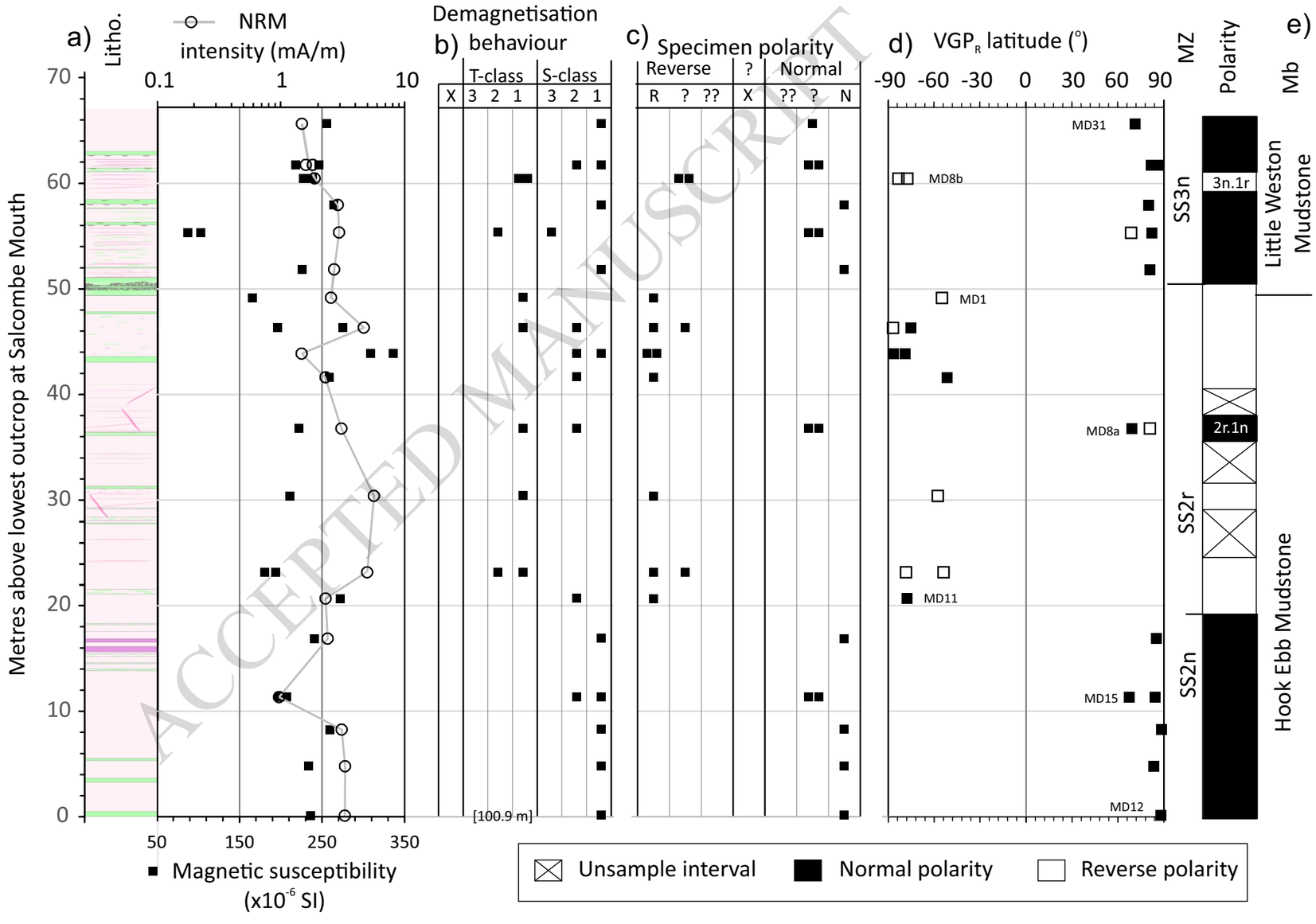

Fig. 3

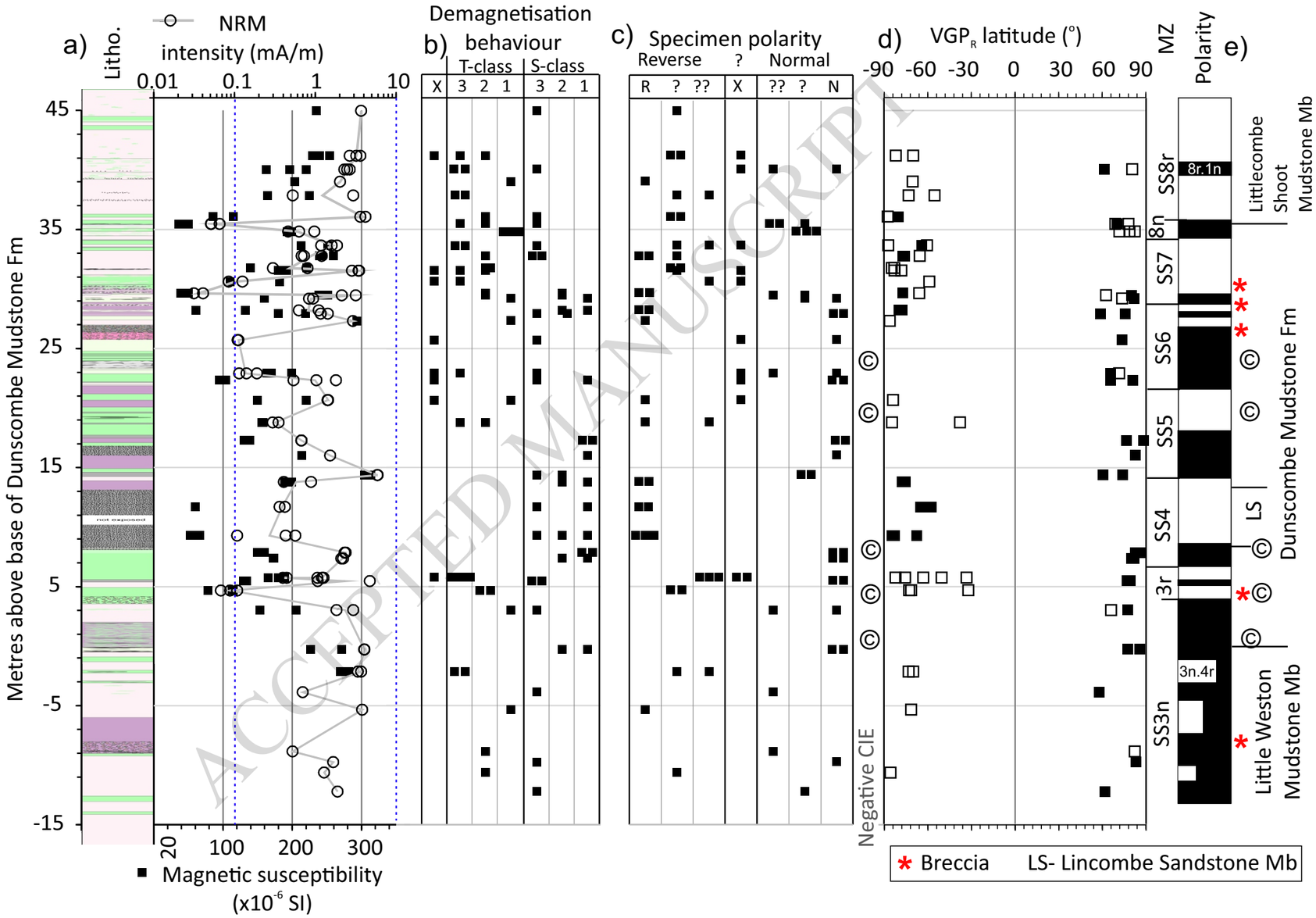

Fig. 4

Fig. 5

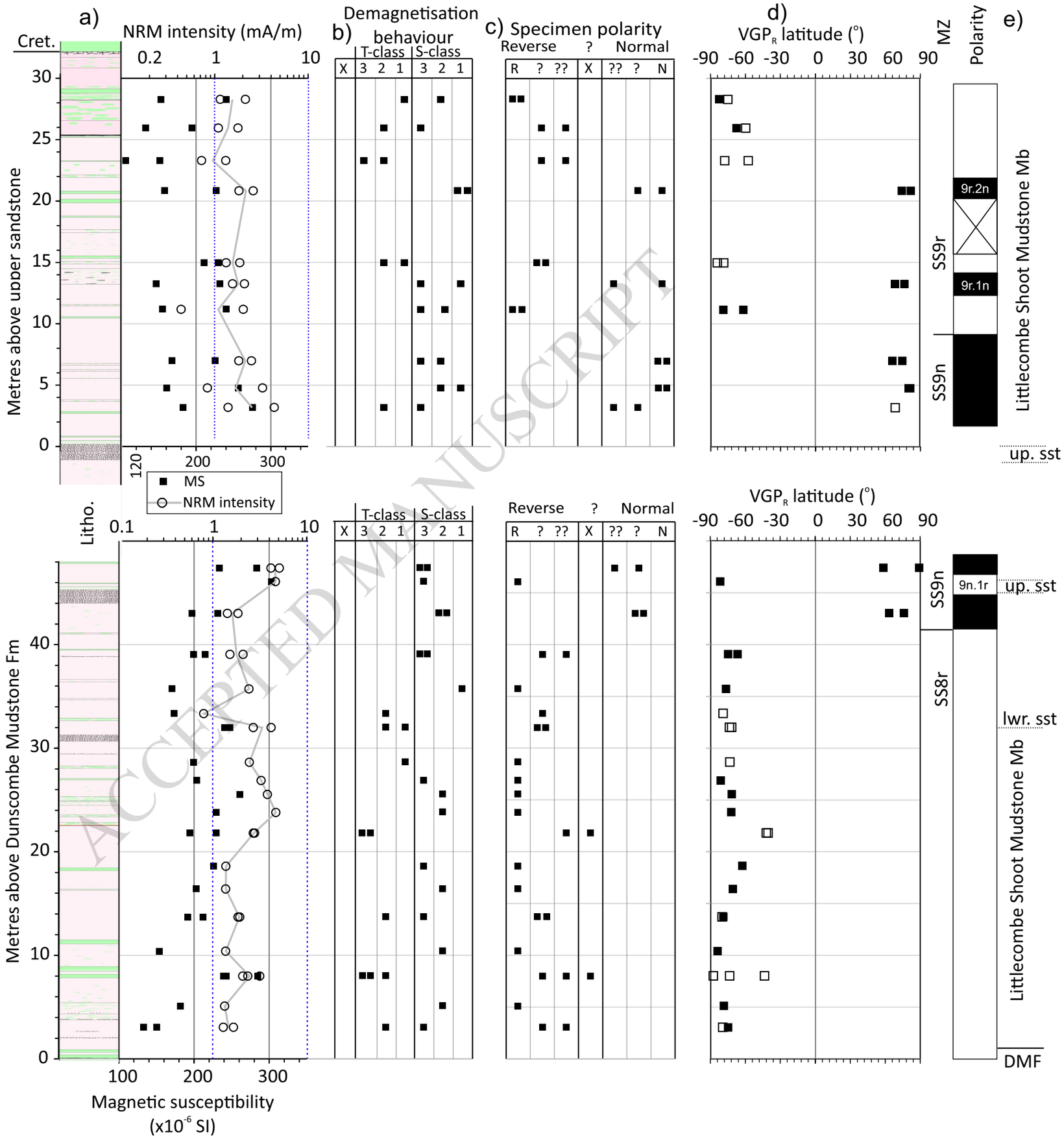

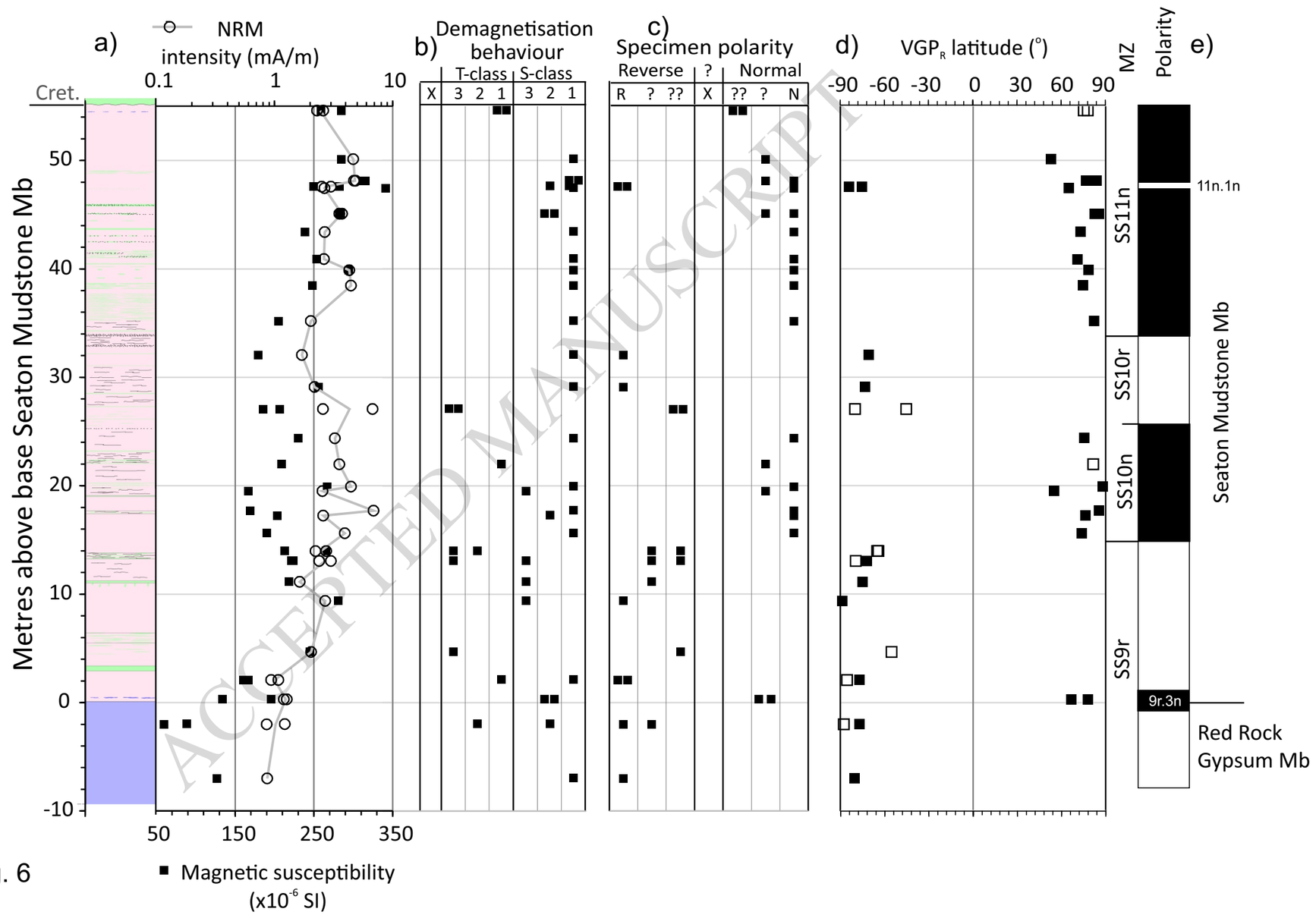

Fig. 6

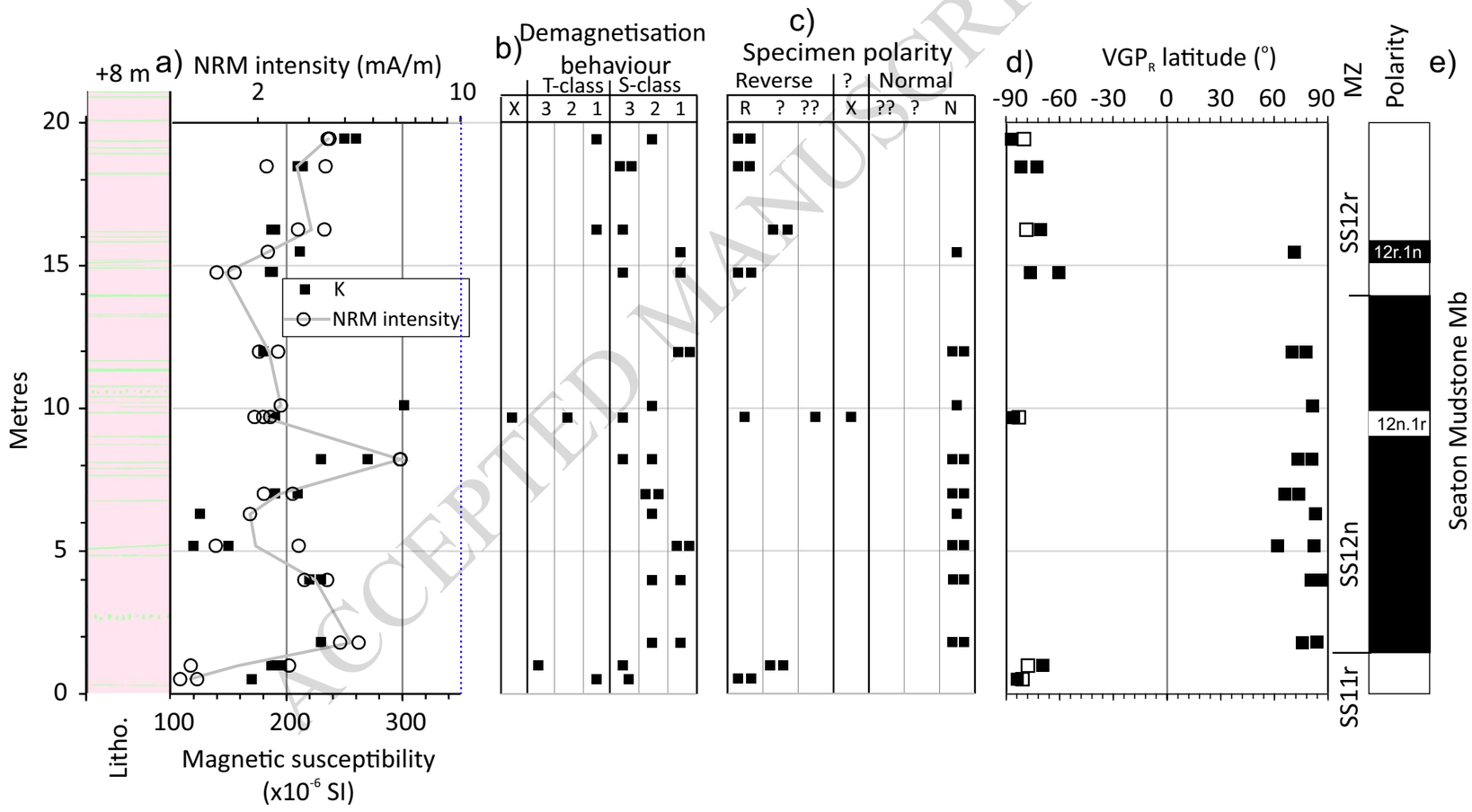

Fig. 7

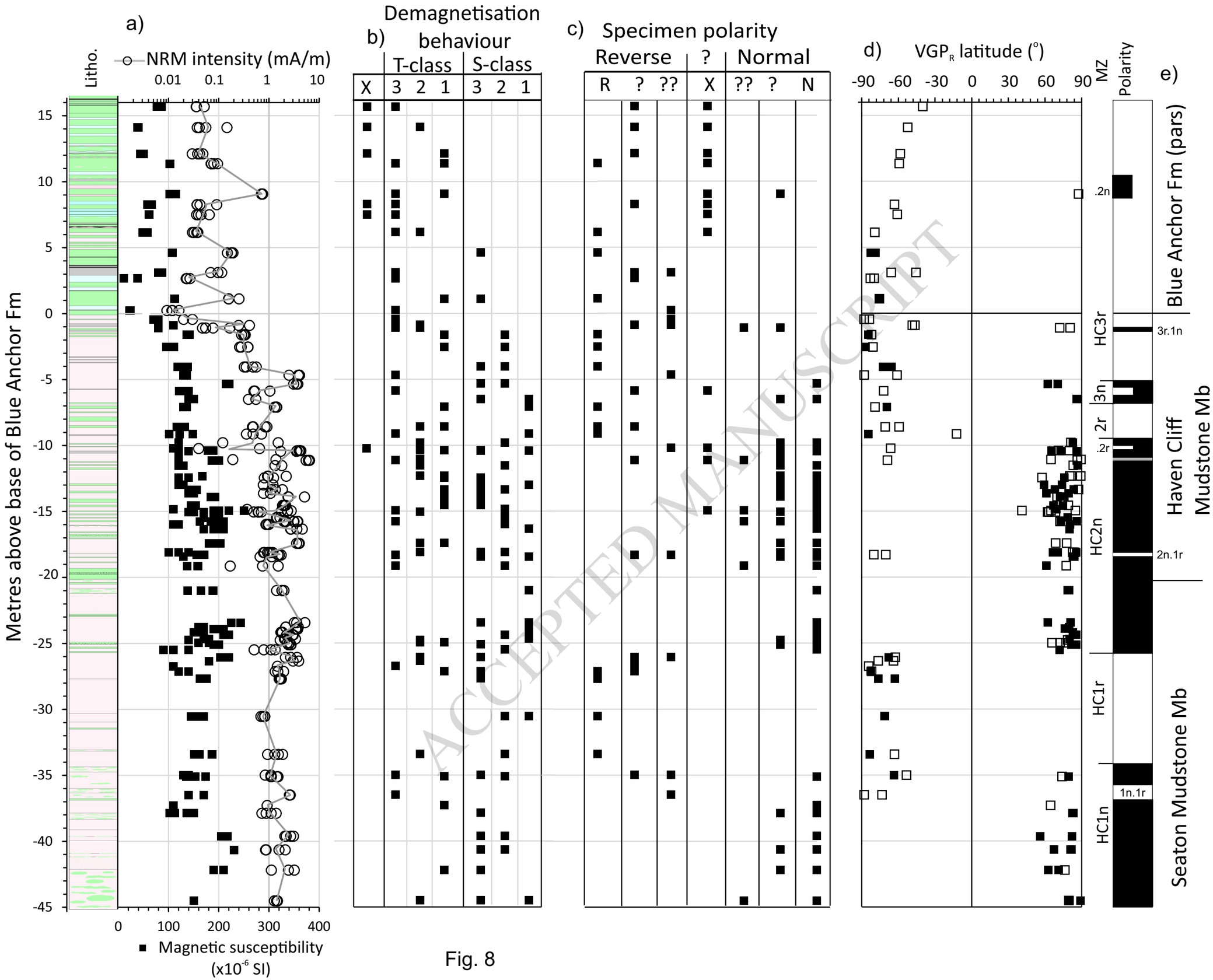

Fig. 8

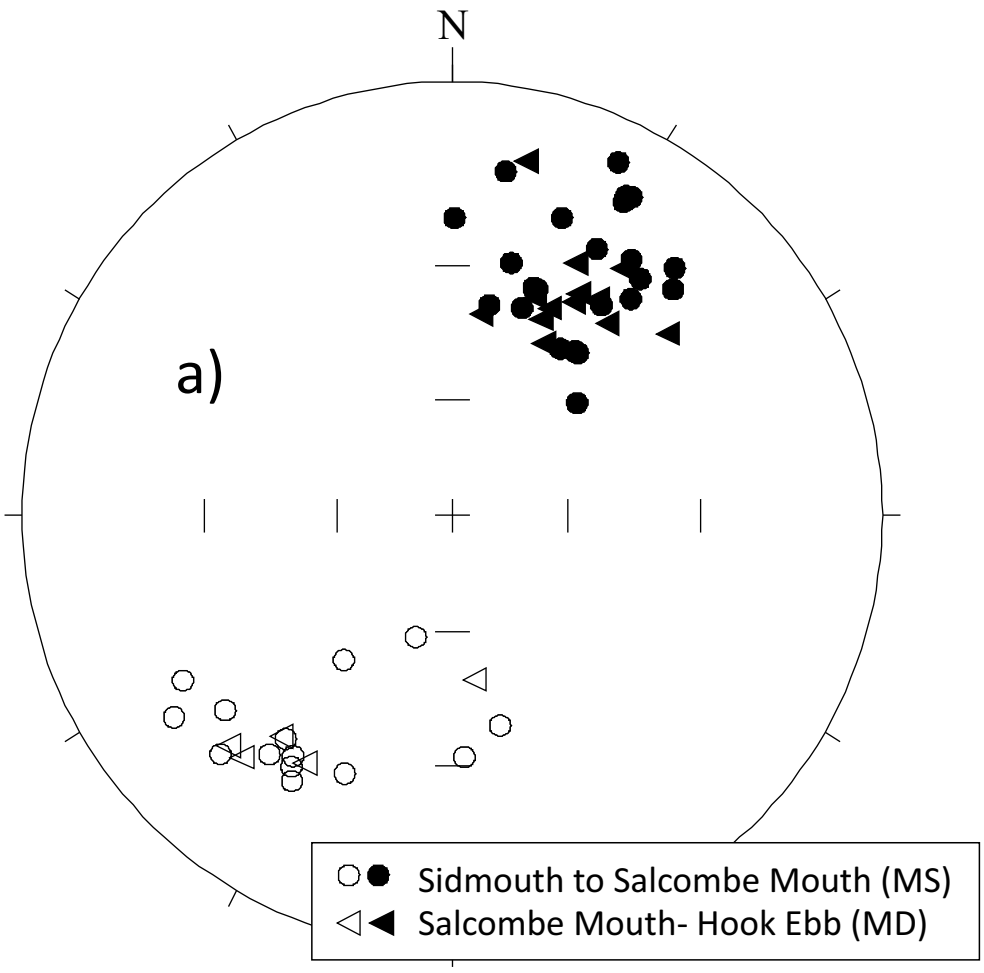

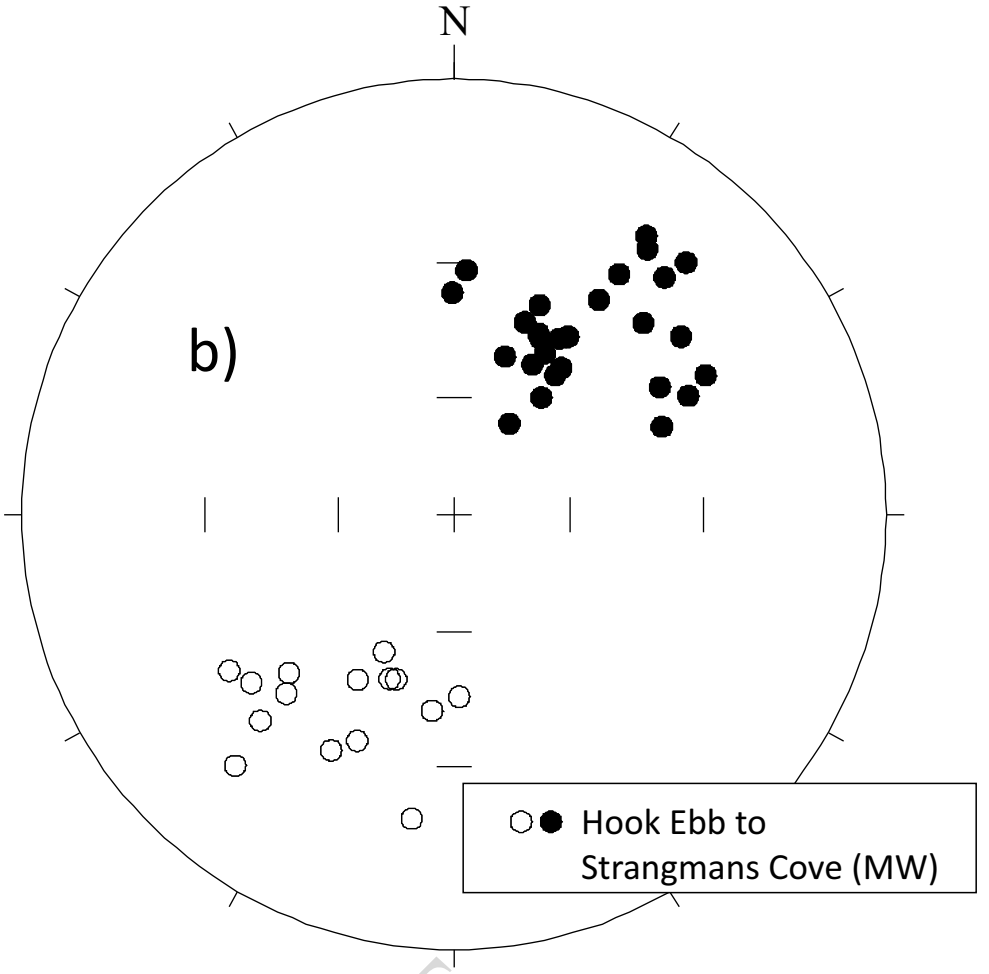

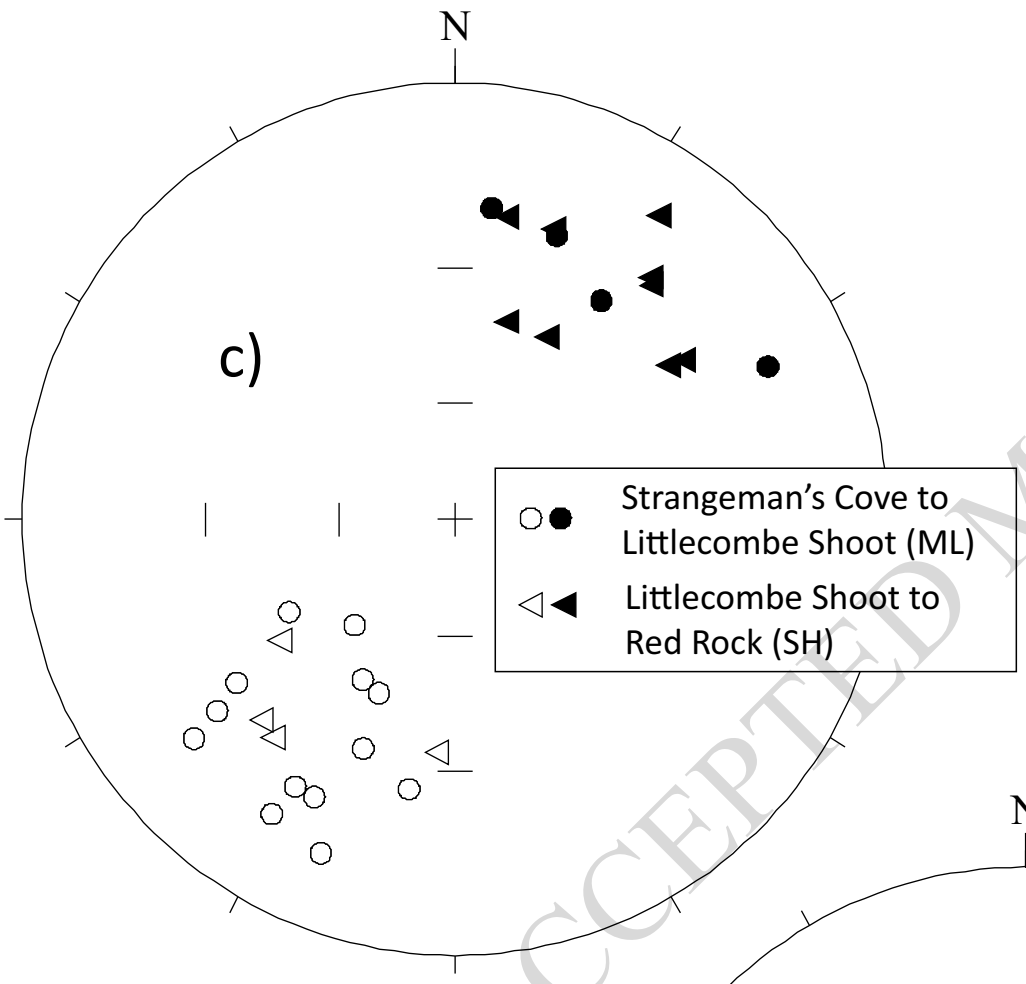

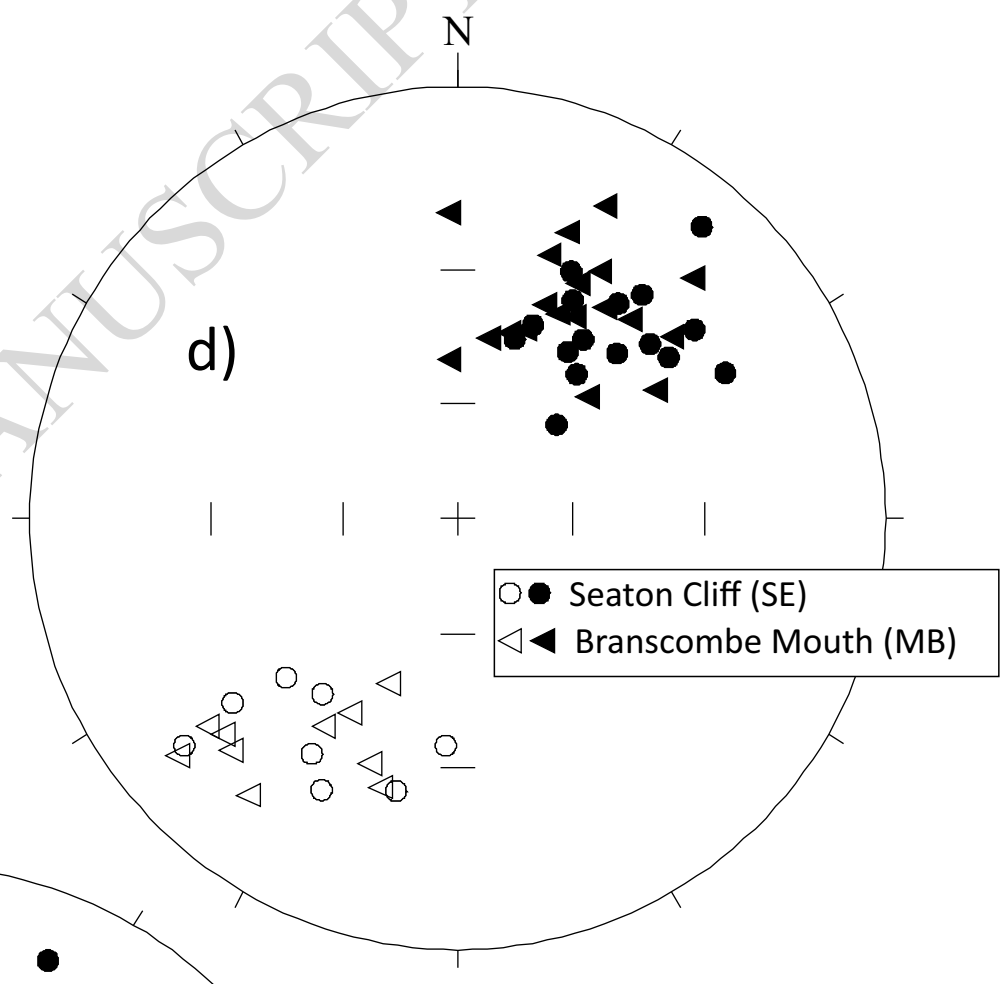

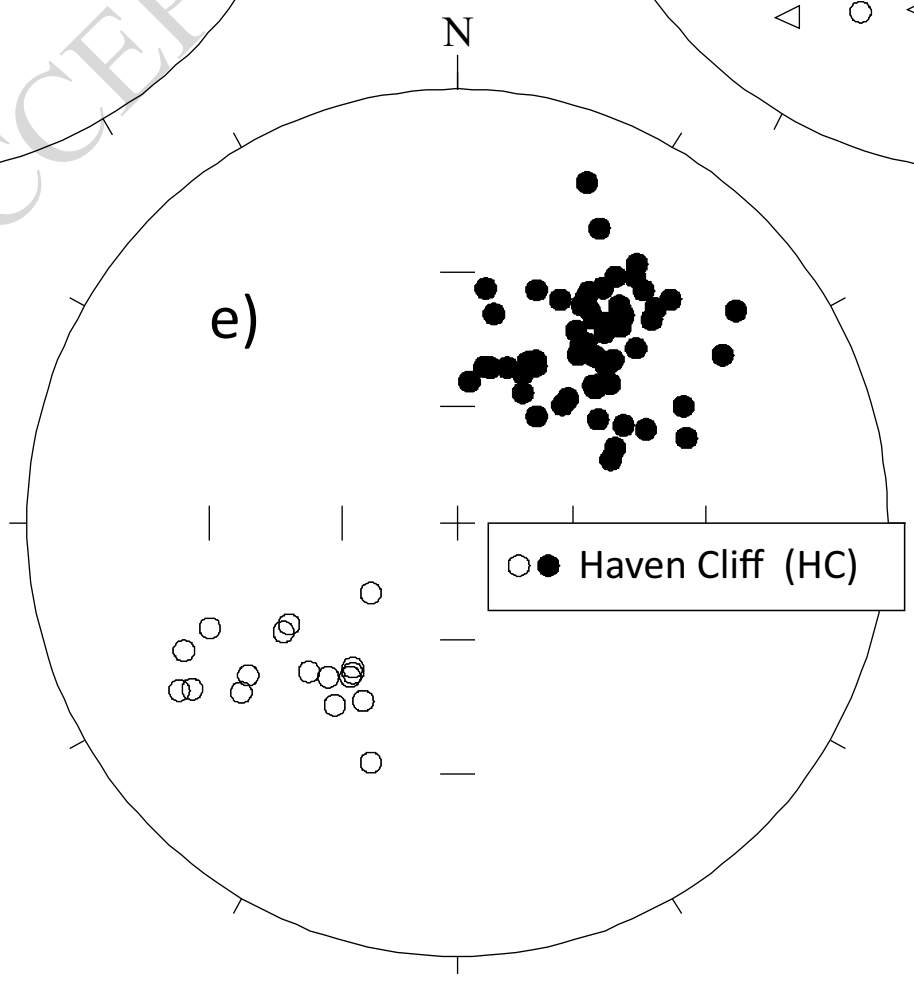

Fig. 9

Fig. 10

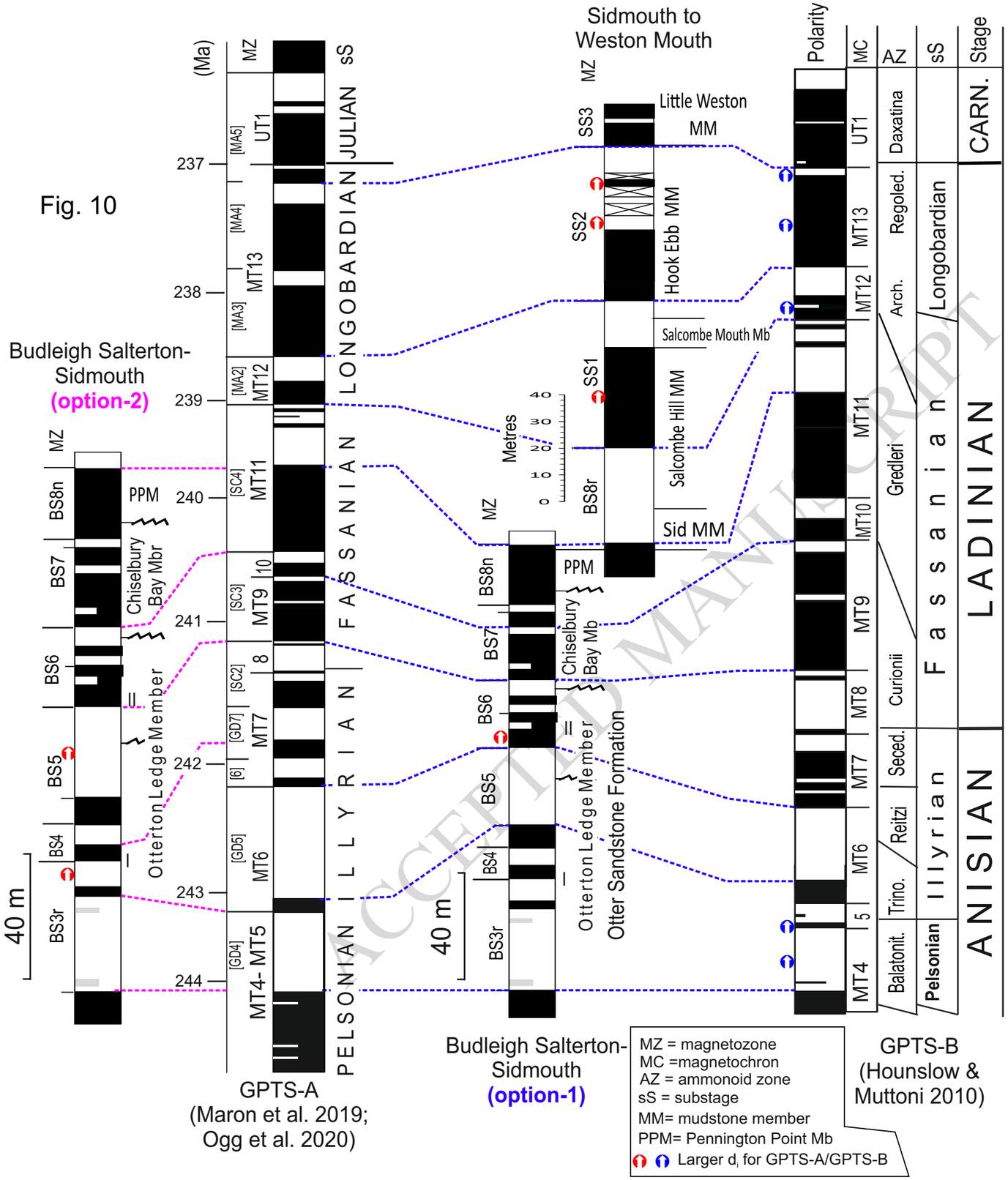

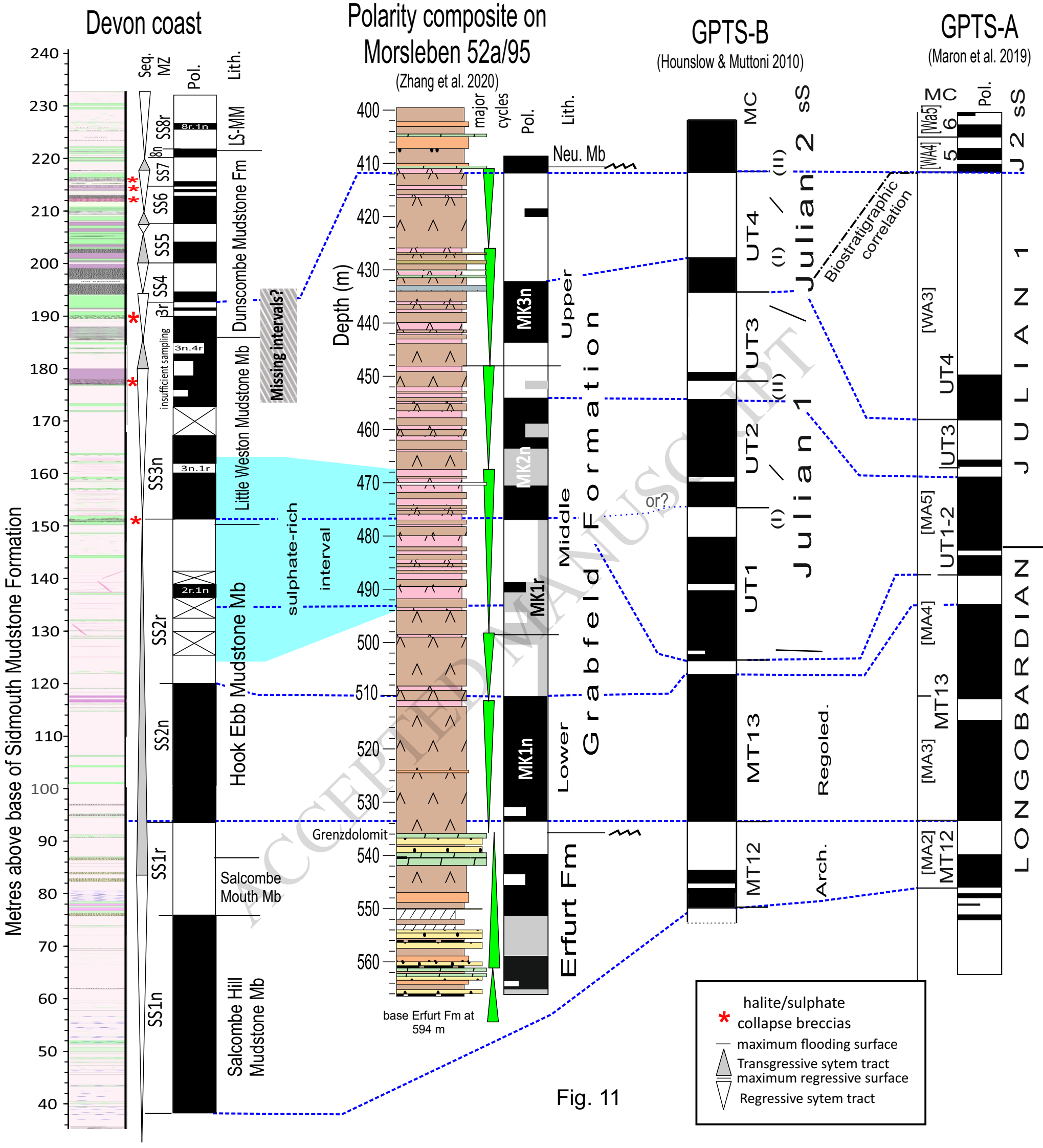

Fig. 11

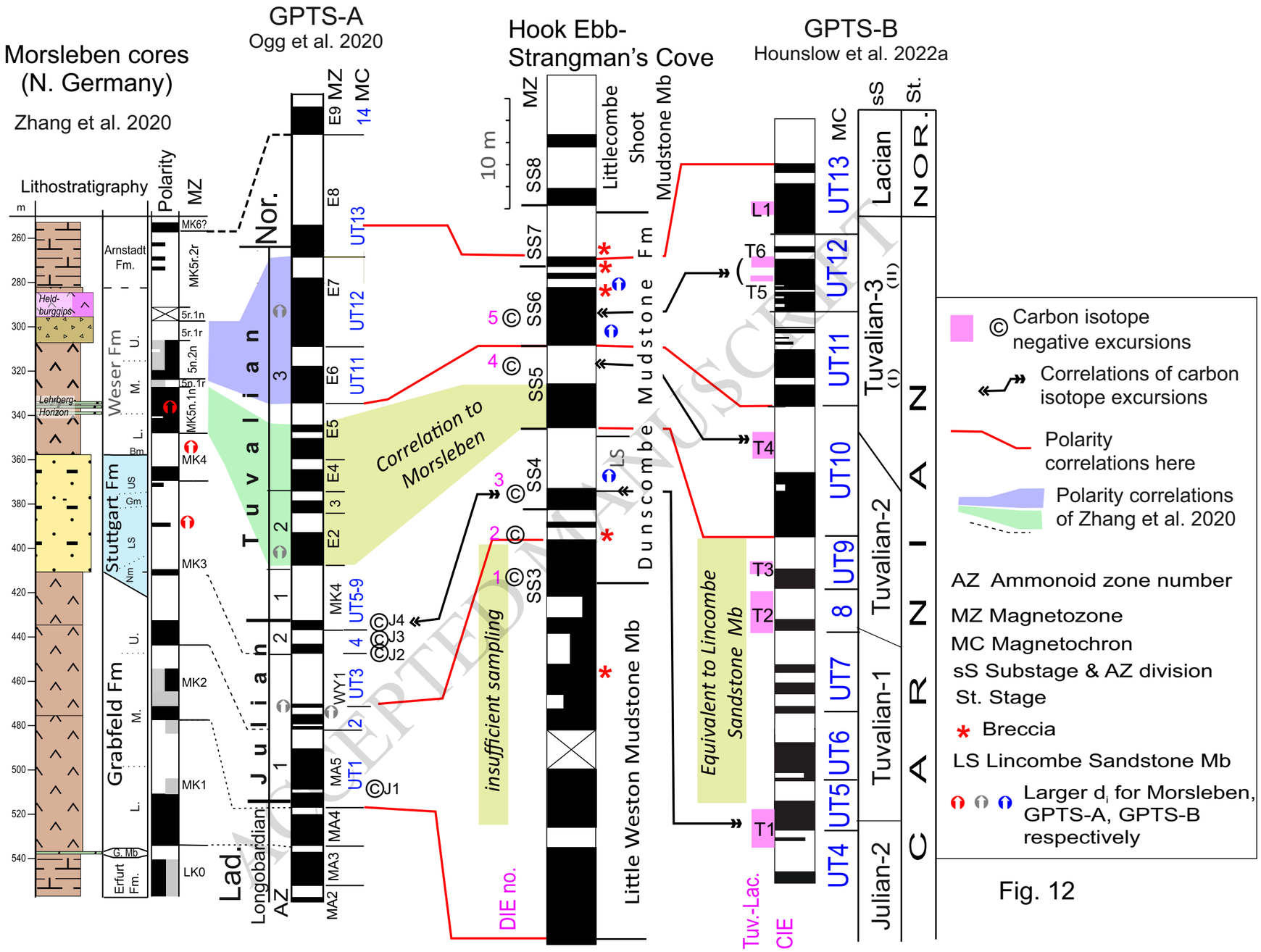

Fig. 12

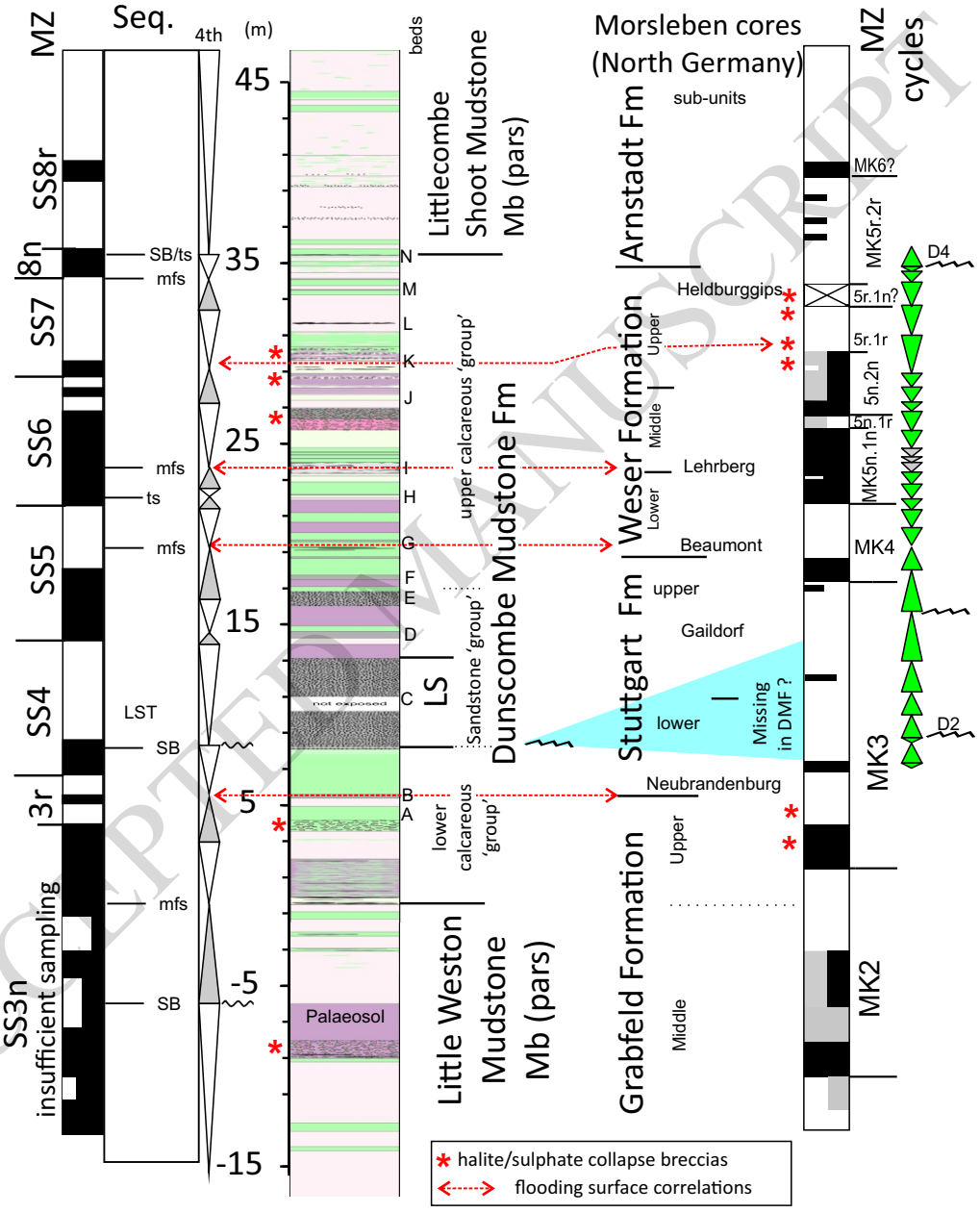

Fig. 13

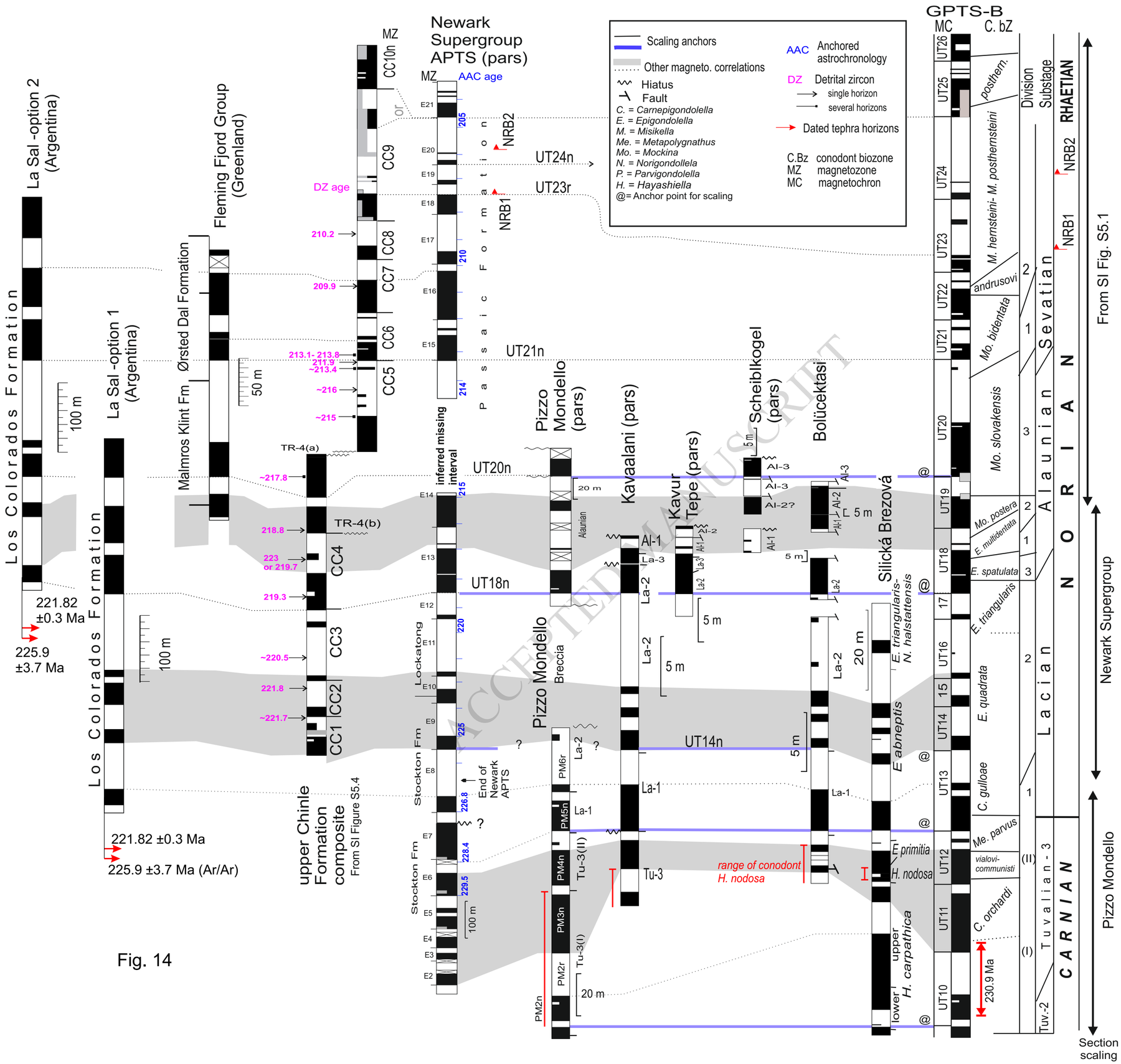

Fig. 14

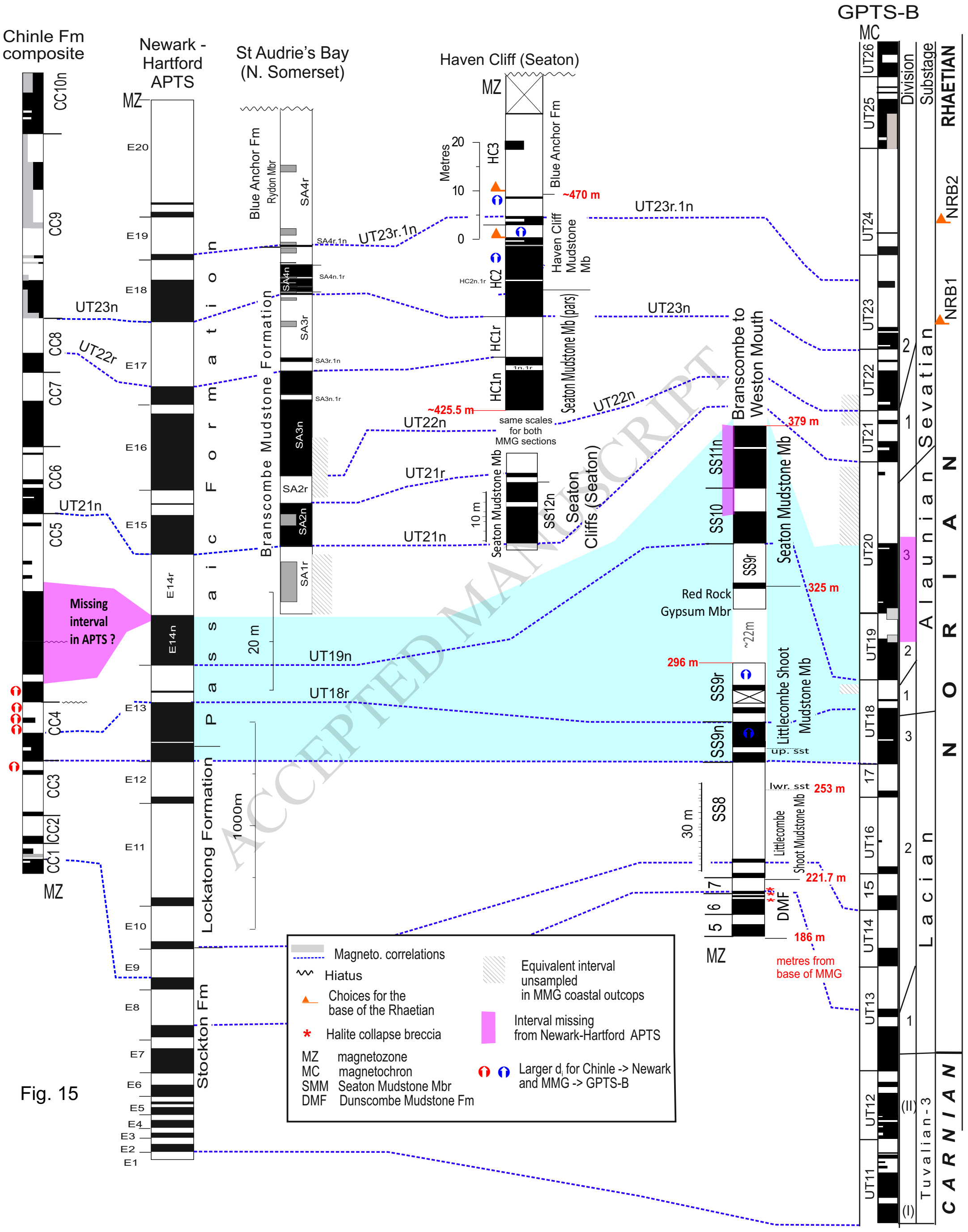

Fig. 15

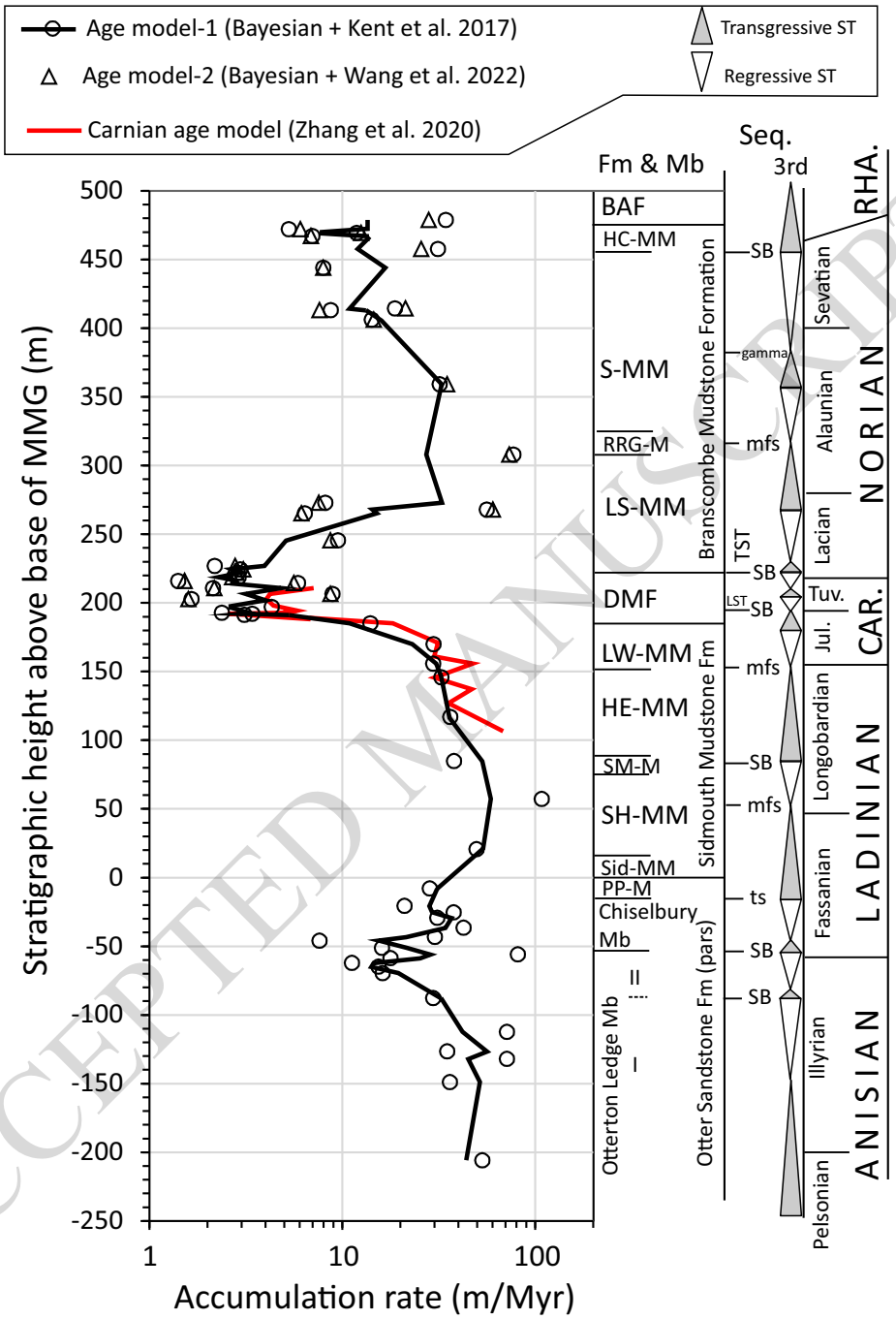

Fig. 16

Formation	**Member [thickness, metres]**	**Type locality**
Blue Anchor Fm (BAF)	[c. 30 incomplete] on Devon coast	Blue Anchor, Somerset
Branscombe Mudstone Fm (BMF)	Haven Cliff Mudstone Mb [20]	Haven Cliff
	Seaton Mudstone Mb [c.115 incomplete]	Branscombe Mouth to Seaton
	Red Rock Gypsum Mb [9.5]	Red Rock
	Littlecombe Shoot Mudstone Mb [78.6 incomplete]	Littlecombe Shoot
Dunscombe Mudstone Fm (DMF)	[35.7 incomplete[1]]	Strangman's Cove
Sidmouth Mudstone Fm (SMF)	Little Weston Mudstone Mb [34.6]	Hook Ebb
	Hook Ebb Mudstone Mb [63.4]	Salcombe Mouth to Hook Ebb
	Salcombe Mouth Siltstone Mb [11.0]	Salcombe Mouth
	Salcombe Hill Mudstone Mb [60.5]	Salcombe Hill to Salcombe Mouth
	Sid Mudstone Mb [15.5]	Sid outfall to Salcombe Hill
Otter Sandstone Fm (Sherwood Sandstone Group)	Pennington Point Mb [22]	Pennington Point (Sid outfall)

Table 1. Lithostratigraphic subdivision of the Mercia Mudstone Group exposed on the Devon coast (after Gallois, 2001, 2019).

Fm=Formation; Mb= Member. [1]Later sections have shown up to 41 m for the DMF.

Section [site code]	Section thickness (m)	Thickness sampled (m)	N/Ns	Grid Reference
Haven Cliff [HC]	67 (unknown gap at base, c 6 m gap at top)	60	164/81	SY2565 8972-SY 2730 8936
Seaton Cliff [SE]	29 (unknown gaps at base and top)	19.5	30/17	SY2382 8979
Red Rock- Branscombe Mouth [MB]	64; (c. 15m gap at base, unknown gap at top)	64	40/30	SY1984 8807-SY2029 8815
Littlecombe Shoot east [SH]	31	25	20/10	SY1800 8799-SY1984 8807
Littlecombe Shoot west [ML]	39	37	28/20	SY1691 8793-SY1800 8799
Strangman's Cove [MW]	61	57	93/44	SY 1691 8793
Salcombe Mouth-Hook Ebb [MD]	70	55	27/19	SY1462 8765-SY1566 8776
Sid Outfall-Salcombe Mouth [MS]	102	98	45/41	SY1290 8733-SY1462 8765
Total	463 plus gaps	~361	447/262	

Table 2. Summary of magnetostratigraphic sampling from the Mercia Mudstone Group, Sidmouth to Haven Cliff. Thicknesses are those shown on the SI FigsS1.1 to S1.7. Localities shown on Fig. 1, and details in SI Table S3.1. N=Number of specimens ;Ns= Number of sampled horizons.

Reference GPTS	**Comparison**	**Fig.**	**SMI, PSI, P_{RV}**	**Nc, d_{median}**	**Absent/ extra magnetozones**
GPTS-A (Option-1); GD4r-MA5n	BS3r-SS3n	11	0.53,0.64,<0.001	24, 0.73	SC4r.1n, SC4r.2n, SC2r.1n, SC2r.2n / BS3r.1n BS4n, BS4r,
GPTS-A (Option-2); GD4r-MA5n	BS3r-SS3n	11	0.37,0.59, 0.002	22, 0.74	GD6n,GD6r, SC2r.1n, SC4r.1n, SC4r.2n/ BS7n.2r, BS7n.1n, BS7r
GPTS-B ; MT4r-UT1n	BS3r-SS3n	11	0.42,0.67, <0.001	24, 0.48	MT7n.1r, MT8r.1n, MT11r.1n, MT11r.2n/ BS4n SS2r.1n,SS2r.2r.
GPTS-A ; GD4n- MA5n	GPTS-B; MT4n-UT1n	11	0.78,0.91, <0.001	31, 0.37	MT5n/ MA3r, MA4n
Morsleben;MK3r.1r-MK5r.1r	SS3r-SS6r	13	0.64,0.54, 0.47	9, 0.92	MK5r.1n/ SS6r.1n, SS7n
GPTS-A; WY1n.2r-E9r	SS3r-SS8r	13	0.52, 0.58, 0.046	15, 0.91	E2r,E3r,E4r,E5n.1r/none
GPTS-B ; UT4n-UT14r	SS3r.1n- SS8r	13	0.51, 0.72, <0.001	14, 0.77	UT6n-UT9n, UT11r.1n, UT11n.1r, UT12r.1n, UT13n.1r/ none
GPTS-B ; UT4n- UT14r	GPTS-A; WY1r.1r-E9r	13	0.4, 0.52, 0.030	20, 0.71	UT8n, UT11n.1r, UT11r.1n, UT12r.1n, UT13n.1r / E15n.1r
GPTS-B ; UT13r.2r- UT24n	SS7r—HC3r.1n	16	0.42, 0.65, <0.001	28, 0.84	None/ SS9r.1n, SS9r.3n
Chinle; CC1n-CC9r.2r	SS8n- HC3r	16	0.36, 0.49, 0.014	26, 1.08	CC3n, CC3r.1n, CC6r.1n / SS9r.1n, SS9r.3n, SS12n.1r, HC2n.1r, HC3r.1n
Newark ATS; E9r-E20n	Chinle; CC1r.1r-CC9r.2n	16	0.36, 0.65, <0.001	26, 0.87	E13n.1r/ CC5n.1r, CC5n.2n, CC5r.1n, CC6n.1r,
GPTS-B ; UT14r- UT24n	Chinle; CC1r.1r-CC9r.2n	16	0.48, 0.80, <0.001	30, 0.66	None/ CC5r.1n

Table 3. Statistics for the comparison of magnetic polarity correlation models in this work. The reference and comparison are the polarity patterns correlated, as shown in the figure number, using the magnetozone/chron ranges indicated. SMI, PSI= similarity of matrices index and Procrustes similarity index determined as in Indahl et al. (2018), with ranges 0-1.0 (no to perfect similarity). P_{RV}= the RV-based statistic testing the probability of association between the two sets (<0.05=strong association) as in Josse et al. (2007). d_{median}= median Euclidean distance of the number of magnetozones/chrons in the comparison (Nc), larger d_{median} correspond to larger average divergence. Absent/extra= magnetozones absent from the reference GPTS set used/ additional magnetozones in the comparison set not shown in the reference set. See SI for data details.

Supplementary information for: Magnetostratigraphy of the Mercia Mudstone Group (Devon, UK): Implications for regional relationships and chronostratigraphy in the Late Triassic of western Europe.

Mark W. Hounslow and Ramues W. Gallois

This supplementary information contains the following:

- Section S1: Additional lithological details of the members and sections, section sampling details and detailed logs of the sampling locations (Figs. S1.1 to S1.7 and Table S1.1). Inferred sequence stratigraphic boundaries (Table S1.2).
- Section S2: Magnetic mineralogy details (Figs S2.1 to S2.10)
- Section S3: Details about the low stability component, stratigraphic distribution of the blocking temperatures ranges of the LT and ChRM components (Figs S3.1 to S3.6). Demagnetisation diagrams for representative specimens (Figs. S3.7 to S3.9), mean directions and reversal tests of formation units in MMG (Table S3.1).
- Section S4: Summary of the virtual geomagnetic pole (VGP) data in relationship to other Triassic poles from stable Europe (Fig. S4.1 and Table S4.1)
- Section S5. Reference magnetostratigraphic sections and the GPTS-B for the Norian and Rhaetian (Figs. S5.1 to S5.4)
    - S5.1 The upper Chinle Group/Fm magnetostratigraphy and U-Pb dates
        - S5.1.1. Petrified Forest National Park (PEFO), Arizona (Fig. S5.3)
        - S5.1.2. Chama Basin, New Mexico
        - S5.1.3 Sangre de Cristo Mountains and Tucumcari Basins, New Mexico
        - S5.1.4. Construction of the Chinle Fm composite (Fig. S5.4)
- Supplementary references
- All the specimen-based data reported here and that from the Otter Sandstone Fm in the associated Excel file.

S1. Section sampling details and lithological logs

The lower parts of the cliffs are locally partially obscured by landslide debris (main text Fig. 1), and the uppermost parts comprise vertical cliffs composed of Cretaceous age Upper Greensand Formation and Chalk Group sediments that rest unconformably on the MMG. A

low easterly dip (2-3°) allows much of the MMG succession to be examined at or a little above beach level. The sections can only be accessed at Sidmouth, Salcombe Mouth, Weston Mouth, Branscombe Mouth and Seaton (main text Fig. 1). The sections in the highest part of the MMG, the Haven Cliff Mudstone Member and the Blue Anchor Formation, crop out east of the outfall of the River Axe at Haven Cliff to Culverhole Point. Some of the sections are inaccessible at high tide, and some are prone to relatively frequent rock falls and landslides, factors which need considering if planning visits.

The sections sampled are:

A) Sidmouth to Salcombe Mouth (sample code MS; main text Fig. 2; SI Fig. S1.1): This section is between the outfall of the River Sid and Salcombe Mouth with the sampling extended up the cliff/gully at the Salcombe Mouth end of the section (from MS40 to 43; Figs. 2; S1.2). This is essentially the section studied by Creer (1955, 1959), although our sampling probably extends beyond the 52 m examined by Creer.

B) Salcombe Mouth to Hook Ebb (sample code MD; main text Fig. 3, SI Figs. S1.2, S1.3): The youngest sample is 17.5m below the base of the DMF which was inaccessible above Hook Ebb at the time of sampling.

C) Strangman's Cove (code MW; Fig. 4, SI Figs. S1.3, S1.4): This is the type section of the DMF and was sampled by Baranyi et al. (2019) for palynology. The quality and extent of the exposure here varies from year to year, so the sampling was done over several years between 2000 and 2014, with the later sampling through the base of the DMF into the top of the Hook Ebb Mudstone, which had not been exposed in earlier years. Initial data showed many magnetozones in the DMF, so later additional sampling included many fill-ins, located onto the same logs. Above the DMF are the red mudstones of the Littlecombe Shoot Mudstone Mb (top of Fig. 4). These are partly decalcified high in the cliff at this locality, so upward sampling was limited here. This upper part overlaps with the better preserved MMG at the Littlecombe Shoot west section.

D) Littlecombe Shoot west (sample code ML; lower panels in main text Fig. 5, SI Fig. S1.4): At the base of the section, weathered/slipped DMF mudstones are overlain by red mudstones of the Littlecombe Shoot Mudstone Mb. The member contains two prominent beds of sandstone which act as laterally persistent marker bands in the cliffs.

E) Littlecombe Shoot east (sample code SH; upper panels in main text Fig. 5, Figs. S1.4, S1.5): This short section, in a steep part of the cliff, overlaps with the sandstone beds in the top part of the Littlecombe Shoot west section. Between Littlecombe Shoot west and Red Rock [SY1984 8807] the lower cliffs are obscured by extensive landslide deposits and vegetation. In the absence of evidence for faulting or change of bedding dip angle, the gap between the top of the youngest Littlecombe Shoot-east exposure and the base of the Red Rock- Branscombe Mouth section is estimated at 15 m. This is a ~22 m magnetostratigraphic sampling gap to the lowest sample in the overlying Red Rock-Branscombe Mouth section. The sampling gaps are clear in the detailed logs below.

F) Red Rock to Branscombe Mouth (code MB; main text Fig. 6, SI Fig. S1.5): Three sub-sections were sampled covering an interval from 2.5 m above the exposed base of the Red Rock Gypsum Mb to 54 m into the Seaton Mudstone Mb (SI Fig. S1.5). Strong colour banding allowed sub-sections to be correlated easily. The youngest part of the section exposes red mudstones with cm-thick sandstone laminae high in the cliff west of Branscombe Mouth, overlain unconformably by the Cretaceous Upper Greensand Formation (Fig. 6).

G) Seaton Cliffs (code SE; main text Fig. 7, SI Fig, S1.6): Samples collected in 2003 from two sections in the Seaton Mudstone Mb fall within the Axe Valley Fault Zone at Seaton. The section sampled at Seaton (SI Fig. S1.6) was the best exposed succession in a group of five fault-bounded blocks that lie within the fault-bounded valley of the River Axe. Most of the successions within these fault blocks are poorly exposed due to landslides. Seismic-reflection surveys across the valley indicate that both the Axe Valley boundary faults downthrow the top of the DMF ~100 m to the west (Edwards and Gallois 2004 fig. 6). To the west of the sampled section, up to a maximum of 40 m of Seaton Mudstone (older than the sampled section) is poorly exposed within the valley, and although some of the lithologies are like those in the Branscombe section (SI Fig. S1.5), the Red Rock Gypsum is not exposed. To the east of the sampled section, up to a maximum of 40 m of partially exposed Seaton Mudstone is lithologically different from that exposed in Haven Cliff. The regional east-directed dip of ~2° is maintained throughout these easterly sections which suggests that they are younger than the sampled section. Neither the Haven Cliff Mudstone Mb nor the BAF are exposed in the Axe valley fault system. These factors, and the fact that marker-bed correlation cannot be made between the Seaton sections and those

outcrops to the west of the town at Branscombe Mouth or east in the Haven Cliff section, suggest that the sampled Seaton section likely falls between the top and base of the sampled sections west and east of the town. Estimates of the thicknesses of the successions exposed in the individual fault blocks suggests that the sampled section represents ~25% of the total Seaton Mudstone Mb in the fault blocks. At the time of writing, these sections are now in a poorer and less accessible condition than when sampled, due to a combination of landslides and sea-defence works.

H) Haven Cliff (code HC, main text Fig. 8, SI Fig. S1.7). This covers the upper part of the Branscombe Mudstone Fm and most of the Blue Anchor Fm (BAF), although an additional ~13 m from the top of the BAF was not sampled (Fig S1.7). This section was also sampled in a second field season to refine polarity boundary positions.

1:100 scale when printed in A3 format

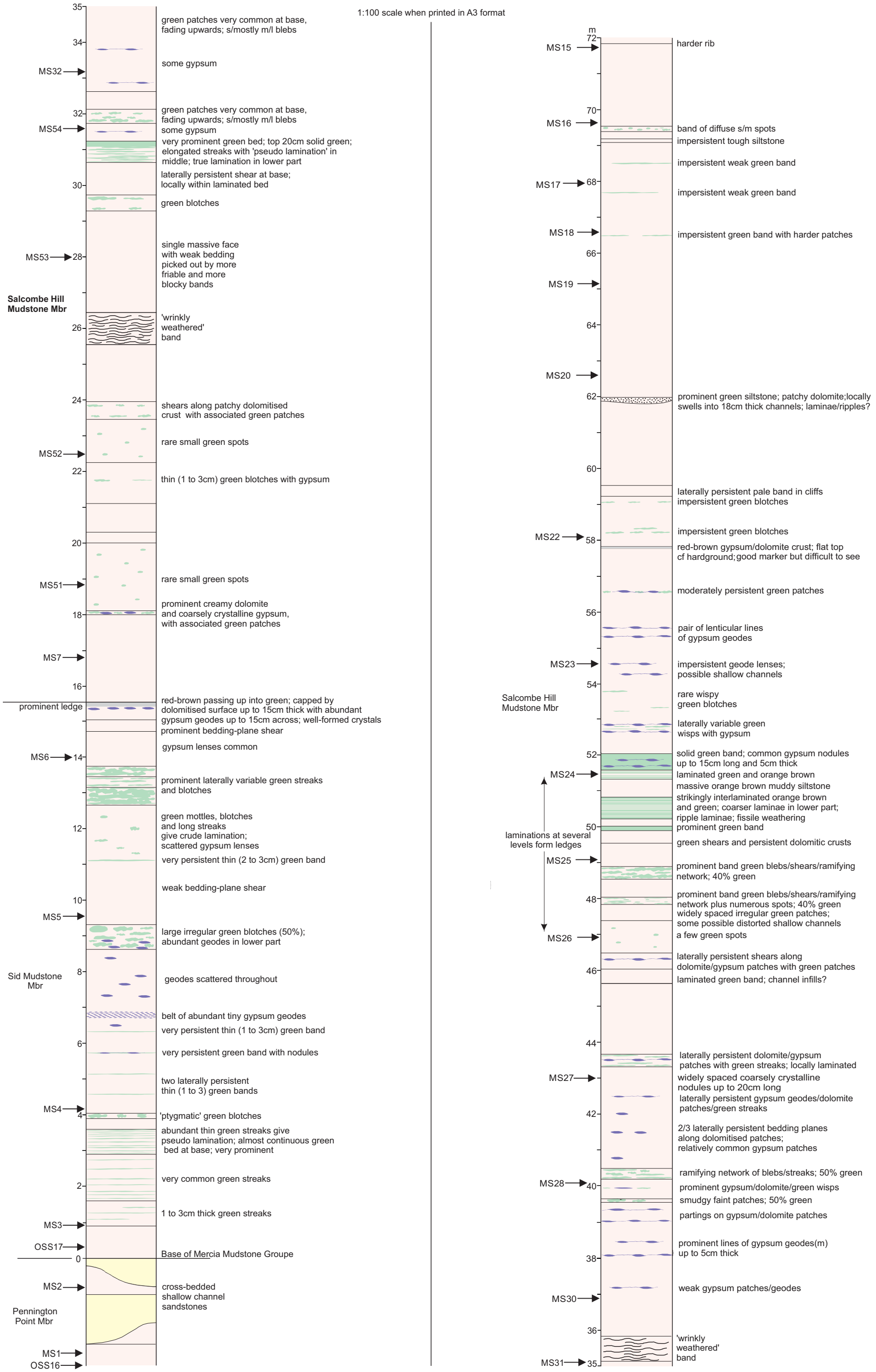

Figure S1.1. Sid outfall (Sidmouth) [SY 1290 8733] to Salcombe Mouth [SY 1462 8765]. Arrows indicate the sample number (MS). The OSS codes relate to the samples of Hounslow & Mcintosh (2003). See Fig. S1.6 for key. Not shown on this log are MS55, MS56 at 4.45 m and 9.67m respectively below the base of the MMG. MS56 is 0.23m below OSS3 measured by Hounslow & McIntosh (2003).

Figure S1.2. Salcombe Mouth [SY 1462 8765] to Hook Ebb [SY 1566 8776] section (MD samples). The MS samples belong to the Sidmouth to Salcombe Mouth section.

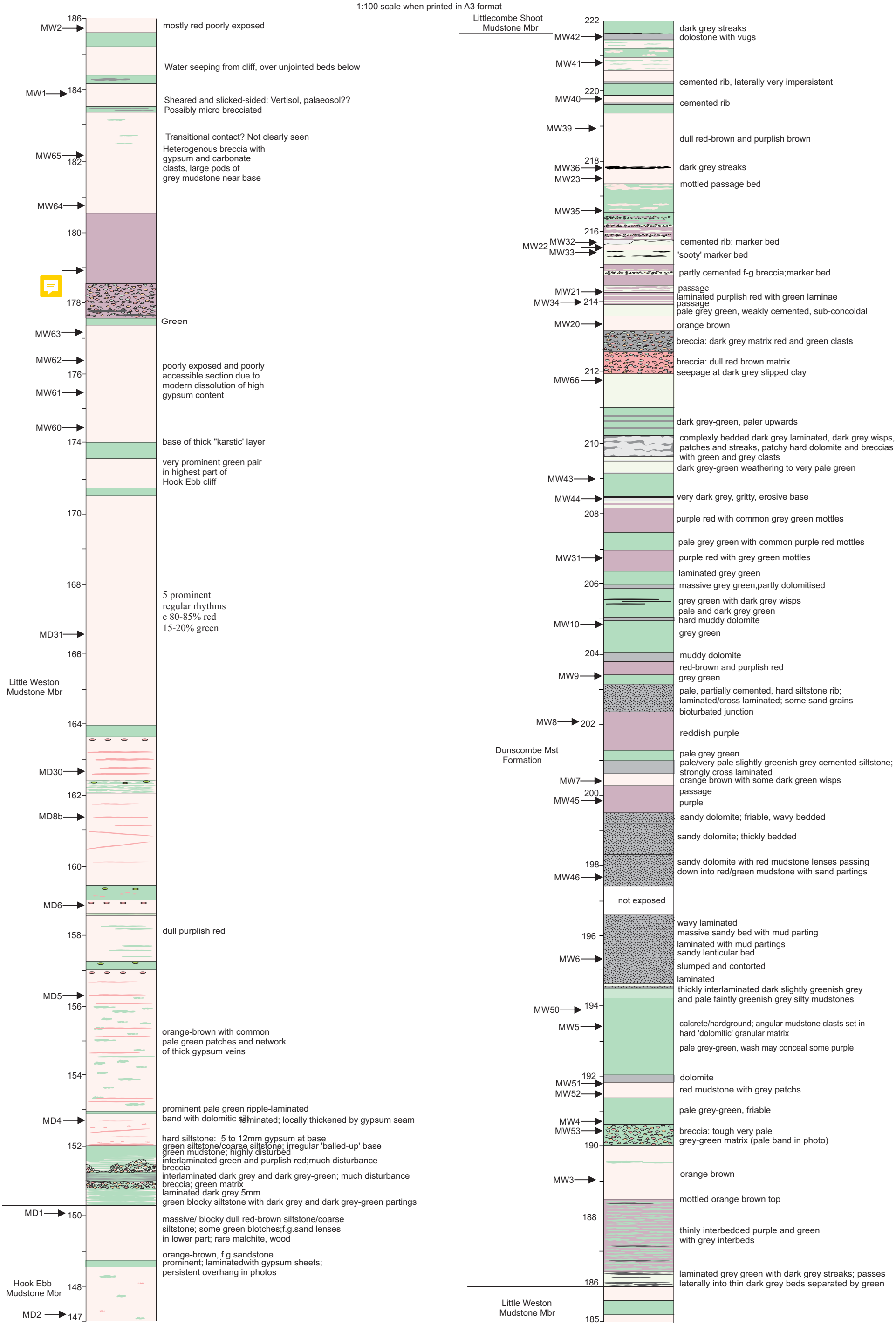

Figure S1.3. The upper part of the Salcombe Mouth -Hook Ebb section Hook Ebb [SY 1566 8776] (MD samples), and lower and mid part of the Strangeman's Cove (MW sample codes, [SY 1691 8793] section.

1:100 scale when printed in A3 format

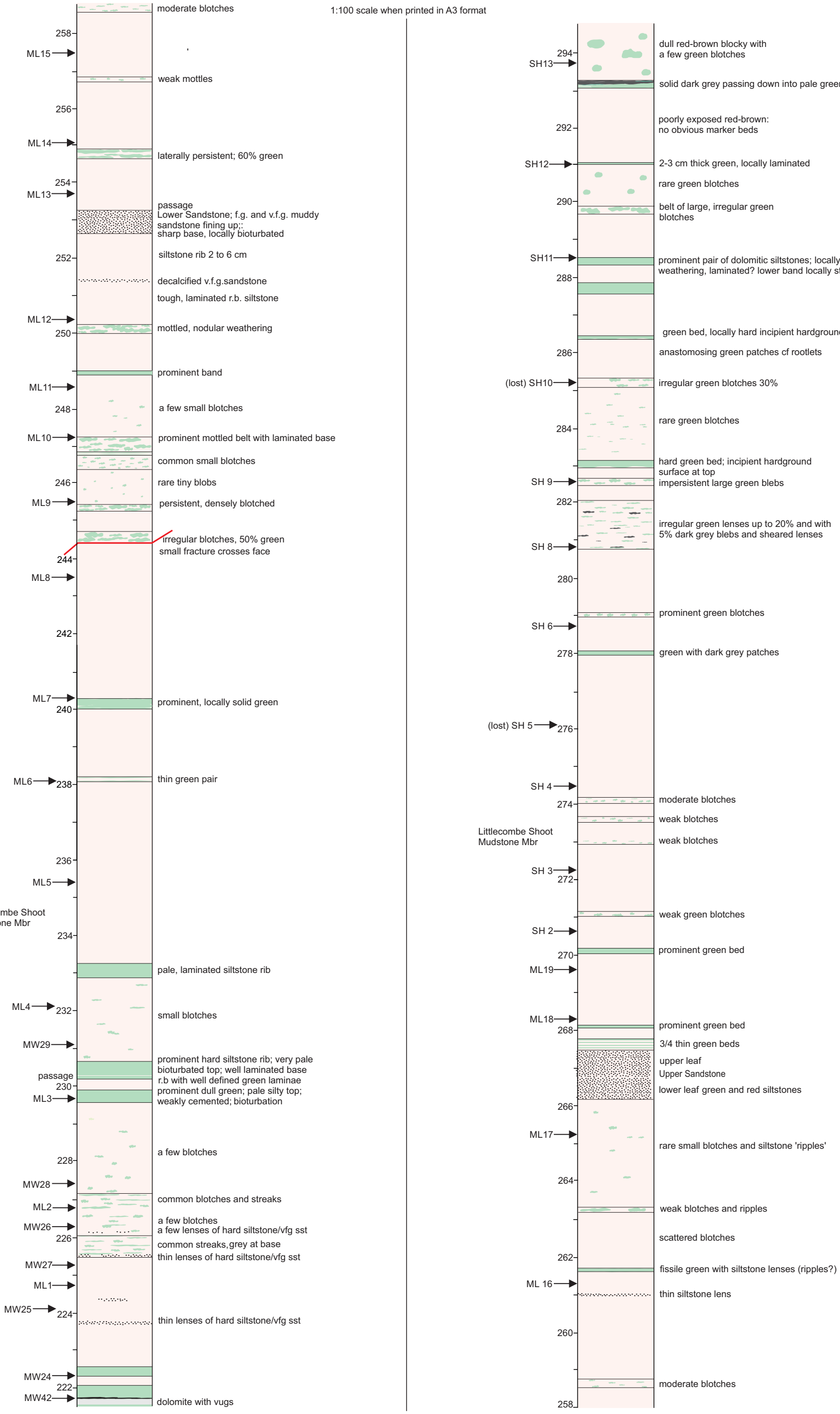

Fig. S1.4. The upper part of the Strangeman's Cove section (MW sample codes [SY 1691 8793]) and the Littlecombe Shoot sections (ML and SH sample codes) [SY 1828 8815].

1:100 scale when printed in A3 format

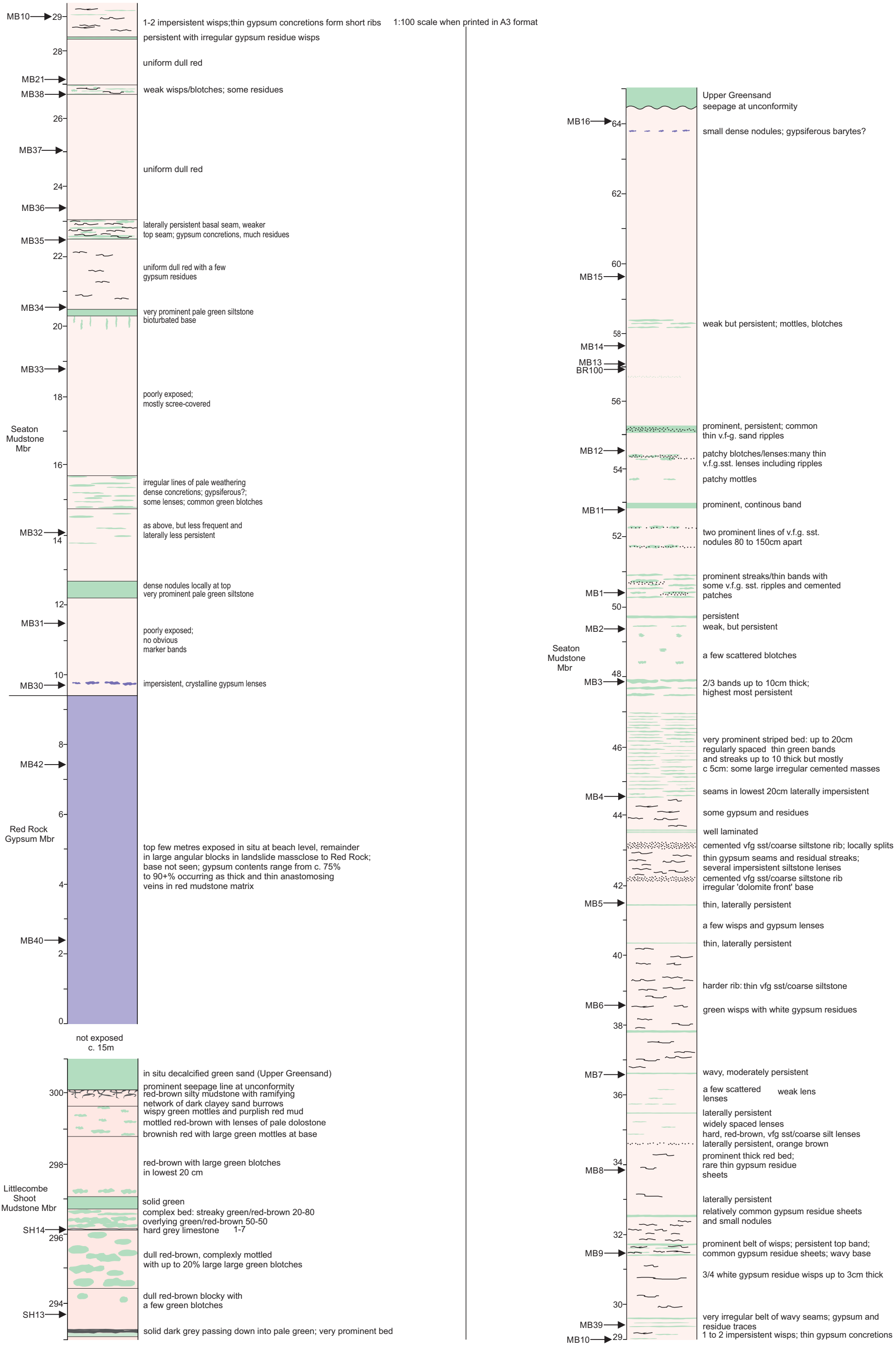

Fig. S1.5 The top-part of the Littlecombe Shoot section (SH sample codes) and the Branscombe Mouth section (MB sample codes). Red Rock [SY 1984 8807 sample MB40] to Branscombe [SY 2029 8815, sample MB16].

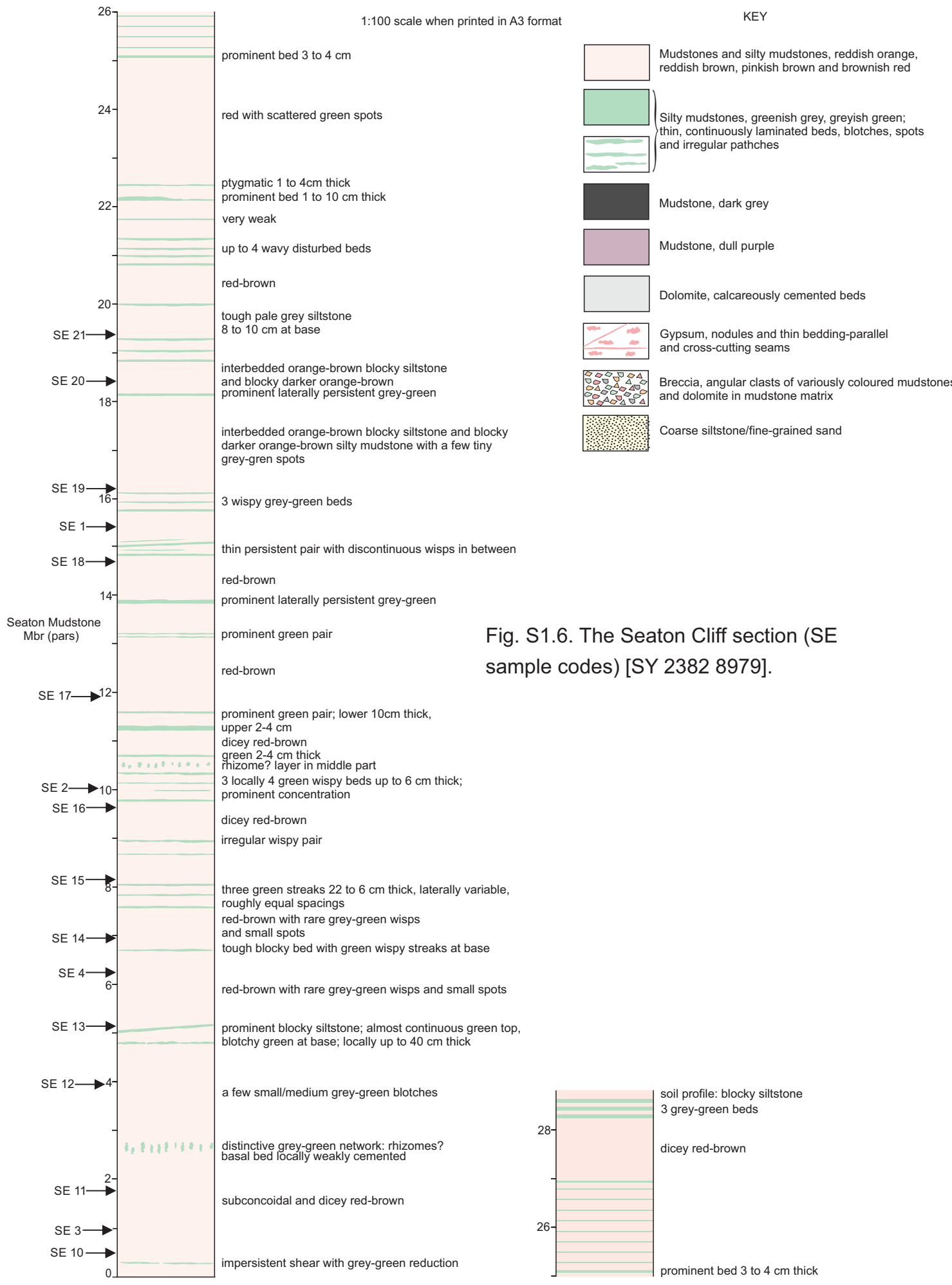

Fig. S1.6. The Seaton Cliff section (SE sample codes) [SY 2382 8979].

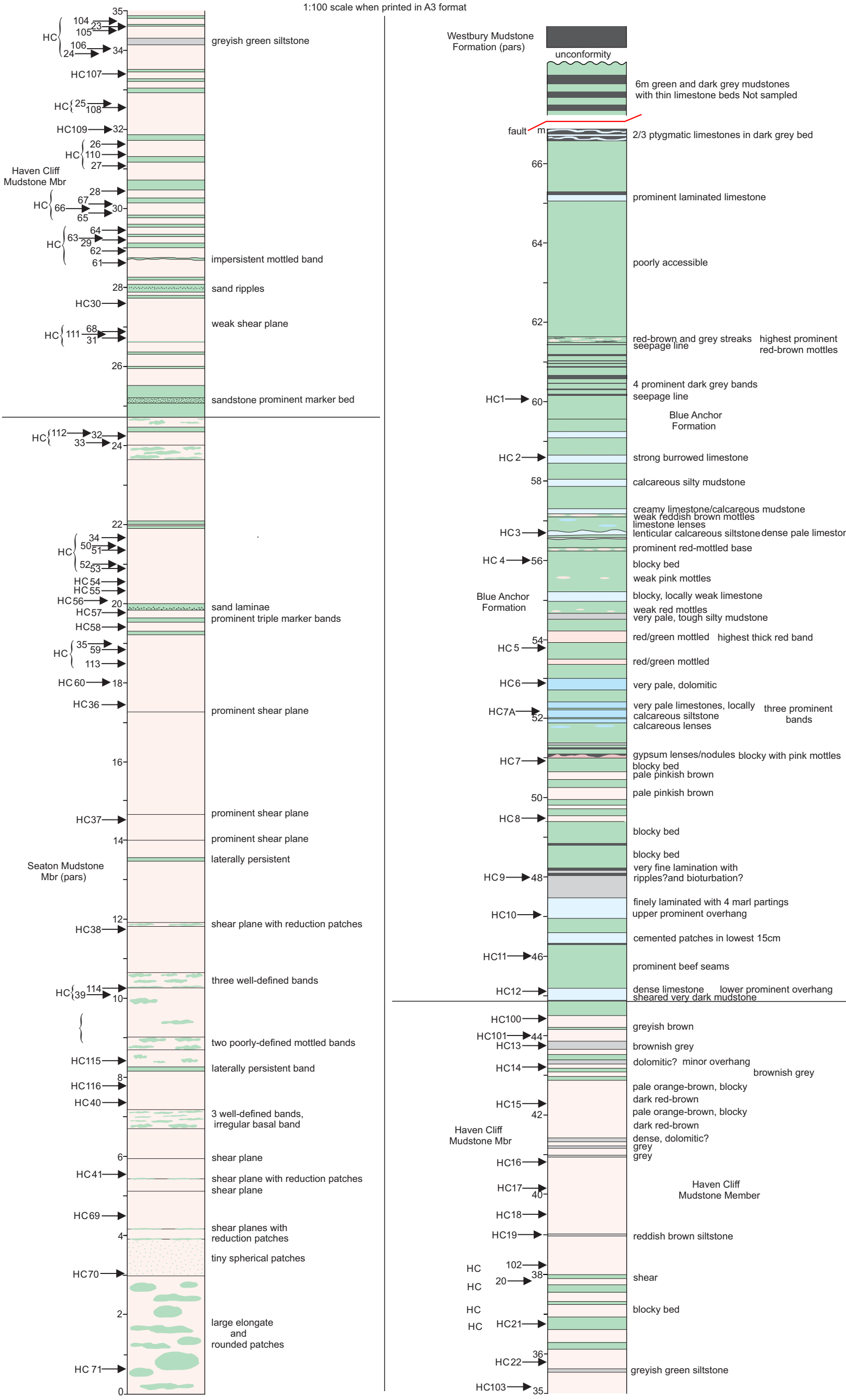

Figure S1.7. Haven Cliff [SY 2565 8972 to SY 2730 8936].

Supplementary Table S1.1. Lithology of the lithostratigraphic units of the sub-divided Mercia Mudstone Group. [1] of Sidmouth Mudstone Formation, [2] of Branscombe Mudstone Formation.

Unit name	**Lithology/ *defined location***
Blue Anchor Formation	Interbedded grey, green and rarely red calcitic and dolomitic mudstones.
[2]Haven Cliff Mudstone Mb	Interbedded green and red dolomitic and calcitic mudstones, with occasional siltstones (the 'variegated marls' of older usage).
[2]Seaton Mudstone Mb	Orange-red and occasionally green calcitic and dolomitic mudstones and occasional thin siltstones.
[2]Red Rock Gypsum Mb	Gypsum-cemented orange-red mudstone, with commonly developed mud breccia texture
[2]Littlecombe Shoot Mudstone Mb	Orange red mudstones with several prominent sandstone horizons and occasional green siltstone horizons.
Dunscombe Mudstone Fm (DMF)	Interbedded pale to dark grey, pale green, dark reddish brown to purple and orange red calcareous mudstones. Also has well-developed thin white siltstones and silty sandstones. Some mudflake conglomerates are also present. Solution breccias indicate thick former halite and gypsum deposits.
[1]Little Weston Mudstone Mb	Interbedded orange red and dark red dolomitic and calcitic mudstones, with extensive gypsum seams and veins
[1]Hook Ebb Mudstone Mb	Orange red dolomitic and calcitic mudstones, with occasional green mudstone and siltstone bands, and common horizons of gypsum seams and veins
[1]Salcombe Mouth Siltstone Mb	Orange red dolomitic and calcitic mudstones, with several thick beds of orange-red siltstone.
[1]Salcombe Hill Mudstone Mb	Orange red dolomitic and calcitic mudstones, with occasional thin green mudstone and siltstone bands, and layers of gypsum nodules.
[1]Sid Mudstone Mb	Orange red dolomitic and calcitic mudstones, with occasional thin green mudstone and siltstone bands.
Pennington Point Mb (of Otter Sandstone Fm)	Interbedded orange-red mudstones and sheet-flood, red silty sandstones. Characterised from the underlying Otter Sandstone by the absence of calcrete conglomerates and the development of large to small sandstone and mudstone filled channels.

Supplementary Table S1.2. Location and description of inferred sequence stratigraphic boundaries in the upper part of the Otter Sandstone Formation and the Mercia Mudstone Group from the Devon coast. These placements utilise principally the clastic playa model of Talbot et al. (1994) and Vollmer et al. (2008), as also shown in fig. 16.13 of Hounslow et al. (2012). The boundaries are organised base to top= oldest to youngest.

Fm/Mb location	**Type [metre level]**	**Characteristics, sources and associated samples**
Base of Haven Cliff MM	SB/ts [ca. 455, -20.1[A]]	Fig. 15. Green Marl with intervening sandstone layer- the base of which is prominent juncture between the red mudstones below and overlying increasingly frequent green and grey mudstones.
High gamma pick in middle of the Seaton MM	mfs [ca 382]	Fig. 15. This high gamma pick can be correlated across Wessex Basin (Galllois 2003; Newell 2018b), and probably corresponds to an interval of black mudstone layers in (low tide) beach-outcrops below the sampled Seaton Section (i.e. within the mid parts of the largely unseen SS11r; Fig. 14)
Mid Red Rock Gypsum Mb	mfs [ca. 316]	Fig. 15. This marker can be recognized throughout the Wessex Basin (Gallois 2003), and probably into the Worcester Basin also (Newell 2018b).
Base of Littlecombe Shoot MM	SB/ts [221.6]	Figs. 15, 16. Dolostone overlain by a thin dark grey mudstone (MW42 sample, WE205, and immediately underlying WE207, 208 of Baranyi et al. 2019).
Dunscombe Mudstone Fm	mfs [220.6]	Fig. 16. Complex of a dolostone with immediately overlying thin grey mudstone layers interbedded in red mudstone
Dunscombe Mudstone Fm	mfs [210]	Fig. 16. Dolostone with interbedded dark grey mudstones, with some brecciation (sample WE305, of Baranyi et al. 2019). Bed L of Gallois and Porter (2006).
Dunscombe Mudstone Fm	ts [208.4]	Fig. 16. Dark grey dolostone with a gritty erosive base, Bed H of Gallois and Porter (2006) (sample MW44 and WE301 of Baranyi et al. 2019).
Dunscombe Mudstone Fm	mfs [205.9]	Fig. 16. Muddy grey to green dolostone, immediately overlying green mudstone with thin grey mudstone layers (samples WE103, WE110, of Baranyi et al. 2019). Bed G of Gallois and Porter (2006).
Dunscombe Mudstone Fm	SB [194.6]	Figs. 15, 16, Down-cutting base of the Lincombe Sandstone, marked by distinct trace fossil assemblage (Porter and Gallois 2008). Base of bed C of Gallois and Porter (2006). Immediately underlying are samples WE106, WE105 of Baranyi et al. (2019).
Base of Dunscombe Mudstone Fm	mfs [186]	Fig. 16. Laminated grey green mudstone with thin dark grey mudstone layers (sample WE003 of Baranyi et al. (2019).
Little Weston MM	SB [180.5]	Fig. 16, purple mudstone with many slickensides and micro-brecciation (a palaeosol). Top is a prominent boundary between jointed mudstones above and unjointed mudstones in the underlying 3 m.
Salcombe Hill MM	mfs, [51.6]	Fig. 15. Green mudstone with gypsum nodules in top of an interval which is well laminated. Just above sample MS24.
Base Pennington Point Mb	ts, [-20.1[B]]	As placed by Newell (2018a), using the log scale in Hounslow and McIntosh(2003)- between samples OSS2 and OSS3.
Base Chiselbury Mb	SB, [-59.1[B]]	As placed by Newell (2018a), using the log scale in Hounslow and McIntosh(2003)- their sample CB6.
Base unit II of Otterton Ledge Mb	SB, [-88.2[B]]	As placed by Newell (2018a), using the log scale in Hounslow and McIntosh (2003)- between samples PB5 and PB6, base of unit C of Hounslow and McIntosh(2003) and unit II of the Otterton Ledge Mb of Newell (2018a).

Boundaries: SB= sequence boundary (mostly maximum regressive surface), ts=transgressive surface, mfs= maximum flooding surface. MM= Mudstone Member. [A]= below the base of the Blue Anchor Fm; [B]= below base of MMG. Metre level with respect to the base of the MMG (unless otherwise indicated)

S2. Magnetic mineralogy

A large proportion of the samples have rather similar K-NRM intensity relationships, with K between 150–300 x10^{-6} SI and intensity between 1–6 mA/m (Fig. S2.1). The exception are some red and non-red lithologies from the Dunscombe Mudstone Fm (DMF), Blue Anchor Fm and the Haven Cliff Mudstone Mb, which have K below 180 x10^{-6} SI and intensity in part below 1 mA/m (Fig. S2.1).

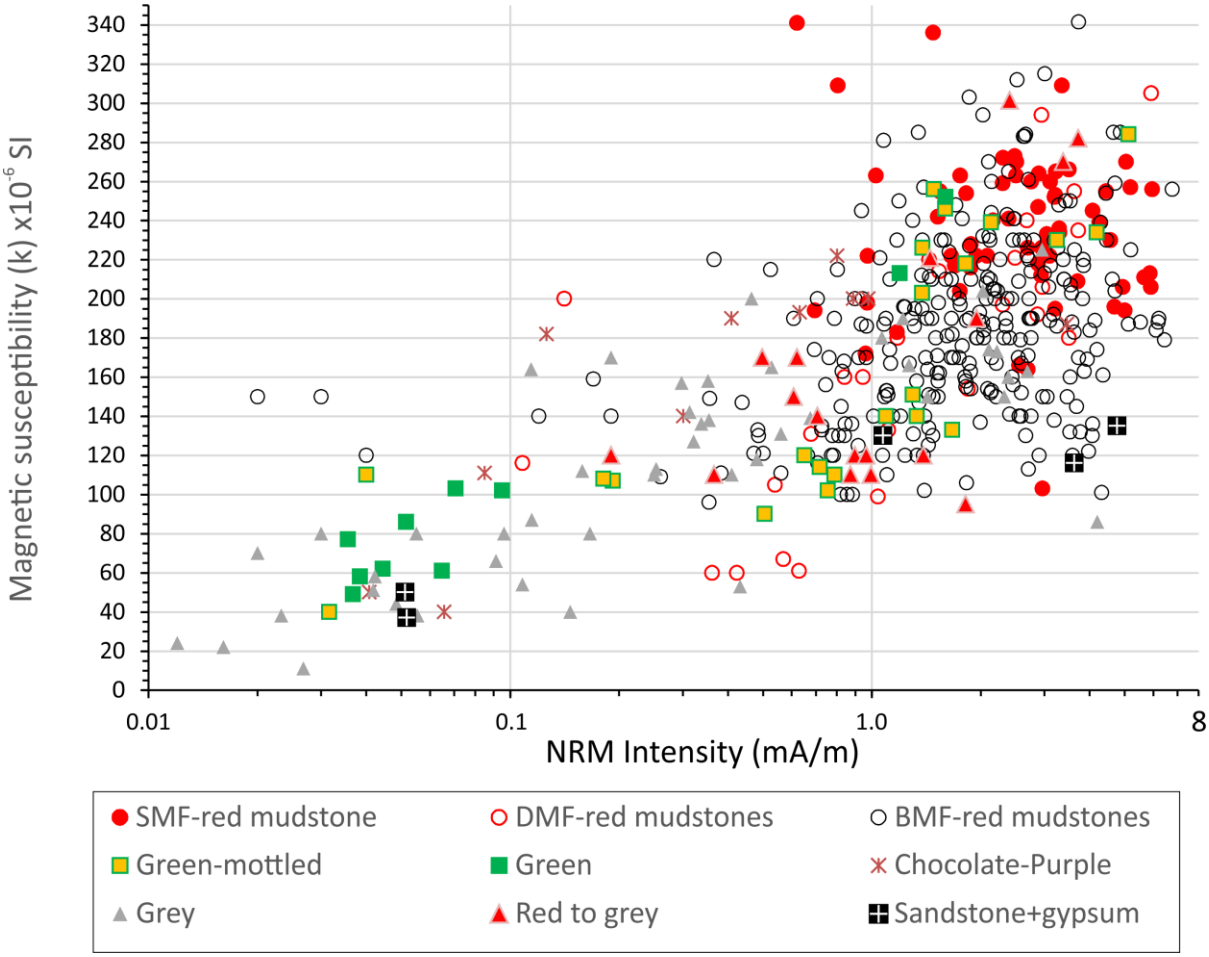

Fig. S2.1. The relationship between the NRM intensity and the magnetic susceptibility (K) for specimens. The red-mudstone samples are divided into formational groups (SMF=Sidmouth Mudstone Fm; DMF=Dunscombe Mudstone Fm; BMF=Branscombe Mudstone Fm). Other non-red samples (from both DMF, Blue Anchor Fm and Haven Cliff Mudstone Mb) are divided by dominant colour, or mixed-colour (green-mottled and red to grey). Chocolate coloured and purple-coloured mudstones are grouped together, as are sandstones (from the Lincombe Member) and gypsum (from Red Rock Gypsum Member). The major positive trend from small K and NRM intensity (predominantly grey mudstones and calcareous/dolomitic mudstones/limestones) to strongly magnetic red mudstones may be in part carbonate-content controlled, since some of those with the lowest K are also the most calcitic/dolomitic.

The natural remanence of the red mudstones is dominated by haematite which is indicated by: 1) unblocking ranges above 580ºC (Figs. S2.8, S2.9); 2) major remanence acquisition in magnetic fields above 0.1 T (Fig. S2.2a); 3) non-saturation of induced remanence (Mr) at 7 T (Fig. S2.2a); 4) magnetic extractions performed by Creer (1957) showed that the black ferromagnetic content (specularite) of the lower MMG was haematite, based on identification by X-ray diffraction. As

previously demonstrated by Creer (1961) the red mudstones of the Mercia Mudstones Group (MMG) are also rich in superparamagnetic haematite (MS5 and LP55 samples in Maher et al. 2004), which is seen in laboratory induced and remanent magnetisations (Fig. S2.2). Creer (1961) estimated that some 97% of the haematite in the MMG red mudstones should be superparamagnetic and some 0.12% of the total haematite carries the stable natural remanence.

The increase in Mr on cooling for the 2 T and 7 T remanence (France and Oldfield 2000), and the value of 56% for the % H parameter of Maher et al. (2004) indicates that sample MS5 probably contains important contributions from goethite. This is also borne out by the linear increase in Mr when cooling a 2 T or 7 T remanence acquired at 293 ºK (France and Oldfield 2000) as in Fig. S2.2c. However, SP haematite or goethite are not contributors to the ChRM which largely reside in blocking temperatures much larger than the Neel temperature of goethite (Figs. S2.8, S2.9). The absence of the Morin transition at 240 ºK in the data in Fig. S2.2c implies the bulk of the hematite is < 0.1 μm in size (Creer 1962; Maher et al. 2004). The rapid drop in J/J_{NRM} during demagnetisation at 100 -150ºC does perhaps suggest goethite may be important in carrying the LT component, or alternatively that the LT component is carried by haematite which unblocks at <350 ºC. Significantly, Maher et al. (2004) demonstrated that sample MS5 (from Sid Outfall-Salcombe Mouth section) when heated at 350ºC annealed the SP haematite which allowed emergence of the Morin transition, so demagnetisation to ca. 350ºC may simply be an annealing-induced demagnetisation, rather than true unblocking of haematite.

Non-red lithologies from the DMF and Blue Anchor Fm have a more complex mix of a soft, magnetite-like phase which fully demagnetises during AF demagnetisation (Fig. S2.9a,b,c) to a mix of haematite and this soft phase (blue curves in Figs. S2.9a,b,c), to non-red samples which are haematite dominated (Fig. S2.9d), much like the red mudstones in the DMF and other units.

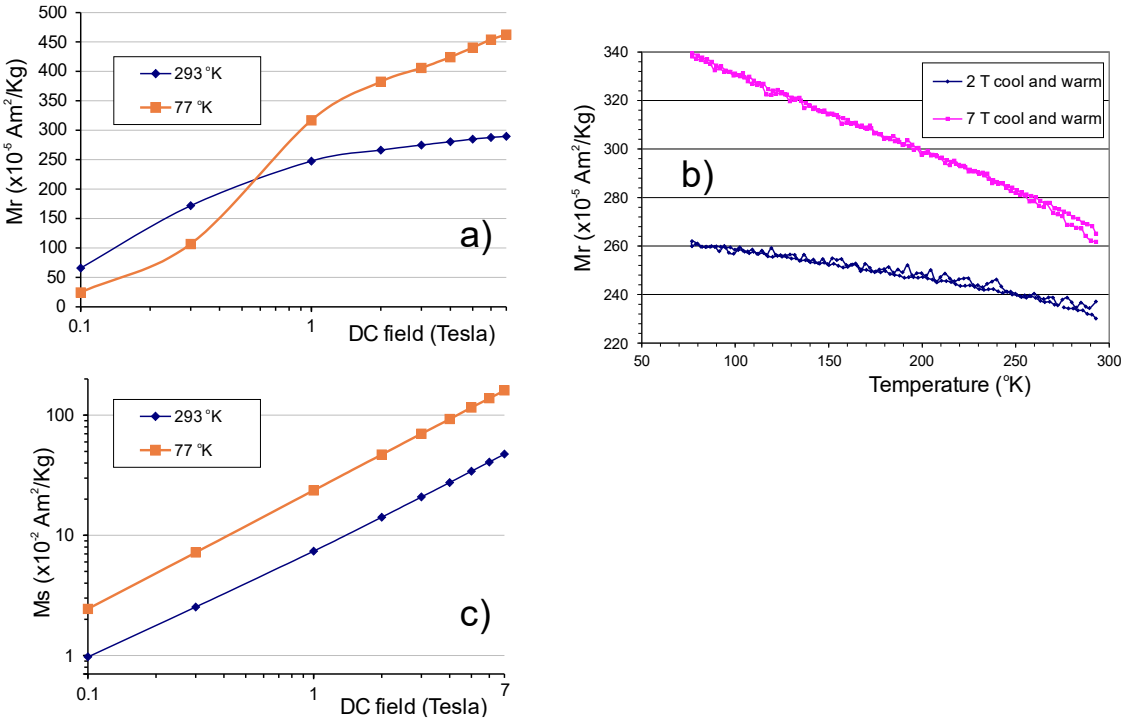

Fig. S2.2. High field and low temperature data for sample MS5 (Sid Mudstone Member). Mr= isothermal remanence, Ms=induced magnetisation. Note the non-saturation of Mr even at 7 T in a) ,

and Ms is linear with field indicating the dominance of paramagnetic/superparamagnetic susceptibility. The change in Mr between 293 and 77°K (12% at 2 T and 21% at 7 T) is smaller than the change in Ms (70% at 2T and 71% at 7 T) between 293 and 77°K indicating that most of the susceptibility is due to paramagnetic behaviour. Creer (1961, 1962) also proposed paramagnetic dominance of the susceptibility in his MMG samples from Devon and South Wales.

S2.1. Behaviour during demagnetisation

Changes in susceptibility of the red mudstones during the thermal demagnetisation heating steps tend to be small or show a gentle decline to around 400-450°C, when in many specimens there is an increase which peaks at around 500– 600°C, to be followed by the decline to 700°C (Figs. S2.3 to S2.7). Only specimens from the Seaton Section (SE code) do not show the dominance of this kind of behaviour in the red mudstones. Some red-mudstone specimens from the Hook Ebb-Strangman's Cove and Strangman's Cove-Littlecombe Shoot- Red Rock sections show more severe thermal alteration (Figs. S2.4g, h; S2.5h). Similar changes have been well documented in red-beds (Schwarz 1968; Shive and Diehl 1977, Duff 1979) and probably result either from clay mineral breakdown and/or annealing of the SP haematite fraction (remembering most of the susceptibility is due to the SP haematite fraction).

The non-red lithologies from the DMF show a range of behaviour from little change in K (Fig. S2.4d) to rather like the red-mudstone 'peaked' behaviour (Fig. S2.4c) to much larger increases in K (not well represented in the figures due to AF demagnetisation was used on these instead).

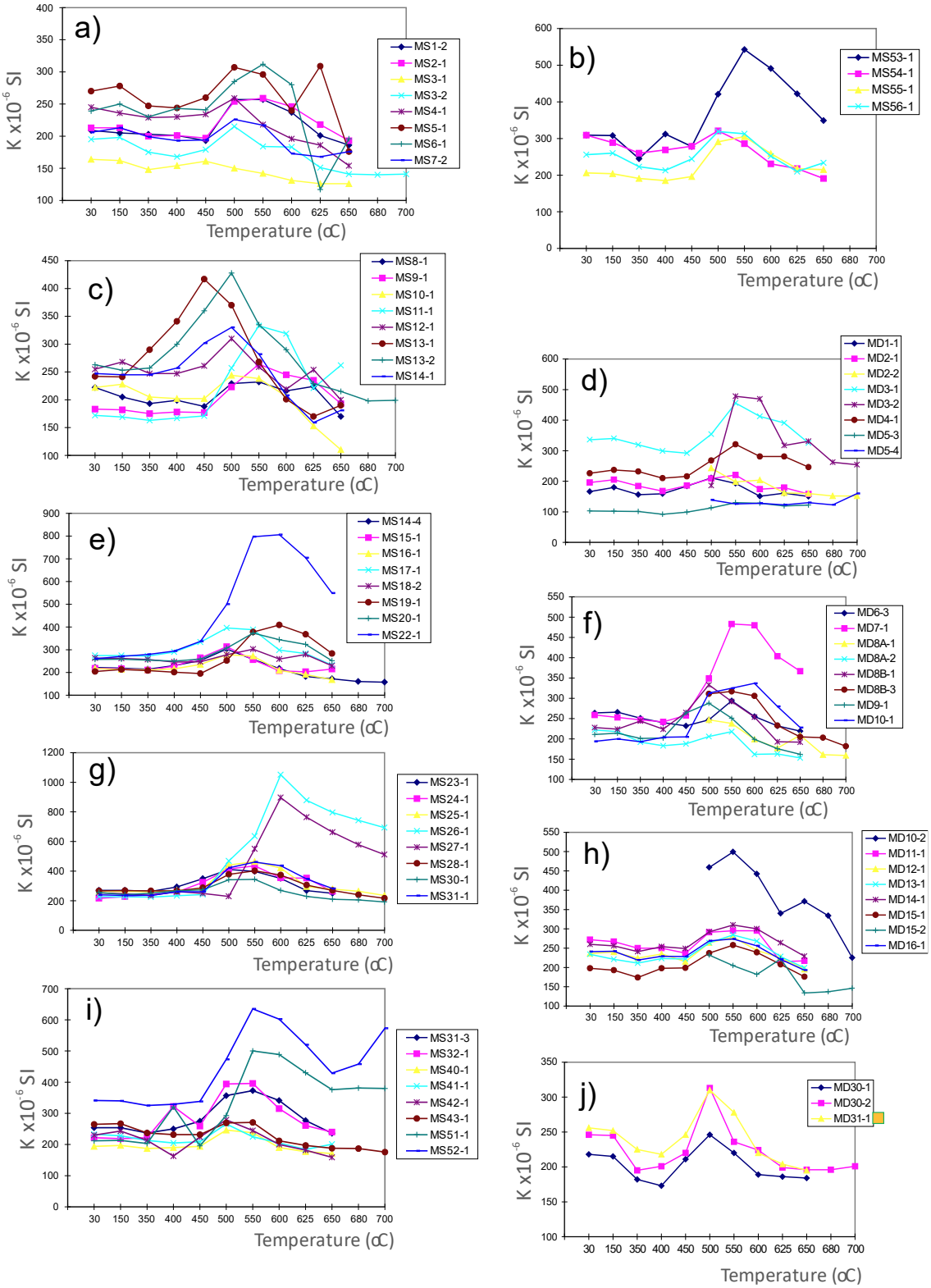

Fig. S2.3. Changes in magnetic susceptibility (K) with heating during thermal demagnetisations steps (measured at room temperature), for the Sid Outfall-Salcombe Mouth (MS) and Salcombe Mouth - Hook Ebb (MD) sections. The x-axis scale is not linear but shows the heating steps used in each case. Non red-lithologies marked with symbols as in Fig. S2.1 (e.g., MD31-1).

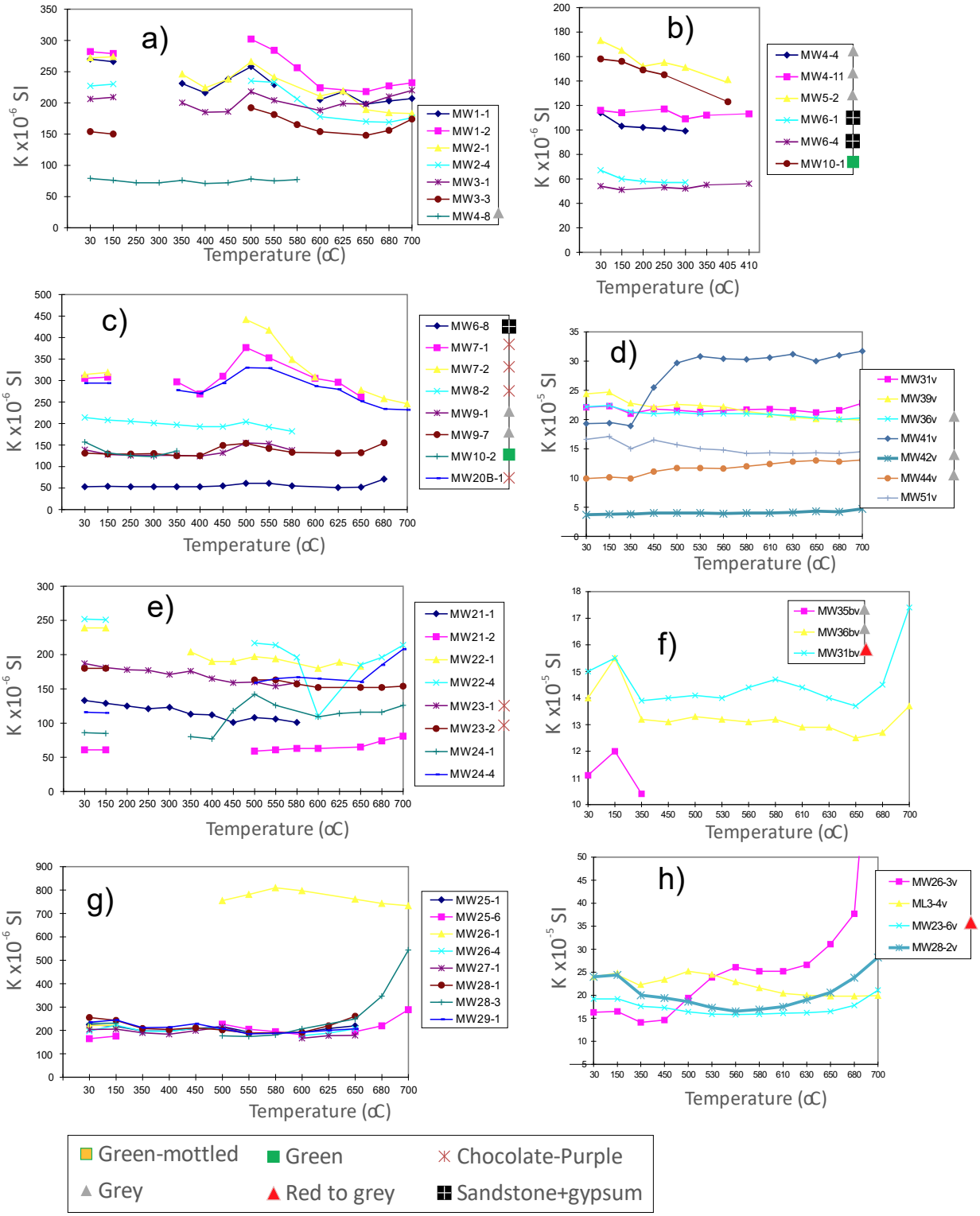

Fig. S2.4. Changes in magnetic susceptibility (K) with heating during thermal demagnetisations steps (measured at room temperature), for the Strangman's Cove (MW) section. The top-most right panel shows K for representative specimens subjected to AF demagnetisation steps. Non red-lithologies marked with symbols as in the key at the bottom (e.g., MW23-6v in h).

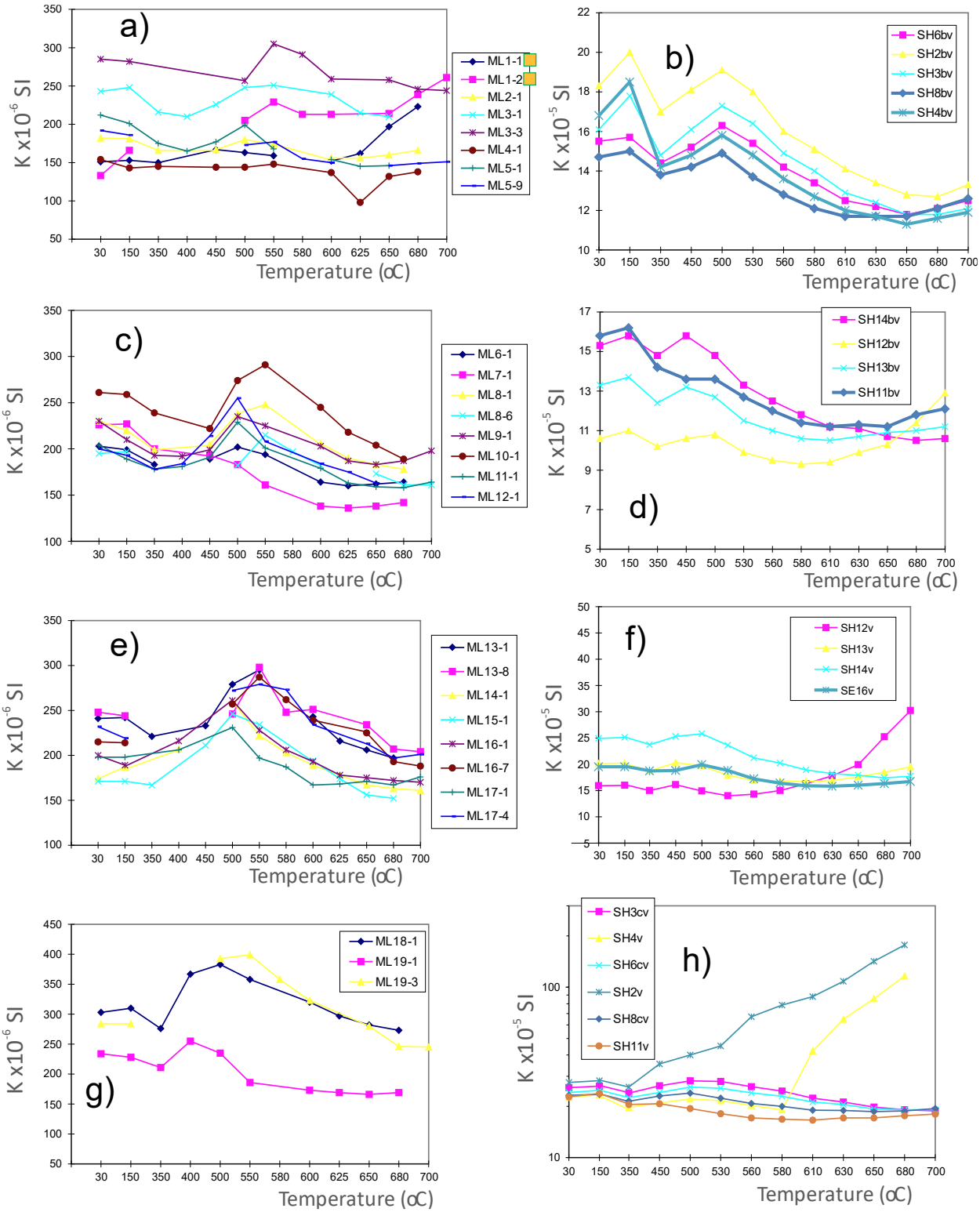

Fig. S2.5. Changes in magnetic susceptibility (K) with heating during thermal demagnetisations steps (measured at room temperature), for the Littlecombe Shoot (ML and SH) section. Note the differing scale used for K for the SH samples. Non red-lithologies marked with symbols as in the key in Fig. S2.4.

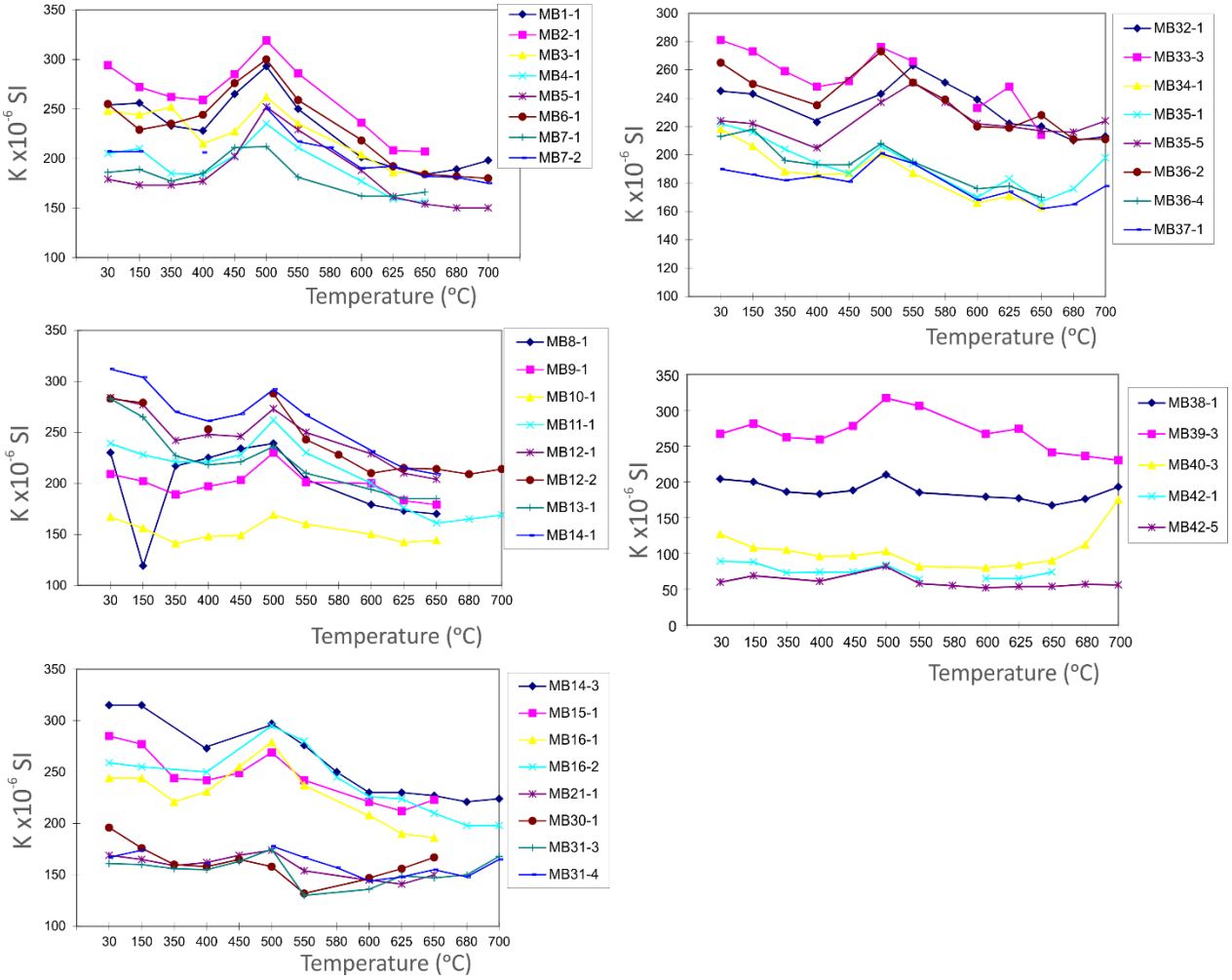

Fig. S2.6. Changes in magnetic susceptibility (K) with heating during thermal demagnetisations steps (measured at room temperature), for the Red Rock to Branscombe Mouth (MB) section.

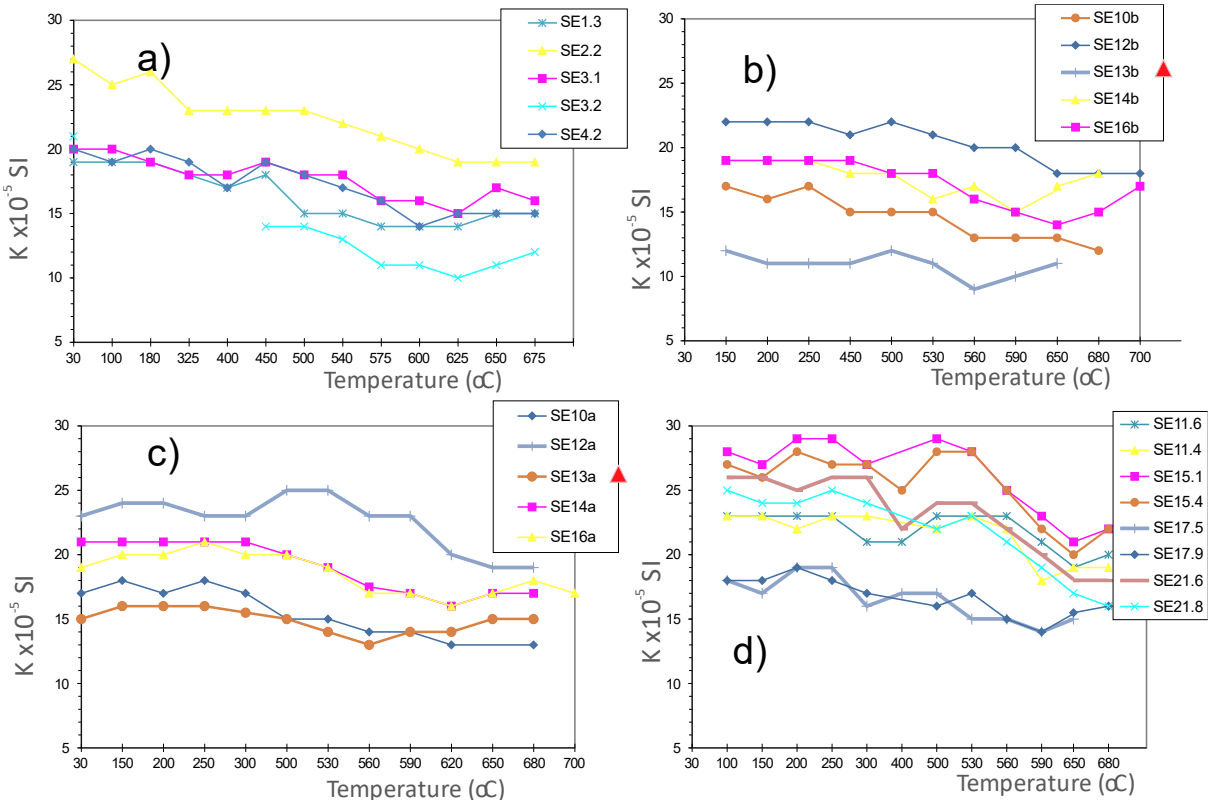

Fig. S2.7. Changes in magnetic susceptibility (K) with heating during thermal demagnetisations steps (measured at room temperature), for the Seaton Cliff section. Non red-lithologies marked with symbols using the key in Fig. S2.4.

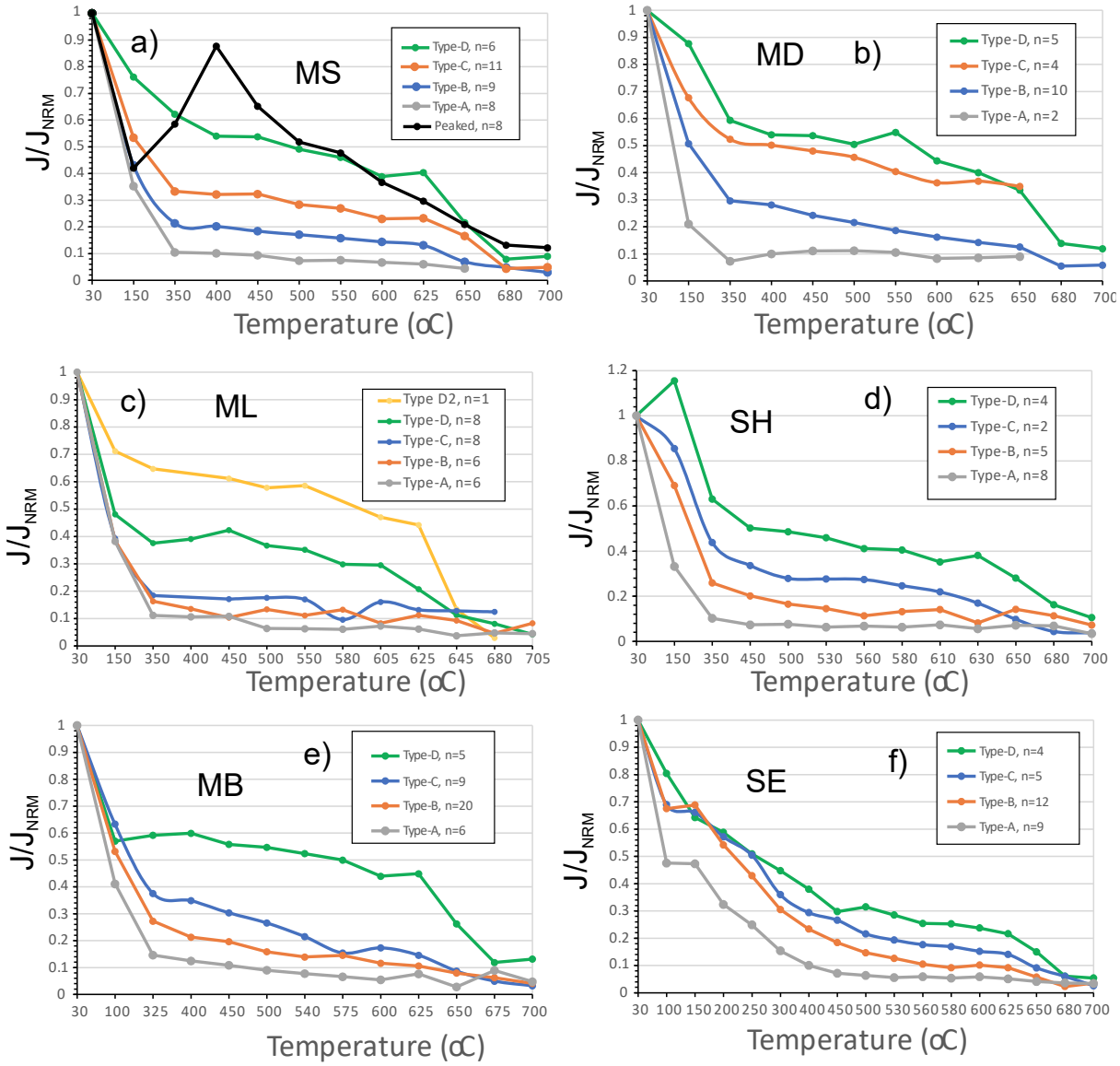

Fig. S2.8. Typical loss of normalised natural remanence (J/J_{NRM}) during demagnetisation for the red lithologies from the various sections (excluding the Strangman's Cove section shown in Fig. S2.9). In each case the curves represent an average of several sets (n= number of specimens) of similar shaped curves, divided into sets based on their J/J_{NRM} intensity between 100 and 500 ºC. These sets are divided into Types A to D (for each section) representing small retention of NRM at 100-500ºC (for Type A behaviour) to larger retention of NRM (for Type-D behaviour). The shapes of the curves are unrelated to the polarity of the specimens, as might be anticipated for remove of a normal polarity LT from reverse and normal polarity ChRM. Those from the MS section have a few specimens (both R and N ChRM) which show a peaked response at around 400ºC.

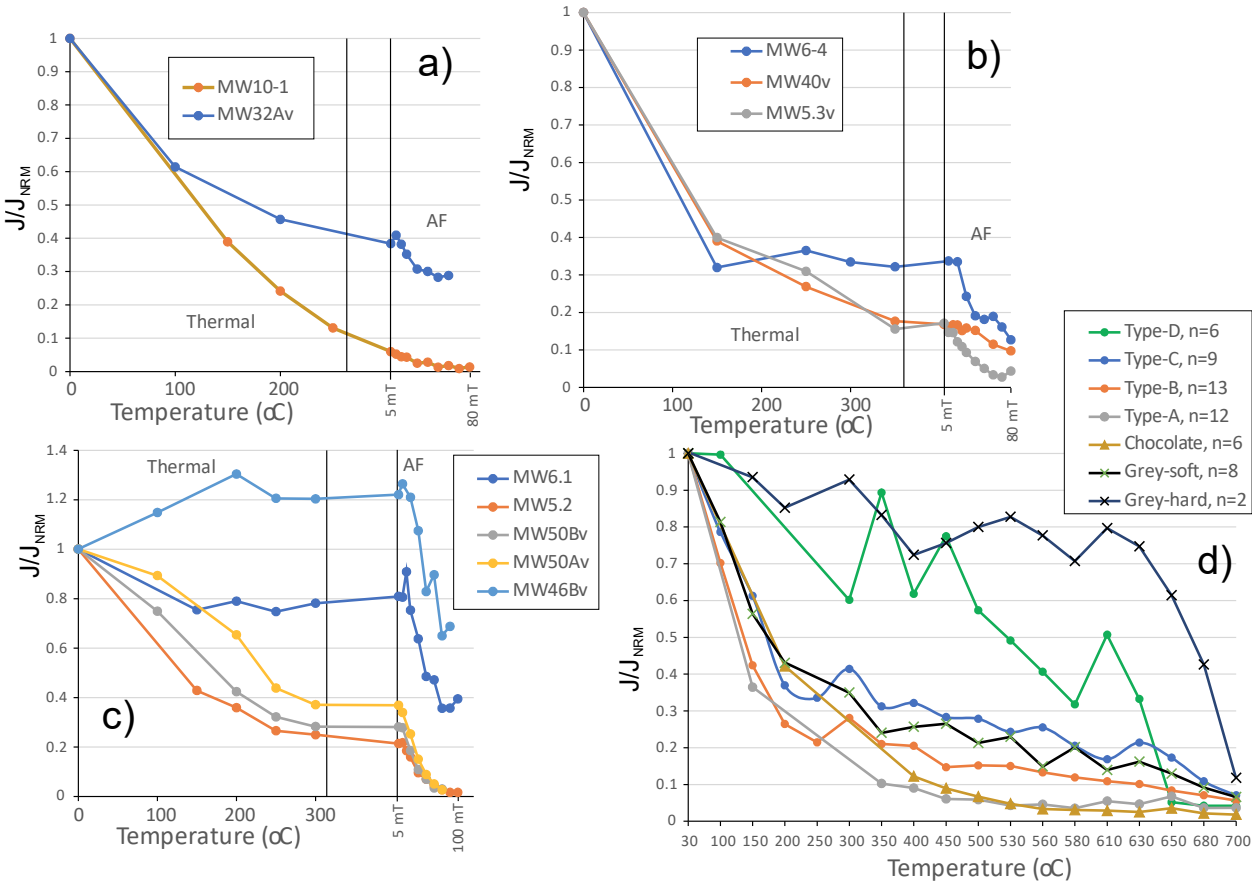

Fig. S2.9. Typical loss of normalised natural remanence (J/J_{NRM}) during demagnetisation for specimens from the Strangman's Cove section (MW code). A), B), C) show representative specimens (labelled with name) subjected to combined thermal and AF demagnetisation. Vertical lines separate the thermal and AF demagnetised steps. D) Those subjected to thermal demagnetisation alone. See Fig. S2.8 for details for red-coloured specimens (Type A to D) in D). In D) those specimens which were not red but grey or pale-chocolate coloured lithologies are also indicated. Grey lithologies either have 'soft' behaviour like the bulk of the red mudstones, or 'hard' behaviour.

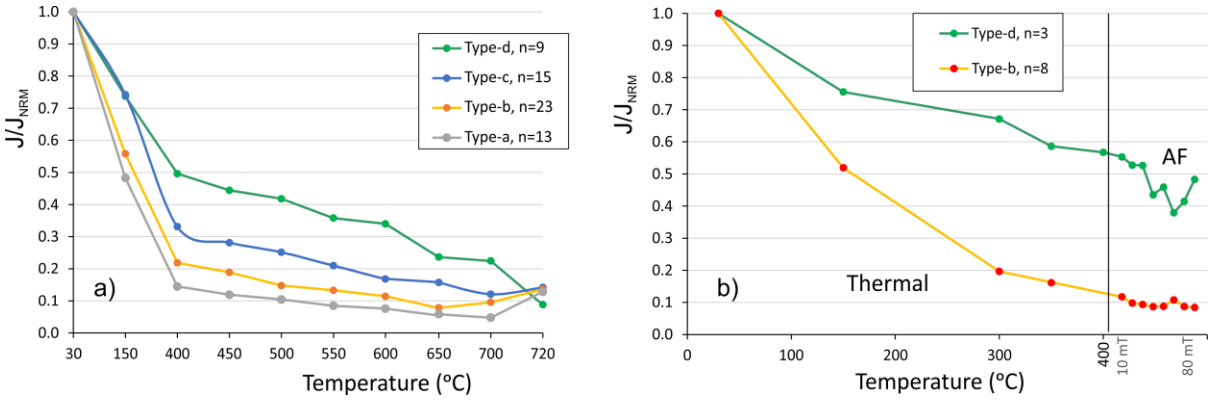

Fig. S2.10. Typical loss of normalised natural remanence (J/J_{NRM}) during demagnetisation for specimens from the Haven Cliff section (HC code). A) Curves representing an average of several sets (n= number of specimens) of similar shaped curves, divided into sets based on their J/J_{NRM} intensity between 100 and 500 ºC. Type-a and Type-b in a) tend to come from the lower part of the section (lower than 13 m below the base of the BAF), and types d and c from above this -13 m level. Intensity decay is much like other samples from the MMG (Figs. S2.8, S2.9). b) Representative average J/J_{NRM} of specimens subjected to combined thermal and AF demagnetisation (all non-red lithologies).

Vertical line separates the thermal and AF demagnetised datasets. Most of the specimens in b) are from the Blue Anchor Fm, with some from the topmost the Haven Cliff Mudstone Mb. Tumbling AF demagnetisation has a minor effect in changing intensity, but a bigger effect in changing the directional data.

S3. Low temperature (LT) component, unblocking ranges of components, demagnetisation diagrams and mean directions.

The LT component is fairly scattered and shows the best grouped behaviour for the SH, ML and MW sections, with least coherence in the MS, MD, HC sections (Fig. S3.1). As Creer (1957, 1959) demonstrated the lower MMG rocks can acquire substantial short-term viscous magnetisations, as well as longer term magnetisations, likely acquired during the Brunhes. Hence, a short-term viscous component has probably contributed to some of the evident scatter in the LT component. Nevertheless, the overall grouping near the present-day geomagnetic field (Fig. S3.1e) confirms the conclusions of Creer (1957) for this low stability component throughout the MMG. The LT component dominates the total NRM magnetisation in many samples accounting for around 50% to 90% of the starting NRM (Figs. S2.8, S2.9, S2.10), typically ranging up to around the ca. 350-400 ^{o}C demagnetisation steps (Fig. S3.3a,c, S3.4a, S3.5a,c,e,g).

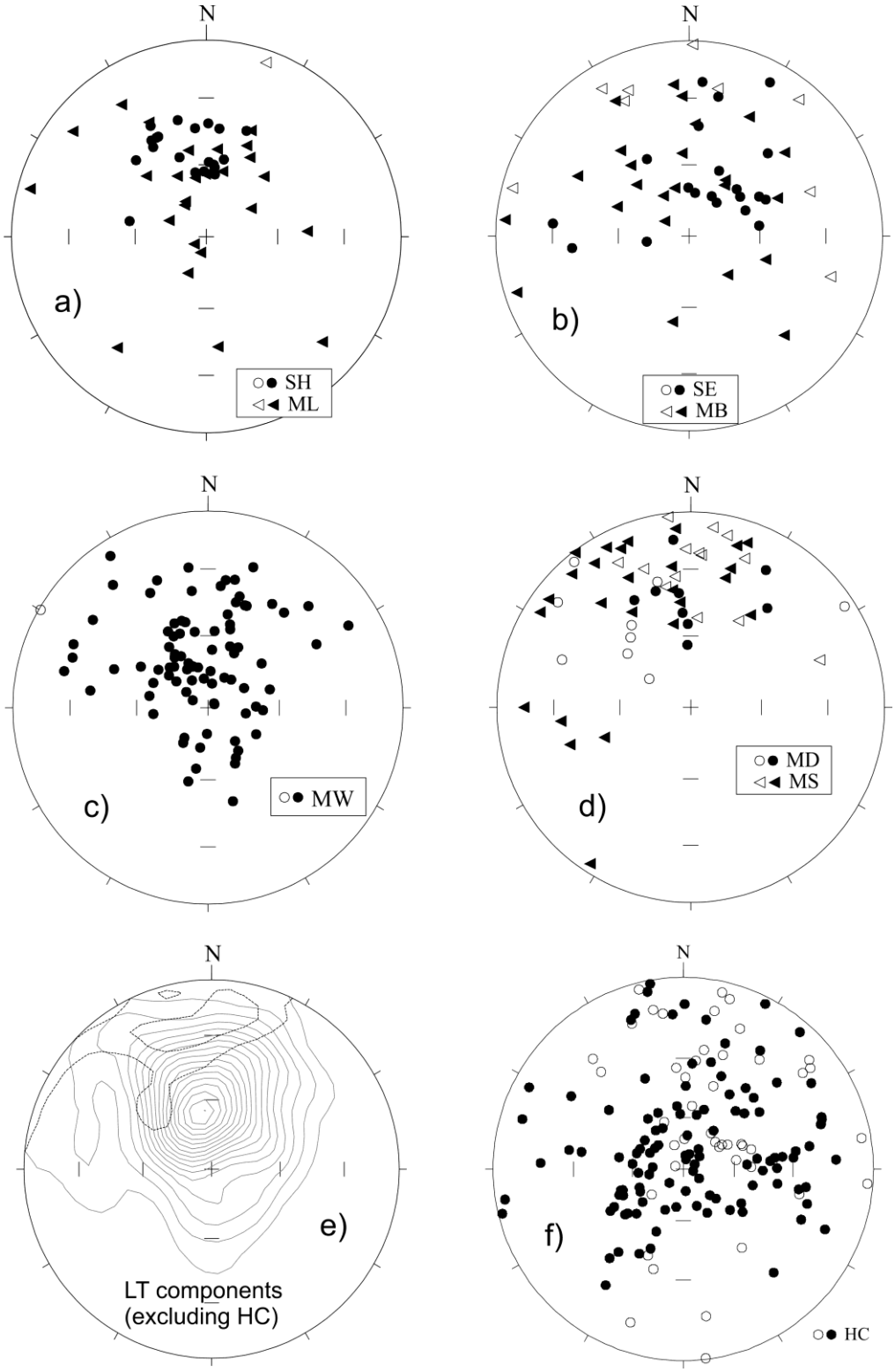

Fig. S3.1. The directional information from the low temperature component (LT) divided into divisions based on the sections (a) to d); all in geographic coordinates). See Table 2 in main text for sample codes indicating sections. e) The LT component directions contoured on the lower (solid contours) and upper hemisphere (dotted contoured), using the Kamb method and inverse area squared smoothing (binomial sigma value=3, grid size=30, contour interval=2; Vollmer 1995).

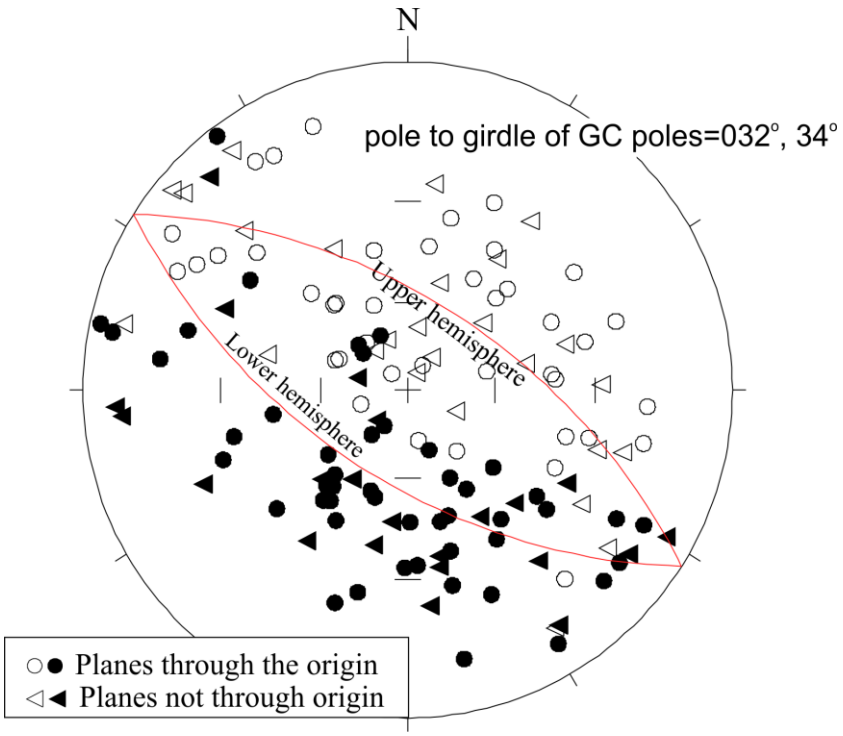

Fig. S3.2. The poles to fitted great circle (GC) planes of the ChRM directions for all the T-class specimens (in stratigraphic coordinates). The great circle shown is that orthogonal to the Fisher mean direction of all of the MMG specimens with S-class directions. Shown is the pole to the girdle defined by the GC poles (T-class specimens only), which is near to the mean direction based on the s-class specimens (main text Table 3).

The line-fit ChRM component shows a range of unblocking temperatures typically at 500ºC and above, but sometimes below this (Figs. S3.3b,d; S3.4b; S3.5b,d,f,h, S3.6b).

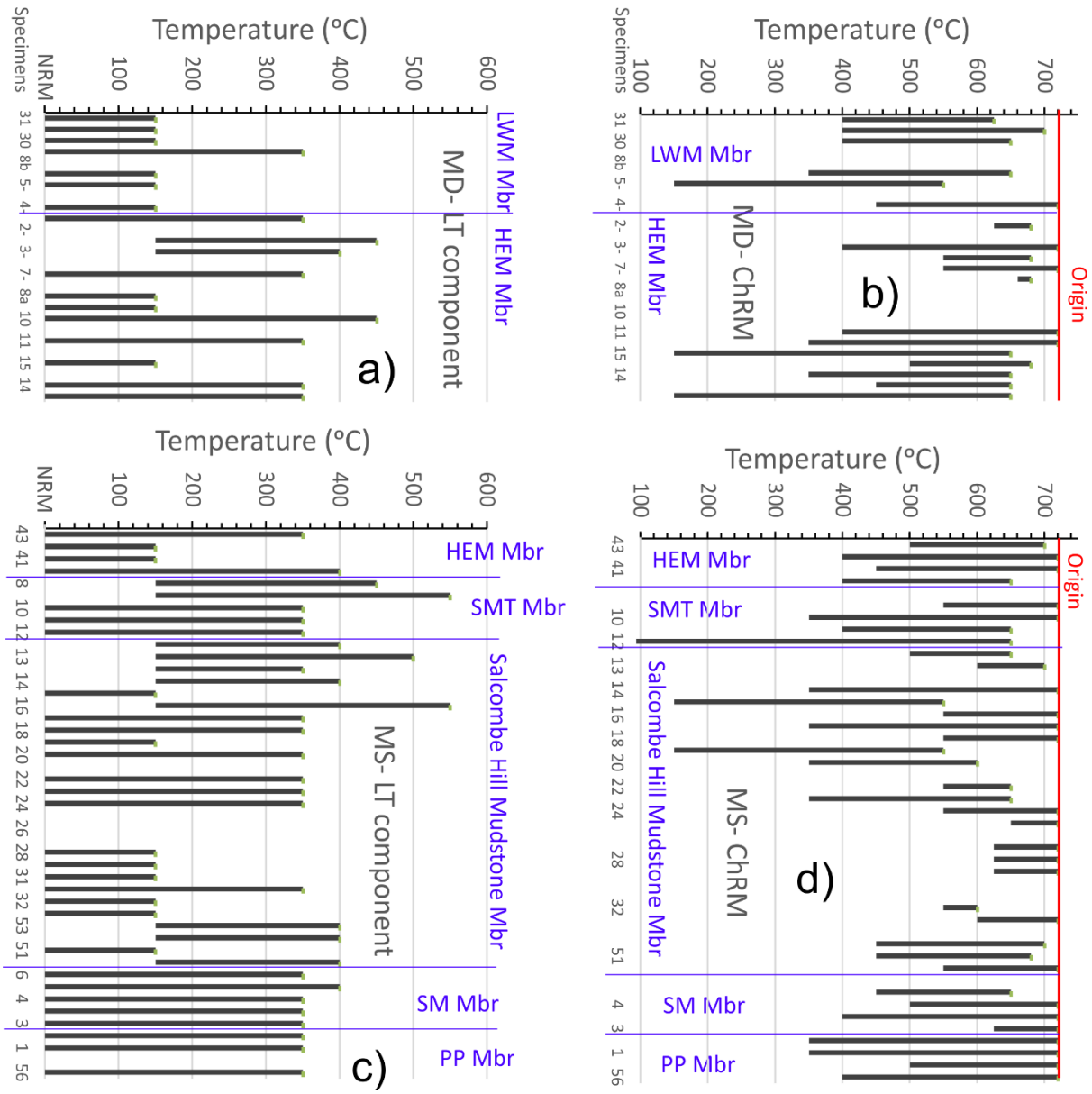

Fig. S3.3. The temperature ranges of the LT components (a and c) and the ChRM components (b and d) for samples from the Sid Outfall to Salcombe Mouth section (MS codes, c) and d)) and Salcombe Mouth to Hook Ebb (MD, a), b) section. The Y-axis shows specimens (only some sample number shown) in stratigraphic order from base to top of the section in each case. The member boundaries (in blue) are shown at the appropriate sample position. In b) and d) intersection of the range with the red vertical line indicates the ChRM component includes the vector origin in the principal component analysis. PP= Pennington Point, SM=Sid Mudstone Mb, SMT= Salcombe Mouth Mudstone Mb, HEM= Hook Ebb Mudstone Mb. LWM= Little Weston Mudstone Mb. See Figs. S1.1 to S1.7 for sample location positions on the section logs.

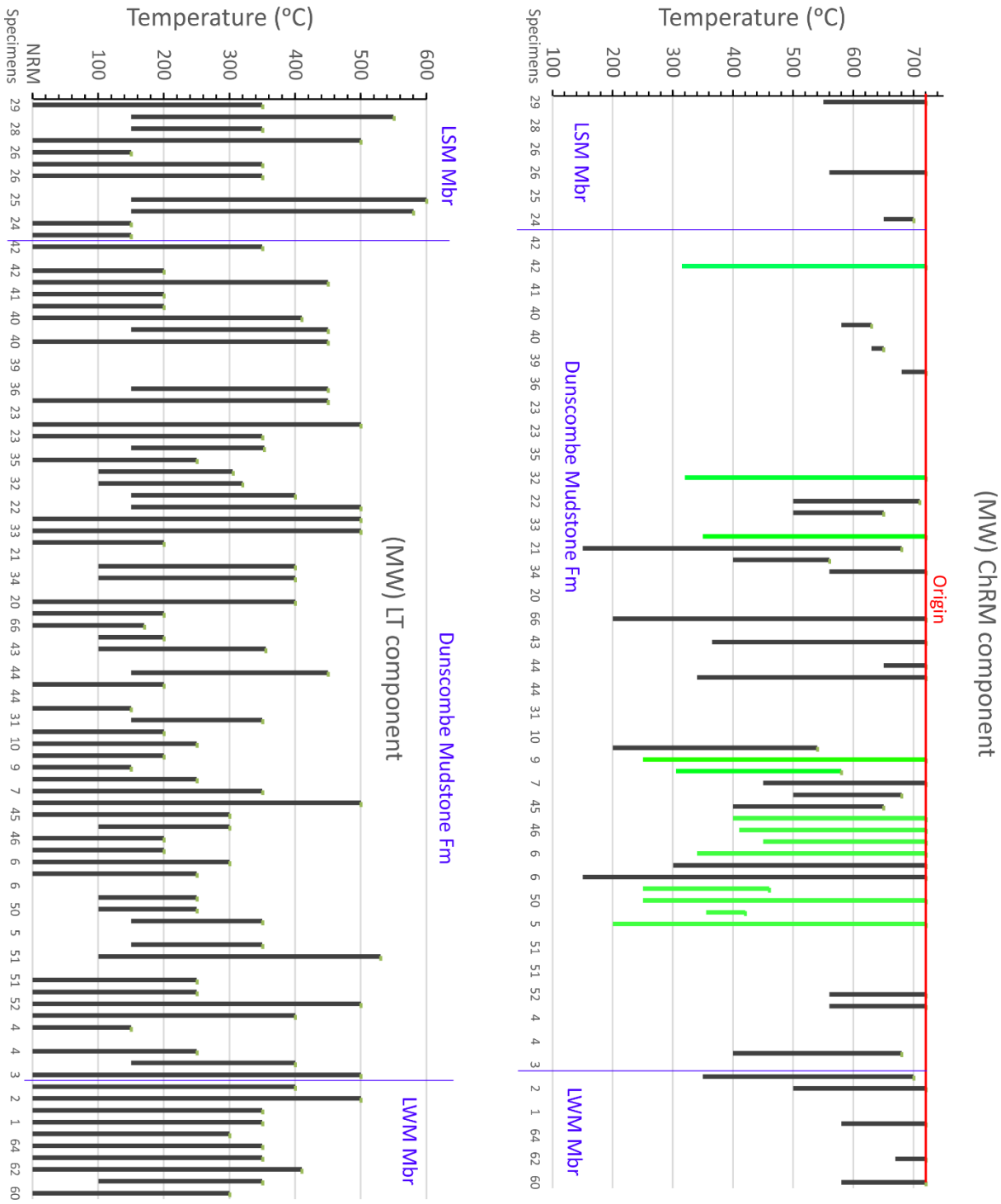

Fig. S3.4. The temperature ranges of the LT components (left) and the ChRM components (right) for the Hook Ebb-Strangman's Cove section (MW). LSM=Littlecombe Shoot Mudstone Mb. The green ranges are those which include AF demagnetisation steps, following initial thermal demagnetisation (to between 200-400 ºC). See Fig. S3.3 for other details.

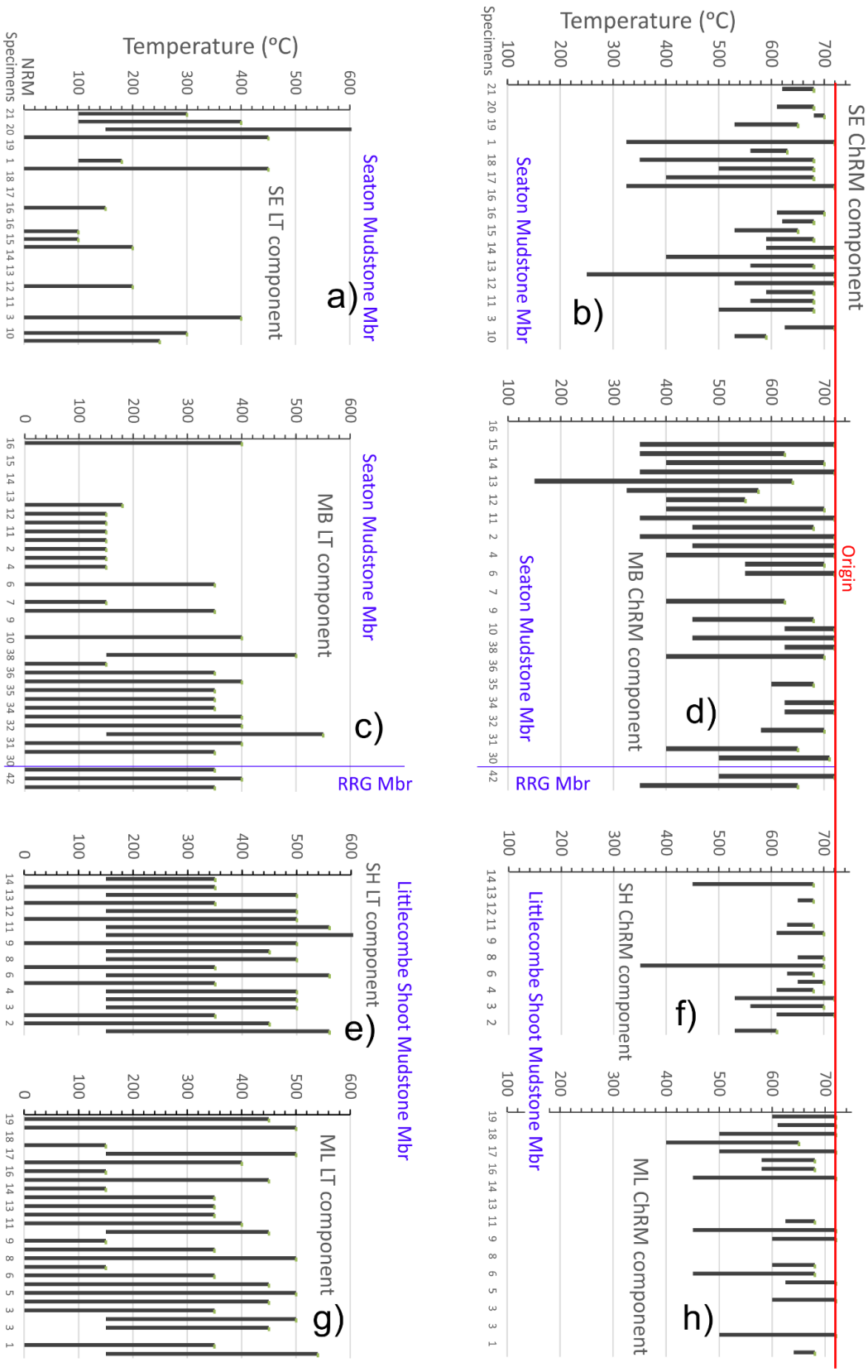

Fig. S3.5. The temperature ranges of the LT components (a, c, e, g) and the ChRM components (b, d, f, h) for the Littlecombe Shoot west section (ML), Littlecombe Shoot east (SH), Red Rock-Branscombe Mouth section (MB) and Seaton Cliffs (SE) sections. RRG= Red Rock Gypsum Mb. See Fig. S3.3 for other details.

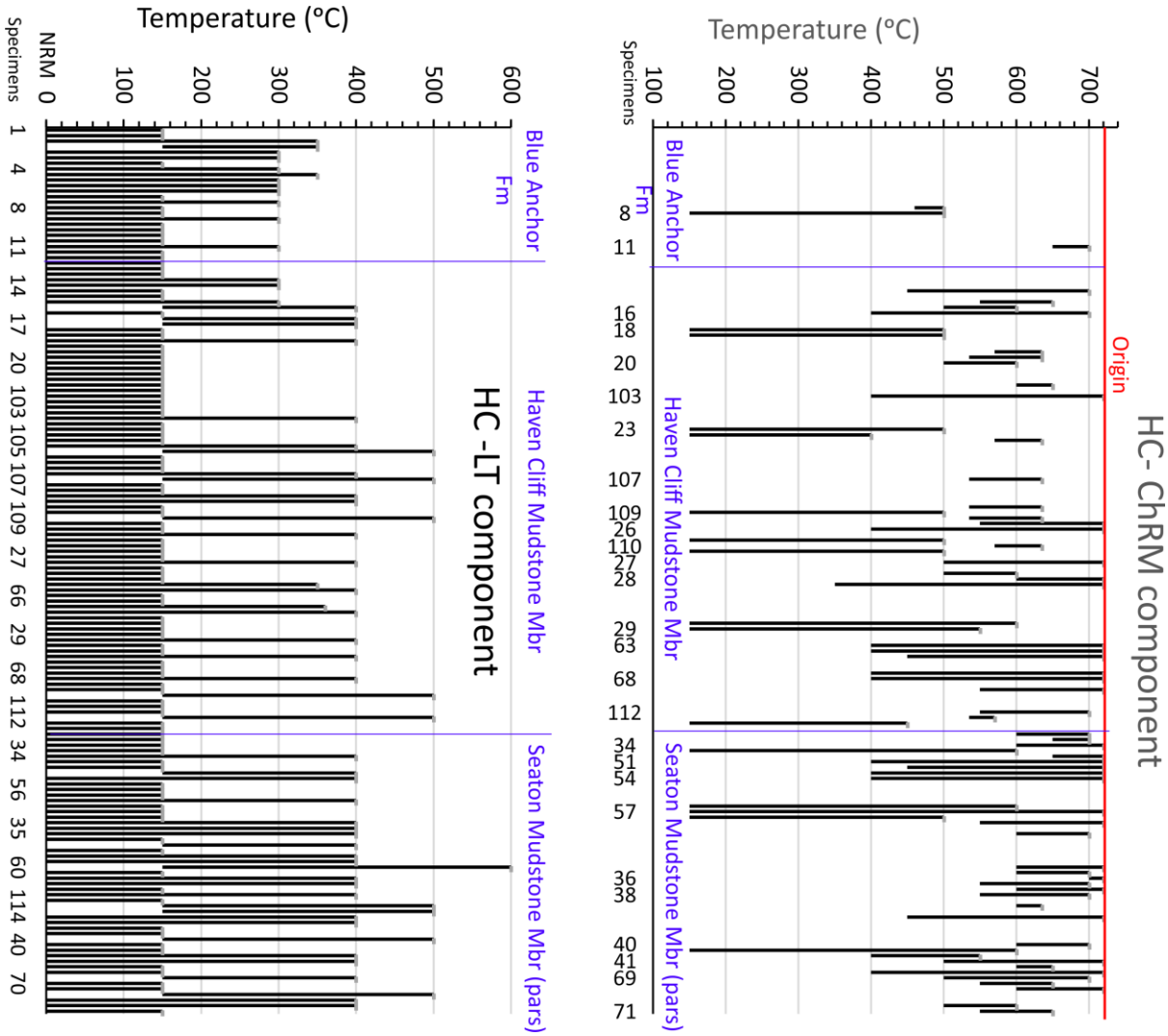

Fig. S3.6. The temperature ranges of the LT components (a) and the ChRM components (b) for the Haven Cliff section (HC). See Fig. S3.3 for other details.

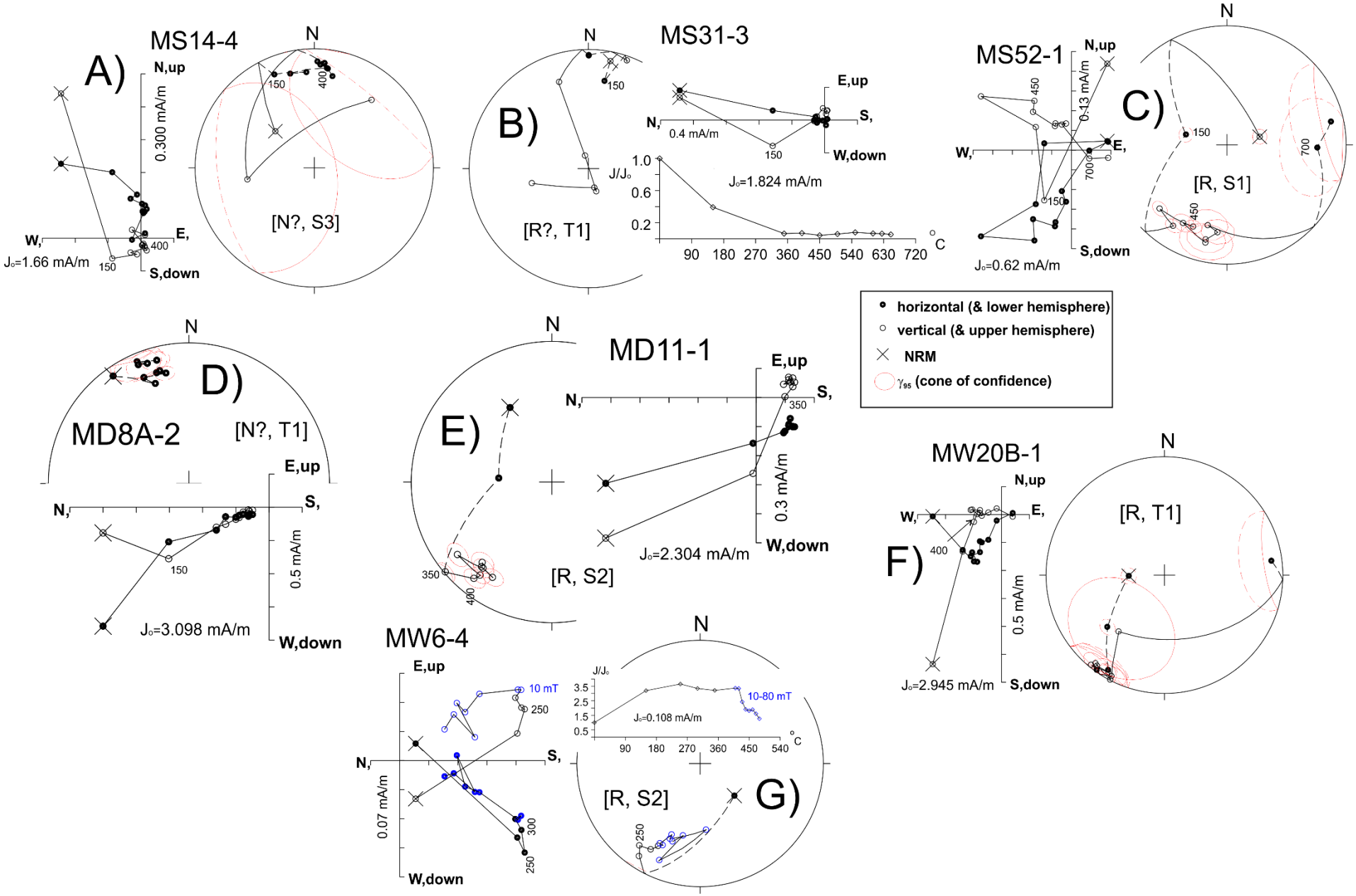
A)
MS14-4
N,up
0.300 mA/m
W,
E,
S,down
J₀=1.66 mA/m
150
400
N
[N?, S3]
B)
MS31-3
[R?, T1]
E,up
N,
S,
W,down
0.4 mA/m
J/J₀
1.0
0.6
0.2
J₀=1.824 mA/m
90 180 270 360 450 540 630 720
°C
MS52-1
N,up
0.13 mA/m
W,
E,
S,down
J₀=0.62 mA/m
450
700
C)
[R, S1]
horizontal (& lower hemisphere)
vertical (& upper hemisphere)
NRM
γ95 (cone of confidence)
D)
MD8A-2
[N?, T1]
E,up
N,
S,
W,down
0.5 mA/m
J₀=3.098 mA/m
E)
MD11-1
E,up
N,
S,
W,down
0.3 mA/m
J₀=2.304 mA/m
350
400
[R, S2]
MW20B-1
N,up
W,
E,
S,down
0.5 mA/m
J₀=2.945 mA/m
F)
[R, T1]
MW6-4
E,up
N,
S,
W,down
0.07 mA/m
10 mT
250
300
J/J₀
3.5
2.5
1.5
0.5
J₀=0.108 mA/m
10-80 mT
90 180 270 360 450 540
°C
[R, S2]
G)

Fig. S3.7 (previous page). Representative demagnetisation plots for the Sidmouth Mudstone and Dunscombe Mudstone formations. Showing Zijderveld plot (scale indicates that between each tick in mA/m) and stereonets of directions. Some have demagnetisation intensity (J/J_0- temperature, ^oC) plots. J_0= initial undemagnetised NRM. Stereonets display the cone of confidence values ($\gamma 95$) of Briden & Arthur (1981) from the repeat measurements (if > 5^o) of each step (some of these have been removed in some plots for greater clarity). Points marked in blue are AF demagnetisation steps, all others are thermal demagnetisation steps. Selected steps are labelled corresponding to the boundaries between the inferred extracted components and great circle planes. The inferred polarity classification and demagnetisation behaviour is indicated in the [..] brackets. Most of these are red mudstone samples, but other lithologies are indicated in the descriptions. All directional plots are in stratigraphic coordinates. Fitted components and great circle directions indicated in {..}, with LT components in geographic coordinates and others in stratigraphic coordinates (plane directions are poles to the GC plane). The third value of the ChRM or pole values in {..} is the VGP latitude value VGP_R. Heights relate to position in the subsections (shown in figures in main text).

A) MS14.4 (73.23m), normal polarity (N?) LT-component is 150-400^{o}C {318°, 9°} and ChRM is 400^{o}C-origin {000°, 21°, 60°}. B) MS31-3 (35.11 m), reverse polarity (R?) with LT component 150-400^{o}C {012°, -11°} and a plane fitted between the NRM and origin defining the magnetisation direction {281°, 04°, -73°}, shown by the trend southwards in the last four steps. C) MS52.1 (22.48 m), reverse polarity (R), with LT component NRM-150^{o}C {033°, 43°} and well-defined ChRM component 450-700^{o}C {217°, -24°, -84°}. D) MD8A-2 (36.78 m), normal polarity (N?), with LT component NRM-150°C {308°,-14°}, and a plane fitted between the NRM and origin defining the magnetisation direction {044°, -47°, 81°}. E) MD11-1 (20.66 m) with LT component NRM-350°C {343°, 38°} and ChRM component 400^{o}C to origin {221°, -17°, -78°}. F) MW20B-1, chocolate brown to dark red mudstone (27.32 m), with LT component NRM-400°C {316°, 67°}, and a plane fitted between the NRM and origin defining the magnetisation direction {303°, -8°, -86°}. G) MW6-4, white very fine-grained sandstone (9.28 m) with LT component NRM-250^{o}C {045°, 28°} and ChRM defined by the steps from 300^{o}C to the origin, including the AF steps from 10 to 80 mT {210°, -42°, -85°}.

Fig S3.8 (following page). Representative demagnetisation plots for the Dunscombe Mudstone Fm and Littlecombe Shoot Mudstone Mbr. See preamble to Fig.S3.7 for plot and labelling details.

A) MW26-3v (40.4 m), normal polarity (N) with LT component NRM-350°C {016°, 41°}, and ChRM component 560°C to origin {003°, 32°, 62°}. B) MW65_2d (3.87 m below base DMF), normal polarity (N??) with LT component NRM-300°C {099°, 74°}and ChRM component 580°C to origin {067°, 35°, 58°}. The intermediate is a composite negative inclination component in the NW. C) ML19-1 (47.39 m), normal polarity (N), with a LT component NRM -450°C {349°, 65°}, and a weak ChRM component 600°C to origin {064°, 13°, 59°}. D) ML18-1 (26.08m), reverse polarity (R) with a ChRM component 500°C to origin {207°,-19°,-82°}. E) ML2-1 (5.09 m), reverse polarity (R) with LT component NRM-150°C {23°, 41°} and ChRM component 500°C to origin (last two steps large $\gamma 95$) {202°, -31°, -79°}. F) SH6bv (11.16 m), reverse polarity with LT component 150-560°C {329°, 46°}, and ChRM component 630-680°C {224°, -25°, -79°}. G) SH11bv (20.83 m), normal polarity with LT component 150-560°C {002°, 59°}and ChRM component 630-680°C {039°, 19°, 82°}.

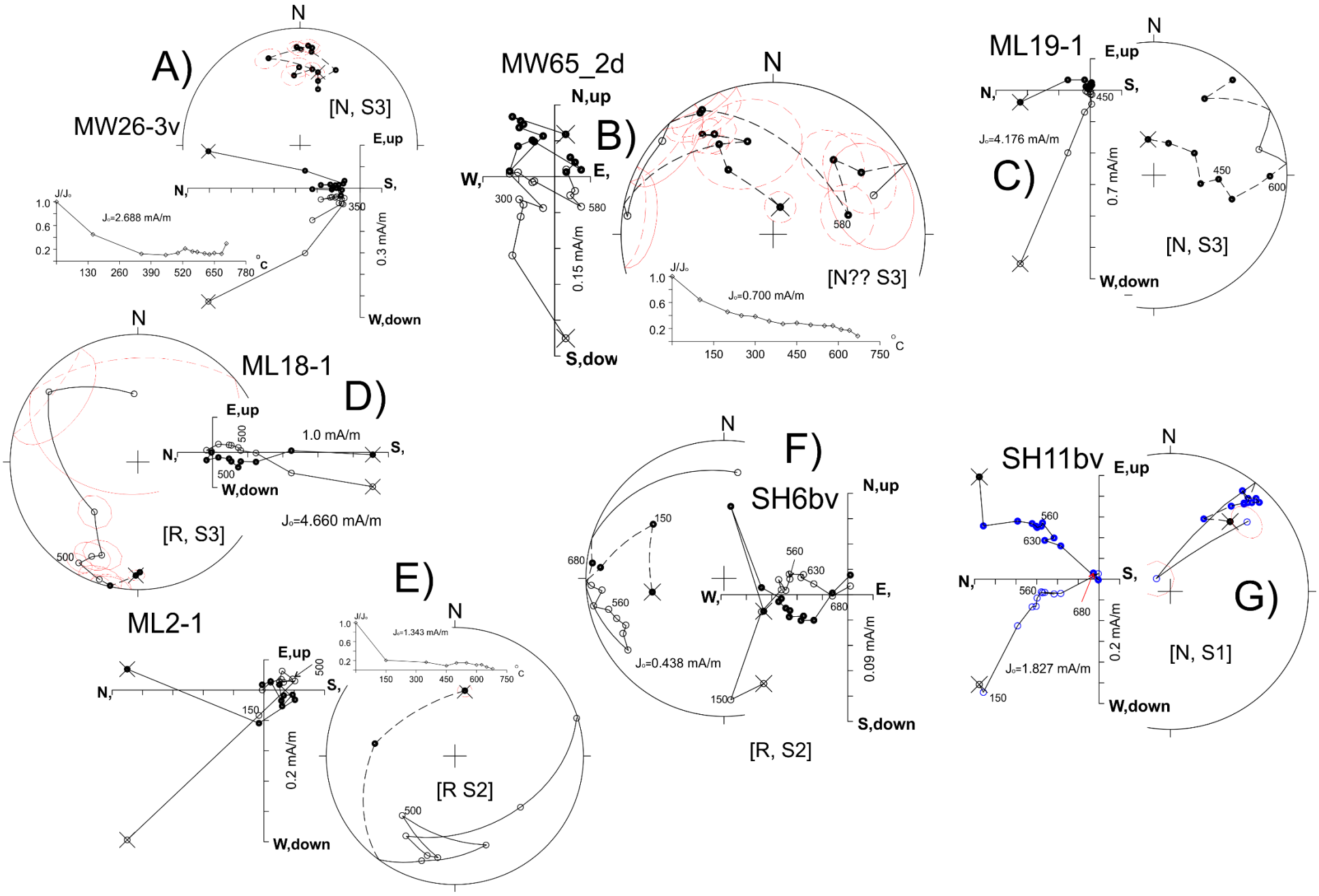
A)
MW26-3v
[N, S3]
N
E,up
N,
S,
W,down
J/J₀
J₀=2.688 mA/m
0.3 mA/m
B)
MW65_2d
N,up
W,
E,
S,dow
0.15 mA/m
[N?? S3]
J₀=0.700 mA/m
C)
ML19-1
N,
S,
E,up
W,down
J₀=4.176 mA/m
0.7 mA/m
[N, S3]
D)
ML18-1
E,up
N,
S,
W,down
1.0 mA/m
J₀=4.660 mA/m
[R, S3]
E)
ML2-1
E,up
N,
S,
W,down
0.2 mA/m
J₀=1.343 mA/m
[R S2]
F)
SH6bv
N,up
W,
E,
S,down
J₀=0.438 mA/m
0.09 mA/m
[R, S2]
SH11bv
E,up
N,
S,
W,down
J₀=1.827 mA/m
0.2 mA/m
[N, S1]
G)

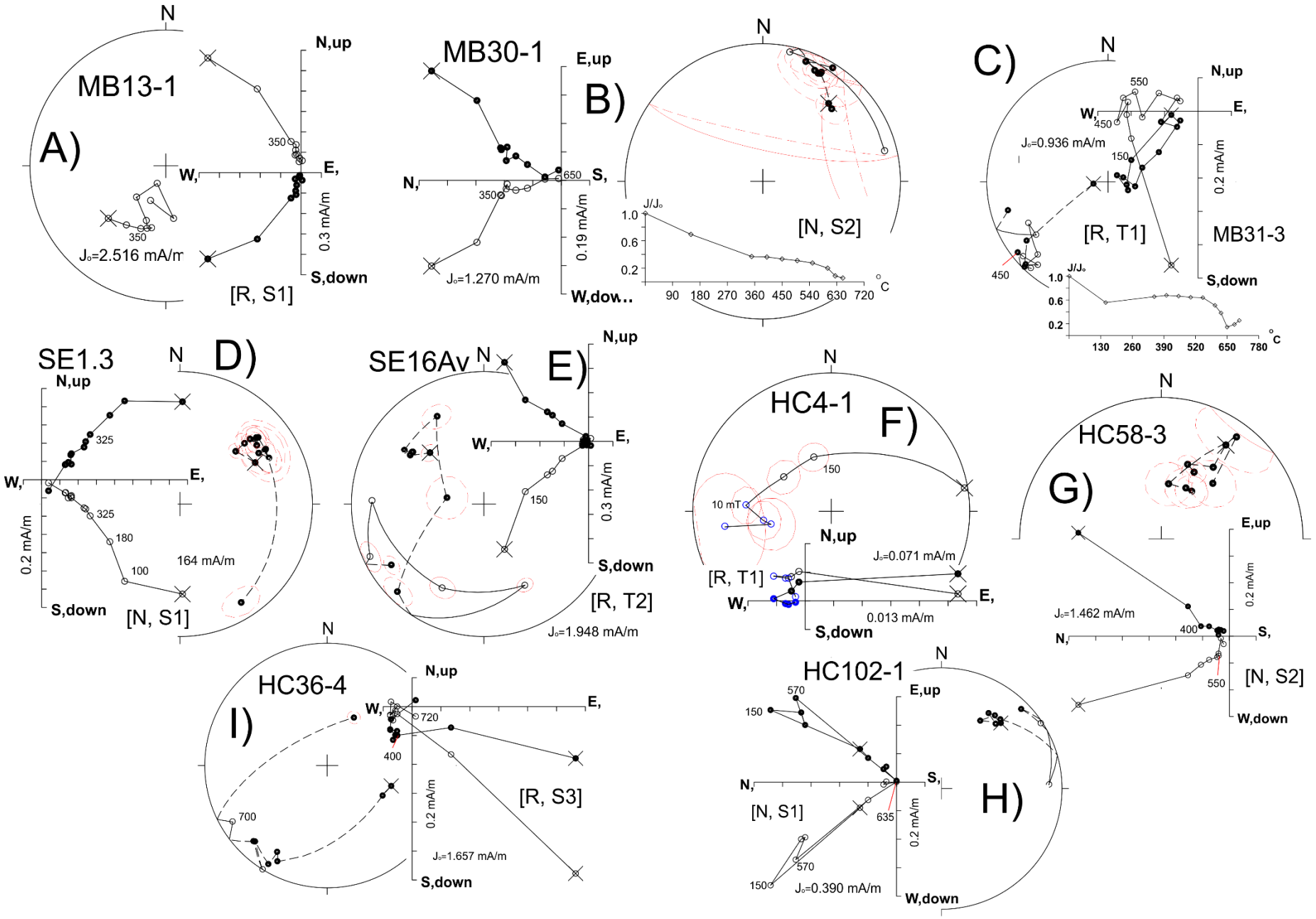
A)
MB13-1
N
N,up
E,
W,
S,down
0.3 mA/m
350
350
J₀=2.516 mA/m
[R, S1]
B)
MB30-1
N
E,up
N,
S,
W,down
650
350
0.19 mA/m
J₀=1.270 mA/m
J/J₀
1.0
0.6
0.2
90 180 270 360 450 540 630 720 °C
[N, S2]
C)
N
N,up
E,
W,
550
450
150
J₀=0.936 mA/m
0.2 mA/m
[R, T1]
MB31-3
S,down
450
J/J₀
1.0
0.6
0.2
130 260 390 520 650 780 °C
D)
SE1.3
N
N,up
W,
E,
325
325
180
100
164 mA/m
0.2 mA/m
S,down
[N, S1]
E)
SE16Av
N
N,up
W,
E,
150
0.3 mA/m
S,down
[R, T2]
J₀=1.948 mA/m
F)
HC4-1
N
150
10 mT
N,up
J₀=0.071 mA/m
[R, T1]
W,
E,
0.013 mA/m
S,down
G)
HC58-3
N
E,up
0.2 mA/m
J₀=1.462 mA/m
N,
400
S,
550
[N, S2]
W,down
I)
HC36-4
N
N,up
W,
E,
720
400
700
0.2 mA/m
[R, S3]
J₀=1.657 mA/m
S,down
H)
HC102-1
N
570
E,up
150
N,
S,
[N, S1]
635
570
150
0.2 mA/m
J₀=0.390 mA/m
W,down

Fig. S3.9 (previous page). Representative demagnetisation plots for the Seaton Mudstone and Haven Cliff Mudstone members and the Blue Anchor Fm. see preamble to Fig.S3.7 for plot and labelling details.

A) MB13-1 (47.59 m), reverse polarity (R) with ChRM component 350°C to origin {203°,-45°, -75°}. B) MB30-1 (0.29 m), normal polarity (N) with LT component NRM to 350°C {049°, 35°}and ChRM component 400-650°C {025°, 13°, 78°}. C) MB31-3 (2.08 m) reverse polarity (R) with LT component 150-550°C {033°, 62°} and a plane fitted between the 450°C and the origin {310°, -3°, -85°} defining the magnetisation direction. D) SE1.3 (15.47 m), normal polarity (N) with a weak/doubtful LT component 100-180°C {046°, 62°}, and strong ChRM between 325°C and the origin {053°, 27°, 71°}. E) SE16Av (9.69 m), with LT component NRM-150°C {331°, 53°} and a weak reverse polarity component defined by a great circle trend from NRM to origin {149°, 51°, -83°}. The strong intermediate component is a composite with positive inclination directed to the NW. F) HC4-1, grey-green mudstone (11.35 m, Blue Anchor Fm), reverse polarity, with LT component NRM-150°C {087°, 12°} and great circle trend from 10 mT to the origin {199°, 21°, -59°}. G) HC58.3, red-grey mottled mudstone (-25.5 m), normal polarity, with a strong LT component NRM-400°C {33, 17} and a ChRM 500°C to the origin {027°, 53°, 72°}. H) HC102-1 (-6.5 m) , normal polarity, LT component NRM-150°C (202°, -38°}, and a ChRM 570-635°C {040°, 29°, 86°}. I) HC36-4 (-27.7 m), reverse polarity, with a strong LT component NRM-400°C {086°, 53°} and a weak very high temperature ChRM, 700-720°C {232°, -25°, -76°}. The intermediate component is inferred as composite, shallow and directed to the SW.

Type/ section/ Unit	Dec(°)	Inc(°)	K/α_{95}(°)	Ns/Nl/Np	Reversal Test	G_O/G_C(°)	Plat/ Plong(°)	Dp/Dm (°)	A95 (min, max), %VGP_{45}
Salcombe Cliff (MS)									
Line fits$	29.8.0	25.9	20.5/5.4	35/37/0	Rc	5/11.3*	45.8/132.9	3.2/5.8	5.2 (2.9, 8.7), 0
GC means+	28.8	25.3	11.1/4.7	40/37/7	Rc	2.8/15.4	45.9/134.4	2.7/5.1	4.5 (2.7,8.0), 0
Dunscombe Cliff (MD)									
Line fits$	29.2	29.0	29.2/6.5	15/18/0	Rc	4.9/15*	47.7/132.5	3.9/2.7	6.9 (4.1, 14.9), 0
GC means+	28.0	30.0	16.4/5.3	18/18/6	Ro	3.7/21	48.8/133.6	3.3/5.9	6.2 (3.8, 13.3), 0
Strangman's Cove (MW)									
Line fits$	33.8	35.5	20.6/4.9	28/43/0	Rb	4.3/7.8*	49.1/123.7	3.3/5.7	5.8 (3.2, 10.0), 0
GC means+	34.3	37.2	11.4/3.5	44/43/33	Rb	4.4/8.1*	49.8/122.1	2.4/4.1	3.8 (2.6, 7.6), 3.6
Littlecombe Shoot west (ML)									
Line fits$	33.9	26.7	16.8/9.0	14/17/0	Ro	7.7/32	44.3/127.7	5.3/9.8	8.0 (4.2,15.6), 0
GC mean+	33.7	26.9	10.7/6.8	18/17/6	Ro	7.3/33	44.5/127.9	4.0/7.4	6.6 (3.8, 13.3), 10.7
Littlecombe Shoot east (SH)									
Line fits$	33.9	27.1	20.8/9.3	8/13/0	Ro	6.9/27	44.5/127.6	5.5/10/1	11.3 (5.2, 22.1), 0
GC mean+	31.8	32.8	10.6/7.3	10/13/6	Rc	9.5/17*	48.6/127.6	4.7/8.3	8.8 (4.8, 19.2), 0
Branscombe (MB)									
Line fits$	30.7	28.5	21.9/5.9	25/29/0	Rc	10.3/12.0*	46.8/130.9	3.6/6.5	6.0 (3.3, 10.8), 0
GC mean+	31.5	26.8	12.0/4.8	28/29/7	Rc	10.5/10.7*	45.5/130.6	2.8/5.2	5.2 (3.2, 10.0), 0
Seaton (SE)									
Line fits$	37.2	29.8	24.8/6.1	16/24/0	Rc	7.6/12.9*	44.3/122.7	3.7/6.8	5.6 (4.0, 14.3), 0
GC mean+	38.4	31.1	9.1/6.4	16/24/5	Rc	7.1/29	44.3/120.7	4.0/7.2	5.2 (4.0, 14.3), 0
Haven Cliff (HC)									
Line fits$	39.6	35.6	24.0/3.4	51/74/0	R-	8.3/8.0	44.0/126.6	2.3/3.9	3.5 (2.5, 6.9), 1.4
GC mean+	37.7	34.2	10.1/2.6	74/74/63	R-	12.4/9.9	44.1/129.4	1.7/3.0	3.0 (2.1, 5.4), 2.1
Formation Means:									
Branscombe Mudstone$,1	33.5	28.4	21.4/3.4	66/86/0	Rb	3.5/6.8	45.4/127.5	2.0/3.7	3.4 (2.2, 5.9), 0
Dunscombe Mudstone$	33.0	35.5	20.7/5.6	20/33/0	Rc	4.9/11.6	49.5/124.7	3.7/6.5	6.2 (3.6, 12.4), 0
Sidmouth Mudstone$	30.9	28.1	22.0/4.1	51/58/0	Rc	2.8/13.1	46.5/130.7	2.5/4.5	4.3 (2.5, 6.9), 0
Pennington Point Mb$	18.7	27.7	11.7/13.3	10/12/0	-	-	51.0/147.3	7.9/14.5	+10.8 (4.8, 19.2), -

Table S3.1. Directional means (with tectonic correction), reversal tests and VGP poles. +=great circle combined mean using method of McFadden & McElhinny (1988). $=conventional Fisher mean. 1= not including Haven Cliff data. Ns=number of levels (sites), Nl=number of specimens used with fitted

lines, and Np =number of specimens with great circle planes used in the determining the mean direction. α_{95}, Fisher 95% cone of confidence. k, Fisher precision parameter. G_O is the angular separation between the inverted reverse and normal directions, and Gc is the critical value for the reversal test. In the reversal test the Go/Gc values flagged with * indicate common K values, others not flagged have statistically different K-values for reverse and normal populations, in which case a simulation reversal test was performed. Plat and Plong are the latitude and longitude of the mean virtual geomagnetic pole[1]. For GC means reverse and normal means averaged using Fisher pooled mean (based on dispersion; Fisher et al. 1993), for line-fits by inverting the reverse set. Pennington Point and Sidmouth Mudstone means use data also from Hounslow & McIntosh (2003). A95 (min, max) = Fisher 95% confidence interval for VGP-based site mean (N_s sites), and $A95_{min}$ and $A95_{max}$ threshold values of Deenen et al. (2011). $\%VGP_{45}$= percent of samples yielding VGP latitude < |45|, as a reflection of the match to modern geomagnetic field models and palaeomagnetic data in which $\%VGP_{45}$ is a 3-4% (Cromwell et al. 2018). $\%VGP_{45}$ applies to all the section. Statistics determined with Pmagtool v.5 (Hounslow 2006).

Section S4: Virtual geomagnetic pole (VGP) data for the European mid and late Triassic

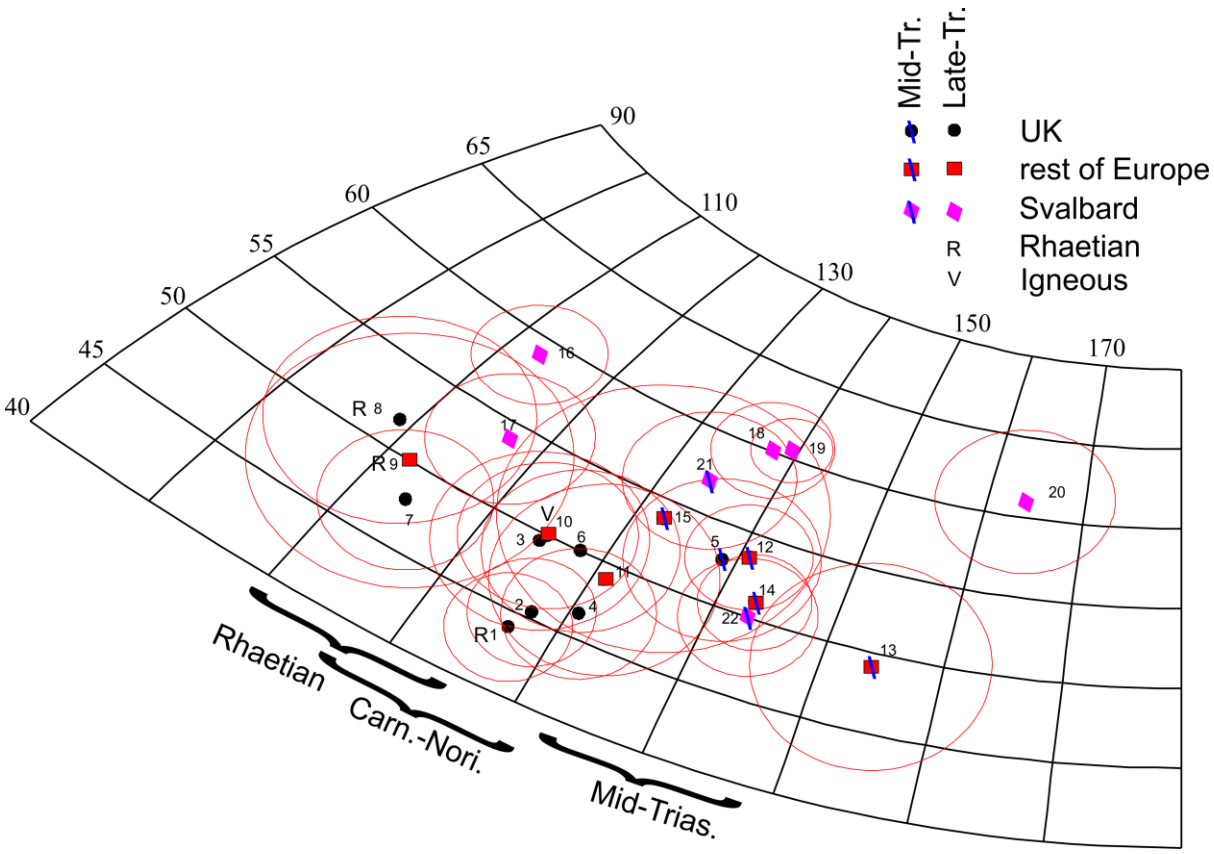

Fig. S4.1. VGP poles for stable Europe for the mid and late Triassic divided into source regions of the data and age intervals. The poles for the Devon coastal sections from this study are numbered 1 to 4, with 5 from Hounslow and McIntosh (2003). Apart from the poles from Svalbard these broadly indicate VGP latitude of ca. 50º, with the age intervals segmenting the data into larger (130-150º) and smaller VGP longitude. The poles are numbered according to Table S4.1.

Formation/Mb/Unit	α_{95}	Lat.	Long.	label	Pole ID
Haven Cliff section	3.4	44	126.6	L-MMG	1
Branscombe Mudstone Fm	3.4	45.4	127.5	L-MMG	2
Dunscombe Mudstone Fm	5.6	49.5	124.7	L-MMG	3
Sidmouth Mudstone Fm	4.1	46.5	130.7	L-MMG	4
Otter Sandstone Fm, Devon coast	5.1	52.8	138.8	M	5
Branscombe M. Fm, St Audrie' Bay	5.1	50	128	L-MMG	6
Branscombe M. Fm, St Audrie' Bay	4.4	47.9	114	L-MMG	7
Blue Anchor Fm, St Audrie' Bay	6.5	51.7	108.9	L-MMG	8
Rhaetian Sandstones	8	50	112	L	9
Sunhordland dykes (221± 5 Ma)	4.6	50	125	L	10
Gipskeuper red beds (Carnian)	6	49	131	L	11
Ladinian sediments, red dolomites	3.3	53.5	140.8	M	12
basal Anisian, Rot Fm	6.5	49.1	154.1	M	13
Polish Muscelkalk, Anisian	3	51	143	M	14
Edivetur Limestones, Anisian, Bulgaria	8.4	53.8	132.4	M	15
De Geerdalen Fm, Dalsnuten	3.1	59	113	S-L	16
Tschermakfjellet Fm, Dalsnuten	4.1	54	117	S-L	17
Nordstefjellet section, Hopen	3	60.1	137.6	S-L	18
Binnedalen section, Hopen	2	60.5	139.3	S-L	19
Tumlingodden, Wilhelmøya	4.5	61	163.8	S-L	20
Top Botneheia Fm, Milne_Edwardsfjellet	4.3	57	134	S-M	21
Botneheia Fm, Milne_Edwardsfjellet	3.7	50	143	S-M	22

Table 4.1. Triassic VGP poles for stable Europe. Label indicates category, M=mid Triassic, L=Late Triassic, S=from Svalbard, MMG=from Mercia Mudstone Group. Poles 1 to 4 from this work. 5=Hounslow and Mcintosh (2003). 6=Briden and Daniels (1999), 7-8=Hounslow et al. (2004).; 9,11=Edel and Duringer (1997); 10= Walderhaug et al. (1993); 12= Théveniaut _et al. (1992); 13=Szurlies (2007); 14= Nawrocki and Szulc (2000); 15= Muttoni et al. (2000). 16,17= Hounslow et al. (2007); 18-20= Hounslow et al (2022), 21-22=Hounslow et al. (2008).

Section S5: Reference magnetostratigraphic sections and the GPTS-B for the Norian and Rhaetian

The numbering of magnetochrons UT17 and UT18 (in main text Figs. 13, 15,16), has been changed from that given in Hounslow and Muttoni (2010), by upgrading the Newark magnetozone E12n (now UT17n) to a full magnetochron and down-grading the equivalent of E13r.1n (UT18r.1n) to a subchron. The marine composite for the Norian-Rhaetian boundary interval from Hounslow and Muttoni (2010) has been updated with new data (Fig. S5.1).

Magnetostratigraphic and U-Pb radiometric dating has given a clearer picture of the synchronicity between the eruption of the Central Atlantic Magmatic Province LIP, and events in the oceans near the Triassic-Jurassic boundary (Deenen et al. 2010, Whiteside et al. 2010; Olsen et al. 2011). Brief reverse polarity intervals are now seen to precede and follow the initial C^{13} isotopic excursion (Fig. S5.2), prior to the Triassic-Jurassic boundary (marked by *Psiloceras spaele* in the Hettangian GGSP at Kujoch; Schoene et al. 2011). Data from the Moenave Formation (Donohoo-Hurley et al. 2010) and Argana Basin (Deenen et al. 2010) was used to refine the magnetochrons UT25 to UT28 (Fig. S5.2) originally defined by Hounslow and Muttoni (2010). A Lower Jurassic, LJ chron numbering is

introduced (Fig. S5.2), with the placement of the magnetostratigraphy with respect to the Hettangian-Sinemurian boundary according to Ruhl et al. (2010). Kent et al. (2017) has proposed an alternative APTS for this interval based on the Newark-Hartford successions.

In addition, the Chinle Fm/Group in SW USA has a well-studied polarity dataset, with associated detrital zircon age dates which clearly dates it to the mid Norian. A composite magnetostratigraphy of the upper Chinle Fm is constructed and used in this work, and its source data and composite construction is outlined in the below section.

It has now been formally proposed that the GSSP for the Carnian-Norian boundary is placed in the Pizzo Mondello section at the first occurence of *Halobia austriaca,* which is within the lower part of magnetozone UT13n (PM5n at Pizzo Mondello), Hounslow et al. (2021).

S5.1 The Chinle Group/Fm magnetostratigraphy and U-Pb dates

Lithostratigraphic correlations between the various units of the upper Chinle Fm (some use this as a Group) in New Mexico, Arizona and Utah are problematic, and probably may not provide a particularly robust means of high-resolution correlation over large areas (Ramezani et al. 2011). This is fundamentally related to the complex fluvial system that the Chinle represents, and a number of unconformities which may sub-divide it (Heckert and Lucas 2002). Consequently, the magnetic polarity synthesis (SI Figs. S5.3, S5.4) has constructed magnetostratigraphy composites over smaller areas for comparison, based on; a) the Chama Basin (Zeigler and Geissman 2011) in northern New Mexico, b) San De Cristo Mts and Tucumcari Basin (Molina-Garza et al. 1996; Reeve and Helsley 1972; Zeigler and Geissman 2011) in eastern New Mexico, c) Petrified Forest National Park (PEFO) area in eastern Arizona (Steiner and Lucas 2000, Ziegler et al. 2017; Kent et al. 2019; Rasmussen et al. 2021). Sections S5.1.1 to S5.1.3 examine these regional records, and section S5.1.4 discusses their amalgamation in Fig. S5.4.

S5.1.1 Petrified Forest National Park (PEFO), Arizona

Biostratigraphy: The zone II/Zone III palynostratigraphic boundary (Litwin et al. 1991, refined by Baryani et al. 2018) in the PEFO is above the Rainbow Forest bed and within the Jim Camp Wash beds (Parker and Martz 2011; SI Fig S5.3) slightly below or at the level of the Adamanian - Revueltian vertebrate turnover (Baryani et al. 2018). This level has been correlated to the New Oxford-Lockatong – Lower Passaic Heidlersburg palynozone boundary in the Passaic Fm (Olsen et al. 2011; Lucas et al. 2012). A similar biostratigraphic correlation argument, but based on land vertebrate and conchostracan faunas has been proposed by Lucas et al. (2012) who correlate the bases of the Sonsela Member and the Passaic Formation, using specifically the miospore *Camerosporites veruccosus* which occurs in the Chinle Zone III assemblage from the PEFO (Parker and Martz 2011). This has a first occurrence (FO) in the base of the Passaic Fm (Warford- Graters members, in magnetozone E11; Lucas et al. 2012). In addition, the pollen *Perinopollenites elatoides* has been found in the Sonsela Sandstone in the base of zone III, which allows potential correlation of this interval to the mid Norian of the Germanic facies in Europe (Baryani et al. 2018). Contrastingly, Lucas et al. (2012) correlates the base of the Revueltian to the Warford Member of the Passaic Formation using vertebrate data (this is the mid part of magnetozone E11 in the Newark Supergroup).

Zircon U/Pb dates: An extensive and well documented re-evaluation of the lithostratigraphy of the Sonsela Member in the PEFO (Martz and Parker 2010; Parker and Martz 2011), has allowed a re-

evaluation of the magnetostratigraphic study of Steiner and Lucas (2000), along with more recent polarity data from outcrops (Ziegler et al. 2017) and the core through the PEFO succession (Kent et al. 2019). This allows the relationship between the magnetostratigraphy, the revised lithostratigraphy (Irmis et al. 2011; Parker and Martz 2011) and the zircon CA-ID TIMS U/Pb dates to be defined with greater confidence (Fig. S5.3). Based on the lithostratigraphy of Irmis et al. (2011) and the magnetostratigraphy of Zeigler and Geissman (2011), additional U-Pb dates from the Six Mile Canyon section and the Chama Basin can be related to the PEFO succession (Fig. S5.4). The detrital zircon age dates do represent substantial challenges in dating the age of deposition, since re-cycling of older zircons in the sand-prone units is probably an issue in the Sonsela Sandstone (Gehrels et al. 2020), which could have biased the zircon ages to older dates in the sandy units.

S5.1.2 Chama Basin, New Mexico

The main independent control on association between strata in the separate sub-basins of the Chinle Fm/Grp are the land vertebrate faunachrons (Lucas 2010), which broadly allow stratigraphic grouping of sections into the Adamanian, Revueltian and Apachean (left side of PEFO outcrop column in Fig. S5.4).

The Chama Basin composite (Fig S5.4) is based on the Coyote Amphitheatre section for the youngest units and the Abuiquiu Dam section for the Poleo Fm (Zeigler and Geissman 2011). The placement of the Hayden Quarry section radiometric date (i.e., 211.9 Ma) onto the Chama Basin magnetostratigraphy uses the lithostratigraphic correlation of Irmis et al. (2011). The roughly equal duration magnetozones in the Salitral Fm (Zeigler and Geissman 2011) is unlike the Norian, and in terms of relative magnetozone duration, is most similar to the polarity pattern in parts of the Carnian (see main text), so is not included in Fig. S5.4.

The reverse polarity dominated composite Chama Basin composite section through the Poleo Fm and Petrified Forest Mb is unlike the mixed polarity seen in the Revueltian LVF age strata from the PEFO, so may represent the reverse polarity intervals in the PEFO core PF4r and PF3r (Fig. S5.4). The uppermost normal polarity zone in the upper siltstone member (Chama Basin column) is likely related to that in the basal Redonda Mb, as proposed by Ziegler and Geissman (2011). The Hayden Quarry section U-Pb date (211.9 Myr) is correlated to near the base of the Petrified Forest Member in the Chama Basin (Irmis et al. 2011; Zeigler and Geissman 2011). The ~215 Ma date from Dickinson and Gehrels (2008) from the Poleo Fm suggests this interval is probably PF4r (Fig. S5.4). The correlation of the inferred ‘Rock Point’ unit in the Chama Basin to the Redonda Fm in eastern New Mexico follows Zeigler and Geissman (2011).

S5.1.3 Sangre de Cristo Mountains and Tucumcari Basins, New Mexico

Well constrained correlations between the Redonda Fm in the San De Cristo and Tucumcari basins are not possible. The upper part of the Redonda Fm (E. New Mexico column in Fig. S5.4) appears to be normal polarity dominated (Reeve and Helsley 1972; Molina-Garza et al. 1996), whereas the mid parts appear reverse to mixed polarity dominated (Fig. S5.4). There are differences between the magnetostratigraphy of the closby Mesa Redonda and Mesa Luciana sections near Tucumcari (Reeve and Helsley 1972; Ziegler and Geissman 2011), and the Redonda Mb composite reflects this uncertainty (due to differences in section thickness, and magnetic polarity in the lowermost and upper-most parts of the Redonda Fm in these sections). The Sebastian Canyon section of the Redonda Fm (Molina-Garza et al. 1996) is not shown due to its low-resolution sampling. The Revueltian and

Adamanian units in these basins are largely placed onto the composite chart (Fig. S5.4), using the land vertebrate faunachron data (Lucas 2010). Relying on the lithostratigraphic equivalence of the Trujillo and Poleo formations allows a tentative correlation of these sections.

S5.1.4. Construction of the upper Chinle Fm composite

The construction of the polarity composite is to a large extent guided by the many zircon U/Pb dates, along with the reference sections through the upper Chinle provided by the PEFO outcrops and core (Figs. S5.3, S5.4). The magnetostratigraphy in the Blue Mesa Mb seems well defined with three magnetic polarity studies in this interval (three PEFO colunns in Fig. S5.4). The Chinle composite CC1 to CC4 magnetozones are based on the PFNP-1A core (Fig. S5.4). From the PEFO, the Sonsela Sandstone is dominated by normal polarity, yet the apparent age equivalent units in the Chama Basin and Sangre de Cristo Mountains are reverse polarity dominated (except in the Tucamcari Basin (Garita Creek); Fig. S5.4). Substantial detrital U/Pb age differences of the Sonsela Sandstone are a feature of its regional occurrence (Marsh et al. 2019). The U/Pb dates in the PEFO both from outcrop and core, at face value, suggest a condensed (or hiatus) internal at around the position of the Rainbow/Jasper Forest bed (Fig. S5.3). A regional hiatus (TR4a or TR4b) in the lower or basal Sonsela Sandstone has also been widely inferred (Heckert and Lucas 2002; Tanner and Lucas 2006), and a change at around the Jasper Forest bed is coincident with a major climatic shift (Nordt et al. 2015), which may be the driver for any condensed interval or hiatus. We infer that further east in the New Mexico successions this hiatus is better expressed and has removed much of the lower part of the Sonsela Sandstone (i.e. better preserved in the PEFO), so that magnetozone CC5n is missing (e.g. in the Chama Basin), and the reverse polarity dominance as seen in E. New Mexico sections at this level largely represent PF4r and PF3r in the PEFO outcrops and core. Substantial differences in thickness of reverse and normal intervals in CC6 and CC7 also seem to be a feature of the Petrified Forest Mb and its equivalents which perhaps relate to the frequency of palaeosols in this member. The Redonda Mb is widely inferred to be largely Rhaetian in age, based on vertebrates and conchostracans (Lucas et al. 2012), and this is largely confirmed by inference based on magnetostratigraphy (Fig. S5.4 and main text).

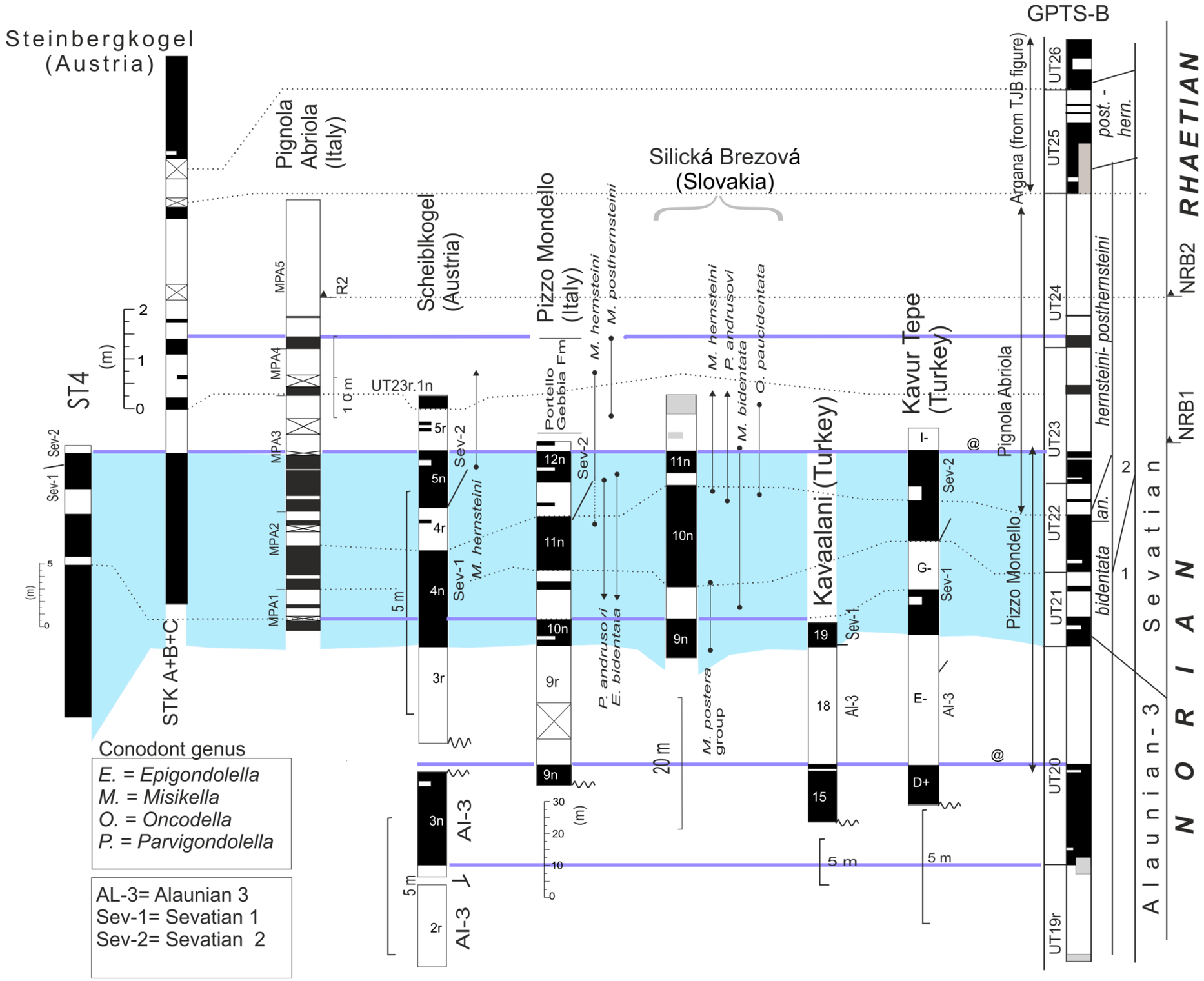

Fig. S5.1. The construction of the magnetostratigraphy around the Norian-Rhaetian boundary using marine sections with biostratigraphy. This is based on Fig. 10 in Hounslow and Muttoni (2010), but with the addition of new data from Steinbergkogel of Hüsing et al. (2011) and Pignola Abriola of Maron et al. (2015) and Bertinelli-et al. (2016). The two proposed options for the base of the Rhaetian are NRB1 and NRB2 (Bertinelli et al. 2016; Galbrun et al. 2020). The conodont zones are those of Rigo et al (2018), but with the contentious Rhaetian boundary interval shown as a conodont range. See Hounslow and Muttoni (2010) for source of other data in this figure. The Sevatian 1 and 2 interval uses the concepts used with the original magnetostratigraphic source data.

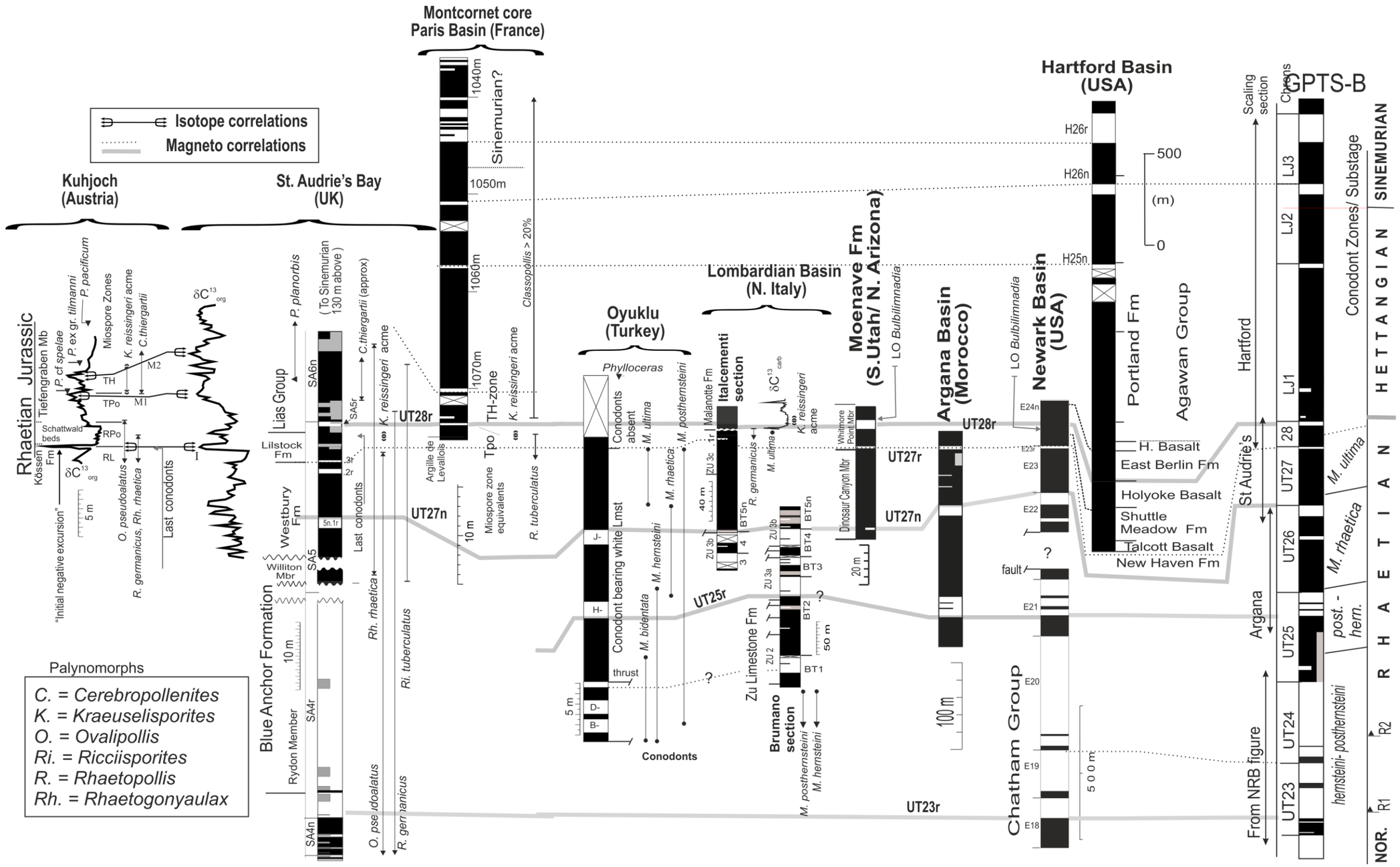

Fig. S5.2. Magnetostratigraphy of the Rhaetian-Hettangian transition modified from Hounslow and Muttoni (2010) by addition of data from the Moenave Fm (Donohoo-Hurley et al. 2010) and Argana Basin data (Deenan et al. 2010). Source details for other section data in Hounslow and Muttoni (2010). Main scaling anchors are UT23r, UT25r, UT27n, UT28r, LJ2n, LJ3r. Subsidiary scaling anchor UT27r. Based on the Italcementi and Brumano sections the interval UT25n- UT26r may be more complex (Maron et al. 2019, show very similar correlations) than is shown in the Newark Supergroup E21-E22, so an uncertain interval is inserted at the fault in the Newark core.

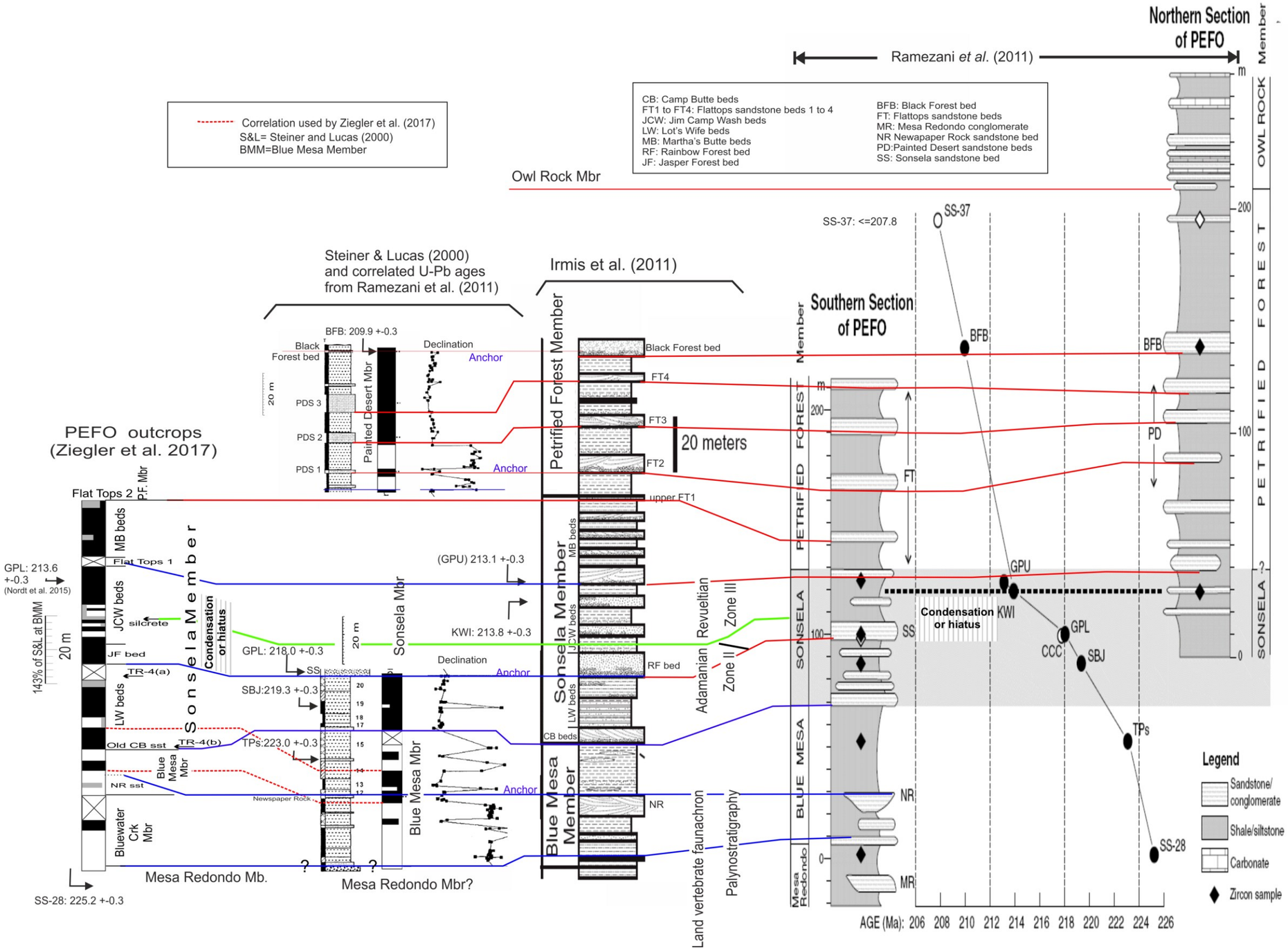

Fig. S5.3. Upper Chinle Formation lithostratigraphic columns used by the two main radiometric dating studies on outcrops in the Petrified Forest National Park (PEFO, Arizona), illustrating how the U-Pb dates (Irmis et al. 2011; Ramezani et al. 2011; Nordt et al. 2015) can be correlated to the PEFO outcrop magnetostratigraphy (Steiner and Lucas 2000; Ziegler et al. 2017), and biostratigraphy (Parker and Martz 2011; Baranyi et al. 2018) and hence their placement on Fig. S5.4. Member boundaries in blue. Sections from the CA-IDTIMS U/Pb dating studies have been scaled using the top of the Newspaper Rock Sandstone and the base of the Black Forest bed. Green correlation line is the Adamanian-Revueltian boundary.

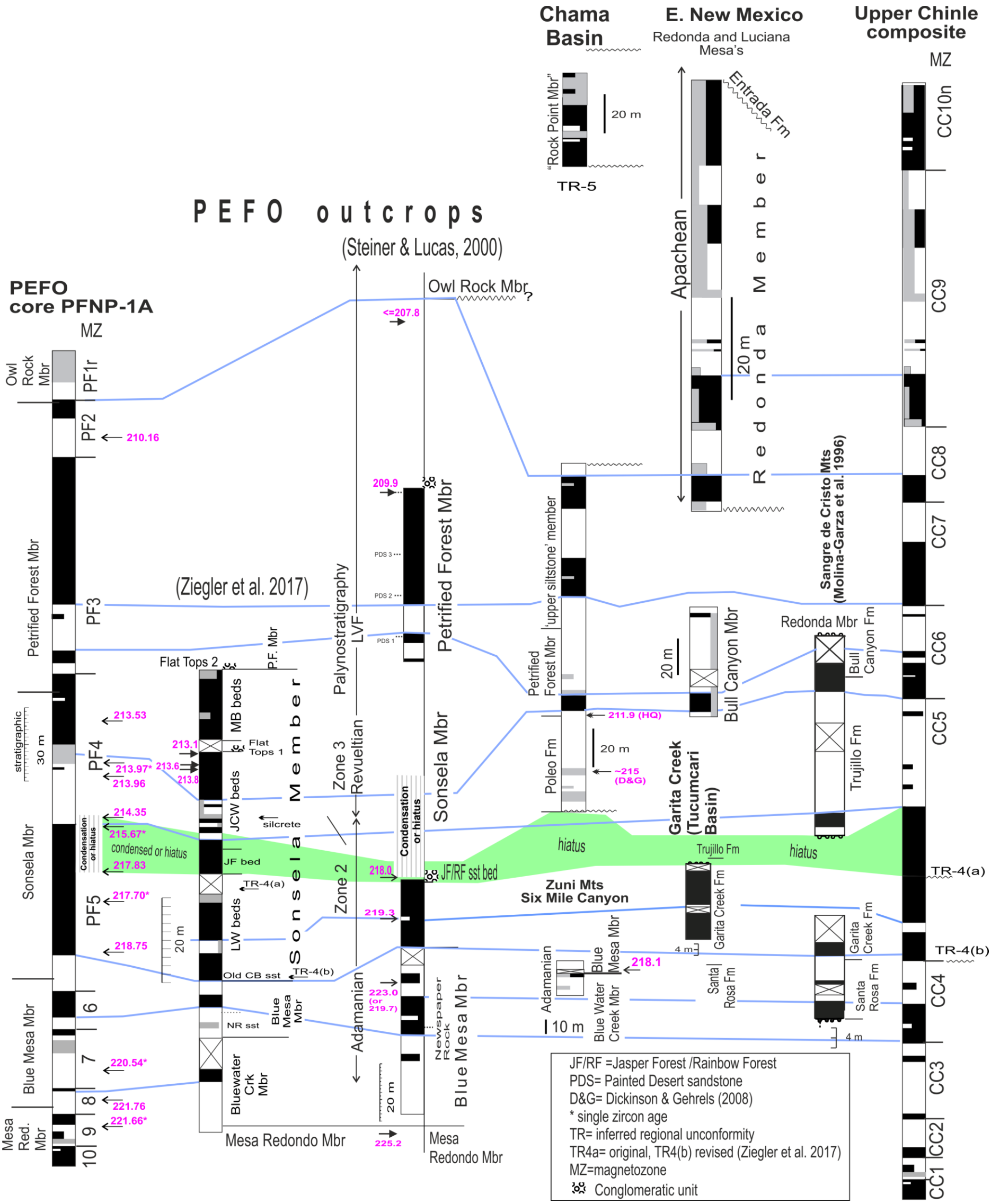

Fig. S5.4. Correlations between the various sections with magnetostratigraphy from the Chinle Fm/Group. The data from the Petrified Forest National Park (PEFO) is related to the reference section in the PEFO core 1a, and its associated detrital zircon dates (Kent et al. 2019; Rasmussen et al. 2021). The magnetic polarity stratigraphy from the outcrops in the PEFO (Steiner and Lucas 2000) indicates a close similarity the Blue Mesa, Sonsela and Petrified Forest members in the cores. Sources of other data for the Chinle Group are Reeve and Helsley (1972), Molina-Garza et al. (1996 2003), Zeigler and Geissman (2010). These sources have all been re-drawn with the same style for uncertain intervals and sampling gaps. See the text for discussion of these relationships.

Supplementary References

Baranyi, V., Reichgelt, T., Olsen, P.E., Parker, W.G. and Kürschner, W.M. 2018. Norian vegetation history and related environmental changes: New data from the Chinle Formation, Petrified Forest National Park (Arizona, SW USA). *GSA Bulletin*, 130, 775-795.

Baranyi, V., Miller, C.S., Ruffell, A., Hounslow, M.W. and Kürschner, W.M. 2019. A continental record of the Carnian Pluvial Episode (CPE) from the Mercia Mudstone Group (UK): palynology and climatic implications. *Journal of the Geological Society*, 176, 149-166.

Bertinelli, A., Casacci, M., Concheri, G., Gattolin, G., Godfrey, L., Katz, M.E., Maron, M., Mazza, M., Mietto, P., Muttoni, G. and Rigo, M. 2016. The Norian/Rhaetian boundary interval at Pignola-Abriola section (Southern Apennines, Italy) as a GSSP candidate for the Rhaetian Stage: an update. *Albertiana*, 43, 5-18.

Briden, J.C. and Arthur, G.R., 1981. Precision of measurement of remanent magnetization. *Canadian Journal of Earth Sciences*, 18, 527-538.

Briden, J.C. and Daniels, B.A. 1999. Palaeomagnetic correlation of the Upper Triassic of Somerset, England, with continental Europe and eastern North America. *Journal of the Geological Society*, 156, 317-326.

Creer K.M. 1955. *A preliminary survey of certain rocks in England and Wales*. PhD. Thesis Cambridge, 203pp.

Creer, K.M. 1957. V. The remanent magnetization of unstable Keuper Marls. Philosophical *Transactions of the Royal Society of London. Series A, Mathematical and Physical Sciences*, 250, 130-143.

Creer, K.M. 1959. AC demagnetization of unstable Triassic Keuper Marls from SW England. *Geophysical Journal of the Royal Astronomical Society*, 2, 261-275.

Creer, K.M. 1961. Superparamagnetism in red sandstones. *Geophysical Journal of the Royal Astronomical Society,* **5**, 16-28.

Creer, K.M. 1962. On the origin of the magnetization of red beds. *Journal of geomagnetism and geoelectricity*, **13**, 86-100.

Cromwell, G., Johnson, C.L., Tauxe, L., Constable, C.G. and Jarboe, N.A. 2018. PSV10: A global data set for 0–10 Ma time-averaged field and paleosecular variation studies. *Geochemistry, Geophysics, Geosystems*, 19, 1533-1558.

Deenen, M.H.L., Ruhl, M., Bonis, N.R. Krijgsman, W., Kuerschner W.M. Reitsma M. and van Bergen M.J. 2010. A new chronology for the end-Triassic mass extinction. *Earth and Planetary Science Letters* 291**,** 113–125.

Deenen, M.H., Langereis, C.G., van Hinsbergen, D.J. and Biggin, A.J. 2011. Geomagnetic secular variation and the statistics of palaeomagnetic directions. *Geophysical Journal International*, 186, 509-520.

Dickinson, W.R. and Gehrels, G.E. 2008. U-Pb ages of detrital zircons in relation to paleogeography: Triassic paleodrainage networks and sediment dispersal across southwest Laurentia. *Journal of Sedimentary Research*, 78, 745-764.

Donohoo-Hurley, L.L., Geissman, J.W. and Lucas, S.G. 2010. Magnetostratigraphy of the uppermost Triassic and lowermost Jurassic Moenave Formation, western United States: Correlation with strata in the United Kingdom, Morocco, Turkey, Italy, and eastern United States. *GSA Bulletin, 122*, 2005-2019.

Duff, B.A. 1979. Peaked thermomagnetic curves for hematite-bearing rocks and concentrates. *Physics of the Earth and Planetary Interiors*, 19, 1-4.

Edel, J.B. and Duringer, P.H. 1997. The apparent polar wander path of the European plate in Upper Triassic-Lower Jurassic times and the Liassic intraplate fracturing of Pangaea: new palaeomagnetic constraints from NW France and SW Germany. *Geophysical Journal International*, 128, 331-344.

Edwards, R.A. and Gallois, R.W., 2004. *Geology of the Sidmouth district: a brief explanation of the geological map sheets 326 and 340 Sidmouth*. British Geological Survey, HMSO.

Fisher, N.I., Lewis, T. and Embleton, B.J., 1993. *Statistical analysis of spherical data*. Cambridge University Press, Cambridge.

France, D.E. and Oldfield, F. 2000. Identifying goethite and hematite from rock magnetic measurements of soils and sediments. *Journal of Geophysical Research: Solid Earth,* 105, 2781-2795.

Galbrun, B., Boulila, S., Krystyn, L., Richoz, S., Gardin, S., Bartolini, A. and Maslo, M. 2020. " Short" or" long" Rhaetian? Astronomical calibration of Austrian key sections. *Global and Planetary Change*, 192, doi.org/10.1016/j.gloplacha.2020.103253.

Gallois, R.W. 2003. The distribution of halite (rock-salt) in the Mercia Mudstone Group (mid to late Triassic) in south-west England. *Geoscience in south-west England,* 10, 383-389.

Gallois, R.W. and Porter, R.J. 2006. The stratigraphy and sedimentology of the Dunscombe Mudstone Formation (late Triassic) of south-west England. *Geoscience in south-west England,* 11, 174-182.

Gehrels, G., Giesler, D., Olsen, P., Kent, D., Marsh, A., Parker, W., Rasmussen, C., Mundil, R., Irmis, R., Geissman, J. and Lepre, C. 2020. LA-ICPMS U–Pb geochronology of detrital zircon grains from the Coconino, Moenkopi, and Chinle formations in the Petrified Forest National Park (Arizona). *Geochronology*, 2, 257-282.

Heckert, A.B. and Lucas, S.G. 2002. Revised Upper Triassic stratigraphy of the Petrified Forest National Park, Arizona, USA. *In:* Heckert, A.B., and Lucas, S.G., eds., *Upper Triassic Stratigraphy and Paleontology*, *New Mexico Museum of Natural History and Science Bulletin*, 21, 1-36.

Hounslow, M.W. and McIntosh, G. 2003. Magnetostratigraphy of the Sherwood Sandstone Group (Lower and Middle Triassic), south Devon, UK: detailed correlation of the marine and non-marine Anisian. *Palaeogeography, Palaeoclimatology, Palaeoecology*, 193, 325-348.

Hounslow, M.W., Posen, P.E. and Warrington, G. 2004. Magnetostratigraphy and biostratigraphy of the Upper Triassic and lowermost Jurassic succession, St. Audrie's Bay, UK. *Palaeogeography, Palaeoclimatology, Palaeoecology*, 213, 331-358.

Hounslow, M.W., Hu, M., Mørk, A., Vigran, J.O., Weitschat, W. and Orchard, M.J. 2007. Magneto-biostratigraphy of the Middle to Upper Triassic transition, central Spitsbergen, arctic Norway. *Journal of the Geological Society*, 164, 581-597.

Hounslow, M.W., Hu, M., Mørk, A., Weitschat, W., Vigran, J.O., Karloukovski, V. and Orchard, M.J. 2008. Intercalibration of Boreal and Tethyan time scales: the magnetobiostratigraphy of the Middle Triassic and the latest Early Triassic from Spitsbergen, Arctic Norway. *Polar Research,* 27, 469-490.

Hounslow, M.W. and Muttoni, G. 2010. The geomagnetic polarity timescale for the Triassic: linkage to stage boundary definitions. *In:* Lucas, S.G. (ed) *The Triassic timescale*, *Geological Society, London, Special Publications*, 334, 61-102.

Hounslow, M.W. McKie, T. and Ruffell, A,H. 2012. Permian and Late Triassic post-orogenic collapse and rifting, arid deserts, evaporating seas and mass extinctions. *In:* Woodcock, N. and Strachan, R.(eds). *Geological history of Britain and Ireland.* Wiley-Blackwell, 2nd edn. 299-321.

Hounslow, M.W., Bachmann, G.H., Balini, M., Benton, M.J. Carter, E.S., Konstantinov, A.G., Golding, M.L., Krystyn, L., Kürschner, W., Lucas, S.G., McRoberts, C.A., Muttoni, G., Nicora, A., Onoue, T., Orchard, M.J., Ozsvárt, P., Paterson, N.W., Richoz, S., Manuel Rigo, M., Sun, Y., Tackett, L.S., Kağan Tekin, U., Wang, Y., Zhang, Y., and Zonneveld. J.-P. 2021. The case for the Global Stratotype Section and Point (GSSP) for the base of the Norian Stage. *Albertiana*, 46, 25–57 https://albertiana-sts.org/wp-content/uploads/2021/12/46-4_Hounslow_etal_2021.pdf

Hounslow, M.W., Harris, S., Karloukovski, V. and Mørk, A. 2022. Geomagnetic polarity and carbon isotopic stratigraphic assessment of the late Carnian-earliest Norian in Svalbard: evidence for a major hiatus and improved Boreal to Tethyan correlation. *Norwegian Journal of Geology*, 102. https://njg.geologi.no/images/NJG_articles/220409_Hounslow.pdf.

Hüsing, S.J. Deenen, M.H.L., Koopmans, J.G. and Krijgsman, W. 2011. Magnetostratigraphic dating of the proposed Rhaetian GSSP at Steinbergkogel (Upper Triassic Austria): Implications for the Late Triassic time scale. *Earth and Planetary Science Letters* 302**,** 203-216.

Irmis, R.B, Mundil, R., Martz, J.W. and Parker, W.G. 2011. High resolution U-Pb ages from the Upper Triassic Chinle Fm (New Mexico, USA) support a diachronous rise of dinosaurs. *Earth and Planetary Science Letters,* 309, 258-267.

Kent, D.V., Olsen, P.E. and Muttoni, G. 2017. Astrochronostratigraphic polarity time scale (APTS) for the Late Triassic and Early Jurassic from continental sediments and correlation with standard marine stages. *Earth-Science Reviews,* 166, 153-180.

Kent, D.V., Olsen, P.E., Lepre, C., Rasmussen, C., Mundil, R., Gehrels, G.E., Giesler, D., Irmis, R.B., Geissman, J.W. and Parker, W.G. 2019. Magnetochronology of the entire Chinle Formation (Norian age) in a scientific drill core from Petrified Forest National Park (Arizona, USA) and implications for regional and global correlations in the Late Triassic. *Geochemistry, Geophysics, Geosystems*, 20, 4654-4664.

Litwin, R. J, Traverse, A. and Ash, S. R. 1991. Preliminary palynological zonation of the Chinle Formation, southwestern U.S.A., and its correlation to the Newark Supergroup (eastern USA). *Review of Palaeobotany and Palynology,* 68, 269–87.

Lucas, S.G. 2010.The Triassic timescale based on non marine tetrapod biostratigraphy and biochronology *In:* Lucas, S.G. (ed). *The Triassic timescale*, *Special Publication of the Geological Society*, 334, 447-500.

Lucas, S.G. Tanner, L.H. Kozur, H.W., Weems, R.E. and Heckert, A.B. 2012. The late Triassic timescale: Age and correlation of the Carnian-Norian boundary. *Earth- Science Reviews*, 114, 1–18.

Maher, B.A., Karloukovski, V.V. and Mutch, T.J. 2004. High-field remanence properties of synthetic and natural submicrometre haematites and goethites: significance for environmental contexts. *Earth and Planetary Science Letters*, 226, 491-505.

Maron, M., Muttoni, G., Rigo, M., Gianolla, P. and Kent, D.V. 2019. New magnetobiostratigraphic results from the Ladinian of the Dolomites and implications for the Triassic geomagnetic polarity timescale. *Palaeogeography, Palaeoclimatology, Palaeoecology*, 517, 52-73.

Maron, M., Rigo, M., Bertinelli, A., Katz, M.E., Godfrey, L., Zaffani, M. and Muttoni, G. 2015. Magnetostratigraphy, biostratigraphy, and chemostratigraphy of the Pignola-Abriola section: New constraints for the Norian-Rhaetian boundary. *GSA Bulletin*, 127, 962-974.

Marsh, A.D., Parker, W.G., Stockli, D.F. and Martz, J.W. 2019. Regional correlation of the Sonsela Member (Upper Triassic Chinle Formation) and detrital U-Pb zircon data from the Sonsela Sandstone bed near the Sonsela Buttes, northeastern Arizona, USA, support the presence of a distributive fluvial system. *Geosphere*, 15, 1128-1139.

Martz, J.W. and Parker, W.G. 2010. Revised lithostratigraphy of the Sonsela Member (Chinle Formation, Upper Triassic) in the southern part of Petrified Forest National Park, Arizona. *PLoS One,* 5 (e9329), 1–26.

McFadden, P.L. and McElhinny, M.W. 1988. The combined analysis of remagnetization circles and direct observations in palaeomagnetism. *Earth and Planetary Science Letters*, 87, 161-172.

McFadden, P.L. and McElhinny, M.W. 1990. Classification of the reversal test in palaeomagnetism. *Geophysical Journal International*, 103, 725-729.

Molina-Garza, R.S., Geissman, J.W. and Lucas, S.G. 2003. Paleomagnetism and magnetostratigraphy of the lower Glen Canyon and upper Chinle Groups, Jurassic- Triassic of northern Arizona and northeast Utah. *Journal of Geophysical Research* 108, doi: 10.1029/2002JB001909.

Molina-Garza, R.S., Geissman, J.W., Lucas, S.G. and Van der Voo, R. 1996. Palaeomagnetism and magnetostratigraphy of Triassic strata in the Sangre de Cristo Mountains and Tucumcari Basin, New Mexico, U.S.A. *Geophysical Journal International* 124, 935-953.

Muttoni, G., Gaetani, M., Budurov, K., Zagorchev, I., Trifonova, E., Ivanova, D., Petrounova, L. and Lowrie, W. 2000. Middle Triassic paleomagnetic data from northern Bulgaria: constraints on Tethyan magnetostratigraphy and paleogeography. *Palaeogeography, Palaeoclimatology, Palaeoecology*, 160, 223-237.

Nawrocki, J. and Szulc, J. 2000. The Middle Triassic magnetostratigraphy from the Peri-Tethys basin in Poland. *Earth and Planetary Science Letters*, 182, 77-92.

Nordt, L., Atchley, S. and Dworkin, S. 2015. Collapse of the Late Triassic megamonsoon in western equatorial Pangea, present-day American Southwest. *GSA Bulletin*, 127, 1798-1815.

Newell, A.J. 2018a. Evolving stratigraphy of a Middle Triassic fluvial-dominated sheet sandstone: The Otter Sandstone Formation of the Wessex Basin (UK). *Geological Journal*, 53, 1954-1972.

Newell, A.J. 2018b. Rifts, rivers and climate recovery: A new model for the Triassic of England. *Proceedings of the Geologists' Association*, 129, 352-371.

Olsen, P.E., Kent, D.V. and Whiteside, J.H. 2011. Implications of the Newark Supergroup-based astrochronology and geomagnetic polarity time scale (Newark-APTS) for the tempo and mode of the early diversification of the Dinosauria. *Earth and Environmental Science Transactions of the Royal Society of Edinburgh,* 101, 1–33.

Parker W.G and Martz, J.W. 2011. The Late Triassic (Norian) Adamanian– Revueltian tetrapod faunal transition in the Chinle Formation of Petrified Forest National Park, Arizona. *Earth and Environmental Science Transactions of the Royal Society of Edinburgh*, 101, 231–260.

Ramezani, J., Bowring, S.A., Martin,Ramezani, J., Hoke, G.D., Fastovsky, D.E. Bowring, S.A., Therrien, F., Dworkin, S.I., Atchley, S.C. and Nordt, L.C. 2011. High-precision U-Pb zircon geochronology of the Late Triassic Chinle Fm, Petrified Forest National Park (Arizona, USA): Temporal constraints on the early evolution of dinosaurs. *Geol. Soc. America Bulletin,* 123, 2142-2159.

Rasmussen, C., Mundil, R., Irmis, R.B., Geisler, D., Gehrels, G.E., Olsen, P.E., Kent, D.V., Lepre, C., Kinney, S.T., Geissman, J.W. and Parker, W.G. 2021. U-Pb zircon geochronology and depositional age models for the Upper Triassic Chinle Formation (Petrified Forest National Park, Arizona, USA): Implications for Late Triassic paleoecological and paleoenvironmental change. *Geol. Soc. America Bulletin*, 133, 539-558.

Reeve, S.C. and Helsley, C.E. 1972. Magnetic reversal sequence in the upper part of the Chinle Formation, Montoya, New Mexico. *Geological Society of America Bulletin,* 83, 3795-3812.

Rigo, M., Mazza, M., Karádi, V. and Nicora, A. (2018). New Upper Triassic Conodont Biozonation of the Tethyan Realm. *In:* Tanner, L. (eds) *The Late Triassic World. Topics in Geobiology*, 46. 189-235, Springer, Cham. https://doi.org/10.1007/978-3-319-68009-5_6.

Ruhl, M., Deenen, M.H.L., Abel, H.A., Bonis, N.R., Krijgsman, W. and Kürschner, W.M. 2010. Astronomical constraints on the duration of the early Jurassic Hettangian stage and recovery rates following the end-Triassic mass extinction (St Audrie's Bay/East Quantoxhead, UK). *Earth and Planetary Science Letters* 295, 262–276.

Schoene, B., Guex, J., Bartolini, A., Schaltegger, U. and Blackburn, T.J. 2011. Correlating the end-Triassic mass extinction and flood basalt volcanism at the 100ka level. *Geology* 38, 387-390.

Schwarz, E.J. 1968. Thermomagnetic analysis of some red beds. *Earth and Planetary Science Letters*, 5, 333-338.

Shive, P.N. and Diehl, J.F. 1977. Thermomagnetic analysis of natural and synthetic hematite. *Geophysical Research Letters*, 4, 159-162.

Steiner, M.B. and Lucas, S.G. 2000. Palaeomagnetism of the late Triassic Petrified Forest Fm, Chinle Group, western United States: Further evidence of 'large' rotation of the Colorado Plateau. *Journal of Geophys. Res*., 105, 25791-25808.

Szurlies, M. 2007. Latest Permian to Middle Triassic cyclo-magnetostratigraphy from the Central European Basin, Germany: Implications for the geomagnetic polarity timescale. *Earth and Planetary Science Letters,* 261, 602-619.

Talbot, M., Holm, K. and Williams, M. 1994. Sedimentation in low-gradient desert margin systems: A comparison of the Late Triassic of northwest Somerset (England) and the late Quaternary of east central Australia. *In:* Rosen, M.R. (ed). *Paleoclimate and basin evolution of playa systems*, *Geol. Soc of America special paper,* 289, 97-118,

Tanner, L.H. and Lucas, S.G. 2006, Calcareous paleosols of the Upper Triassic Chinle Group, Four Corners region, southwestern United States: Climatic implications. *In:* Alonso-Zarza, A.M. and Tanner, L.H., (eds), *Paleoenvironmental record and applications of calcretes and palustrine carbonates. Geological Society of America Special Paper*, 416, 53–74.

Théveniaut, H., Besse, J., Edel, J.B., Westphal, M. and Duringer, P. 1992. A Middle-Triassic paleomagnetic pole for the Eurasian plate from Heming (France). *Geophysical Research Letters*, **19**, 777-780.

Vollmer, F.W. 1995. C program for automatic contouring of spherical orientation data using a modified Kamb method. *Computers and Geosciences*, 21, 31-49.

Vollmer, T., Werner, R., Weber, M., Tougiannidis, N., Röhling, H.G. and Hambach, U. 2008. Orbital control on Upper Triassic Playa cycles of the Steinmergel-Keuper (Norian): A new concept for ancient playa cycles. *Palaeogeography, Palaeoclimatology, Palaeoecology*, 267, 1-16.

Walderhaug, H. 1993. Rock magnetic and magnetic fabric variations across three thin alkaline dykes from Sunnhordland, western Norway; influence of initial mineralogy and secondary chemical alterations. *Geophysical Journal International*, 115, 97-108.

Whiteside, J.H., Olsen P.E., Eglinton, T., Brookfield M.E. and Sambrotto R.N. 2010. Compound-specific carbon isotopes from Earth's largest flood basalt eruptions directly linked to the end-Triassic mass extinction. *Proc. Nation. Acad. Sci*., 107**,** 6721–6725.

Zeigler, K.E., Parker, W.G. and Martz, J.W. 2017. The lower Chinle Formation (Late Triassic) at Petrified Forest National Park, southwestern USA: A case study in magnetostratigraphic correlations. *In:* Ziegler, K.E and Parker, W.G. (eds). *Terrestrial depositional systems*, 237-277, Elsevier. doi.org/10.1016/B978-0-12-803243-5.00006-6

Ziegler, K.E. and Geissman, J.W. 2011. Magnetostratigraphy of the Upper Triassic Chinle Group of New Mexico: Implications for regional and global correlations among Upper Triassic sequences. *Geosphere,* 7, 802-829.